THERMO-MECHANICAL BEHAVIOR DURING STEEL CONTINUOUS CASTING IN FUNNEL MOLDS

BY

LANCE C. HIBBELER

THESIS

Submitted in partial fulfillment of the requirements
for the degree Master of Science in Mechanical Engineering
in the Graduate College of the
University of Illinois at Urbana-Champaign, 2009

Urbana, Illinois

Adviser:

Professor Brian G. Thomas

ABSTRACT

Computational models have been developed to investigate the thermal and mechanical behavior of the solidifying steel shell in continuous casting funnel molds, with the goal of understanding the effect of funnel shape on the solidifying steel shell. The numerical models have been calibrated with plant measurements from the Corus Direct Sheet Plant in IJmuiden, The Netherlands, and are used to recommend funnel designs and narrow-face taper practices. The steady-state temperature distribution in the mold is calculated in three-dimensions, and then used to calibrate and validate a simpler one-dimensional model of mold heat transfer. The results are applied to explain the effect of mold wear on the measured mold temperatures and heat fluxes. Investigation of the mechanical behavior of the solidifying shell has identified the geometry of the funnel has little influence on the thermal behavior of the solidifying shell, but induces a bending effect in the shell that is absent in conventional parallel-face molds. This bending effect is shown to increase the likelihood of crack formation in the "inside curve" region of the funnel, due to increased tensile stress on the solidification front. This mechanical effect can be mitigated by using a shallow and wide funnel with no inner flat region. Naturally, this finding needs to be balanced with the original purpose of the funnel, to allow room for the submerged entry nozzle, and with other crack mechanisms in order to find the optimal funnel-shape design.

ACKNOWLEDGEMENTS

This work would not have been possible without the support of several people. I would like to thank my adviser, Brian G. Thomas, for his enthusiastic support and technical expertise provided during this project. Several previous students of Professor Thomas have paved the way for this work, including Dr. Seid Koric, Dr. Chunsheng Li, and Dr. Hong Zhu. I gratefully acknowledge the financial support of the member companies of the Continuous Casting Consortium at The University of Illinois, which at the time of this writing includes ABB, Arcelor-Mittal, Baosteel, Corus, Delavan/Goodrich, LWB Refractories, Nucor, Nippon Steel, Postech, Steel Dynamics, and ANSYS-Fluent. Computational resources were provided by the National Center for Supercomputing Applications (NCSA) at the University of Illinois. My colleagues at Corus IJmuiden were instrumental in this work by initially posing the question to be answered and providing plant measurements, and include Begoña Santillana, Gert Abbel, Arie Hamoen, Arnoud Kamperman, Jean Campaniello, and Frank Grimberg.

I would like to thank some of the other graduate students in the Continuous Casting Consortium and the Department of Mechanical Science and Engineering for their camaraderie and many shared meals during my tenure at the University of Illinois, including Rajneesh Chaudhary, Kevin Cukierski, Mark Hernquist, Hemanth Jasti, Rui Liu, Dr. Russell McDonald, Joe Miksan, Michael Okelman, Bryan Petrus, Matt Rowan, Varun Singh, Aravind Sundararajan, Kun Xu, and Xiaoxu Zhou. Finally, I would like to thank my family for their support of my endeavors in higher education.

TABLE OF CONTENTS

LIST OF FIGURES

LIST OF TABLES

PRINCIPAL NOMENCLATURE

Symbols used in this work include both upper- and lower-case Roman and Greek letters. Subscripts and superscripts include letters, Arabic numerals, and typographical glyphs. Scalars are represented by italicized symbols, a. Thermodynamic variables such as enthalpy are discussed in terms of "total" quantities with capital letters H, and in terms of "specific" quantities (*i.e.*, per unit mass) with small letters h. Two- and three-dimensional vectors are represented by boldface, italicized, lower-case Roman letters, $\boldsymbol{a}$, and n-dimensional vectors such as those used in numerical models are symbols within braces (curly brackets) $\{a\}$. Second-order tensors are represented with boldface, italicized, upper-case Roman letters and lower-case Greek letters, $\boldsymbol{A}$ and $\boldsymbol{\alpha}$. Fourth-order tensors are represented with boldface upper-case Roman letters, $\mathbf{A}$. Matrices, including the matrix representation of the components of tensors, are symbols within brackets (square brackets), $[A]$. Unless specifically mentioned otherwise, the meter-kilogram-second-ºC unit system is adopted in this work.

Symbol	Description
a_1, a_2	Parameters in thermal conductivity model
$\boldsymbol{b}_i$	Bézier curve control points, $i = 1, 2, 3, 4$
$\boldsymbol{b}_c$	Bézier curve vector
$\boldsymbol{C}$	Right Cauchy-Green strain tensor (second-order)
C	Carbon composition
c_i	Constants used various models, $i = 1, 2, 3, 4, \ldots$
c	Funnel crown
c_B	Funnel crown at mold bottom / mold exit
c_T	Funnel crown at mold top
c_p	Constant-pressure specific heat capacity
$\boldsymbol{D}$	Rate-of-deformation tensor (second-order)
E	Elastic (Young's) modulus
$\boldsymbol{F}$	Deformation gradient tensor (second-order)
f_i	Mass fraction of phase i
g	Acceleration due to gravity

g_i	Volume fraction of phase i
H_i h_i	Total, specific enthalpy of phase i
H_f	Enthalpy of formation (latent heat of fusion)
$\boldsymbol{I}$, $\mathbf{I}$	Second- and fourth-order identity tensors
$\boldsymbol{K}$	Thermal conductivity tensor (second-order)
K	Bulk modulus
k_i	Thermal conductivity of phase i
ℓ_f	Funnel length
ℓ_m	Mold length
$\boldsymbol{n}$	Outward-pointing surface normal vector
Q	Activation energy
$\boldsymbol{q}$	Heat flux vector
$\boldsymbol{R}$	Rotation tensor (second order)
r_h	Horizontal plane funnel radius
r_v	Vertical plane funnel radius
s	Mold surface position
T	Temperature
T_0	Initial temperature
T_{liq}	Liquidus temperature
T_{ref}	Reference temperature
T_{sol}	Solidus temperature
$\boldsymbol{t}$	Surface traction vector
t	Time
t_0	Reference time
t_d	Dwell time of shell in mold
t_s	Slab/strand half-thickness
$\boldsymbol{U}$	Right stretch tensor (second-order)
$\boldsymbol{u}$	Displacement vector
$\boldsymbol{V}$	Left stretch tensor (second-order)
V	Volume
V_C	Casting speed
V_f	Funnel volume

w_i	Inner funnel half-width
w_m	Middle funnel half-width
w_o	Outer funnel half-width
w_s	Slab/strand half-width
x , y , z	Spatial coordinates
z_t	Location of upper tangent point
α_E	Coefficient of thermal expansion
α_T	Thermal diffusivity
β	Bézier curve parameter
Δ_y , Δ_z	Distance between tangent points on linear funnel
δ	Shell thickness
δ_{NF}	Narrow face taper as a raw length
$\boldsymbol{\varepsilon}$, ε_{ij}	Linearized total strain tensor, component ij (second-order)
$\boldsymbol{\varepsilon}^{el}$, ε_{ij}^{el}	Elastic strain tensor, component ij (second-order)
$\boldsymbol{\varepsilon}^{ie}$, ε_{ij}^{ie}	Inelastic strain tensor, component ij (second-order)
$\boldsymbol{\varepsilon}^{th}$, ε_{ij}^{th}	Thermal strain tensor, component ij (second-order)
$\bar{\varepsilon}^{ie}$	Equivalent inelastic strain
$\dot{\bar{\varepsilon}}^{ie}$	Equivalent inelastic strain rate
ϕ	Bézier curve parameter
η	Bézier curve parameter
μ	Lamé's second elastic constant (shear modulus)
ν	Poisson's ratio
ρ	Mass density
$\boldsymbol{\sigma}$, σ_{ij}	Cauchy stress tensor, component ij (second-order)
$\boldsymbol{\sigma}'$	Deviatoric Cauchy stress tensor (second-order)
$\bar{\sigma}$	Equivalent stress
σ_Y	Yield stress
ψ	Intermediate function used in Bézier curve funnel

Various mathematical operators are used in this work. Standard conventions are adopted, and are summarized here. The operators that are defined for second-order tensors have direct analogues for higher-order tensors and use the same symbols. All coordinate systems considered in this work are orthonormal, and specifically rectangular/Cartesian, so there is no need to track the covariance and contravariance of the gradient operator. Matrix operators use the same symbols as the tensor operators for the analogous operations (inverse, transpose, determinant).

Operator	**Meaning**
$\dot{a}$, $\dot{\boldsymbol{a}}$, $\dot{\boldsymbol{A}}$	First time derivative of variable
$\ddot{a}$, $\ddot{\boldsymbol{a}}$, $\ddot{\boldsymbol{A}}$	Second time derivative of variable
∇a, $\nabla \boldsymbol{a}$	Gradient of scalar field a or vector field $\boldsymbol{a}$
$\nabla \cdot \boldsymbol{a}$, $\nabla \cdot \boldsymbol{A}$	Divergence of vector field $\boldsymbol{a}$ or tensor field $\boldsymbol{A}$
$\nabla \times \boldsymbol{a}$, $\boldsymbol{a} \times \nabla$	Curl, conjugate curl of vector field $\boldsymbol{a}$
$\boldsymbol{a} \cdot \boldsymbol{b}$	Inner (dot, scalar) product of vectors $\boldsymbol{a}$ and $\boldsymbol{b}$
$\boldsymbol{a} \times \boldsymbol{b}$	Cross product of vectors $\boldsymbol{a}$ and $\boldsymbol{b}$
$\boldsymbol{A} \cdot \boldsymbol{a}$, $\boldsymbol{A} \cdot \boldsymbol{B}$	Tensor $\boldsymbol{A}$ operating from the left on vector $\boldsymbol{a}$ or tensor $\boldsymbol{B}$
$\boldsymbol{a} \cdot \boldsymbol{A}$, $\boldsymbol{B} \cdot \boldsymbol{A}$	Tensor $\boldsymbol{A}$ operating from the right on vector $\boldsymbol{a}$ or tensor $\boldsymbol{B}$
$\boldsymbol{a} \otimes \boldsymbol{b}$, $\boldsymbol{A} \otimes \boldsymbol{B}$	Outer (dyad, tensor) product of vectors $\boldsymbol{a}$ and $\boldsymbol{b}$ or tensors $\boldsymbol{A}$ and $\boldsymbol{B}$
$\boldsymbol{A} : \boldsymbol{B}$	Contraction (scalar product) of tensors $\boldsymbol{A}$ and $\boldsymbol{B}$
$\boldsymbol{A}^{-1}$	Inverse of tensor $\boldsymbol{A}$
$\boldsymbol{A}^{T}$	Transpose of tensor $\boldsymbol{A}$
$\det(\boldsymbol{A})$	Determinant (third invariant) of tensor $\boldsymbol{A}$
$\mathrm{tr}(\boldsymbol{A})$	Trace (first invariant) of tensor $\boldsymbol{A}$

Several acronyms are used throughout this work for the sake of both brevity and convention, and are summarized here.

Acronym	**Meaning**
2D	Two-dimensional
3D	Three-dimensional
BTZ	Brittle Temperature Zone
DSP	Direct Sheet Plant

IC	Inner Curve
IF	Inner Flat
LFC	Longitudinal Facial Crack
NF	Narrow Face
NR	Newton-Raphson
OC	Outer Curve
OF	Outer Flat
SEN	Submerged Entry Nozzle
TC	Thermocouple
WF	Wide Face

CHAPTER 1

INTRODUCTION

1.1. Background

Steel is, both literally and figuratively, the foundation of the modern industrialized world. The use of steel has allowed for the construction of taller buildings, longer bridges, stronger tools, and many other structures and mechanisms that outperform the previous generation. Steel has one of the lowest cost-to-strength ratios relative to other materials, and so has become ubiquitous in the modern world; steel is found in everything from kitchen utensils to heavy earthmoving equipment. At some points and places in history, such as the settling of the North American frontier, steel has been more valuable than precious metals like gold because of its durability in tools such as plows and axes.

The vast majority of steel produced in the world today is done so through a process called continuous casting. Continuous casting, as its name suggests, is a continuous process capable of high production volumes, especially compared to previous batch-based ingot casting. Continuous casting has been responsible for over 90% of the world steel production for several years, which has been in excess of one billion metric tons since the year 2004 [3,4]. The process of continuous casting has its origins with Henry Bessemer some 140 years ago [2], but did not become a major industrial process until the middle of the 20th century with the need for a large amount of steel for second world war and the reconstruction of the European nations, Russia, and Japan in its aftermath. Continuous casting has been evolving since then because of both industrial experience and applied scientific research, but the steel producers and consumers will never cease the demand for a higher volume of product with fewer defects at lower prices.

1.2. Overview of Continuous Casting Process

The important aspects of the continuous casting process are shown in Figure 1.1 [7]. Fluid flow in continuous casting is a gravity-driven process, as few if any pumps can withstand the temperatures at which steel is a liquid. The refined liquid steel from the steelmaking process continues its journey in a large refractory-lined ladle, which is placed above the casting machine. The bottom of the ladle is opened and the steel drains out into a large reservoir called a tundish. While also serving as a refining vessel under optimal conditions, the main purpose of the tundish

is to act as a buffer between ladle changes so that the process can continue without interruption. The steel next flows out of the tundish though a refractory submerged entry nozzle (SEN) into a bottomless, water-cooled, oscillating copper mold. Either a stopper rod within the tundish or a slide-gate mechanism within the SEN regulates the flow of molten steel out of the tundish.

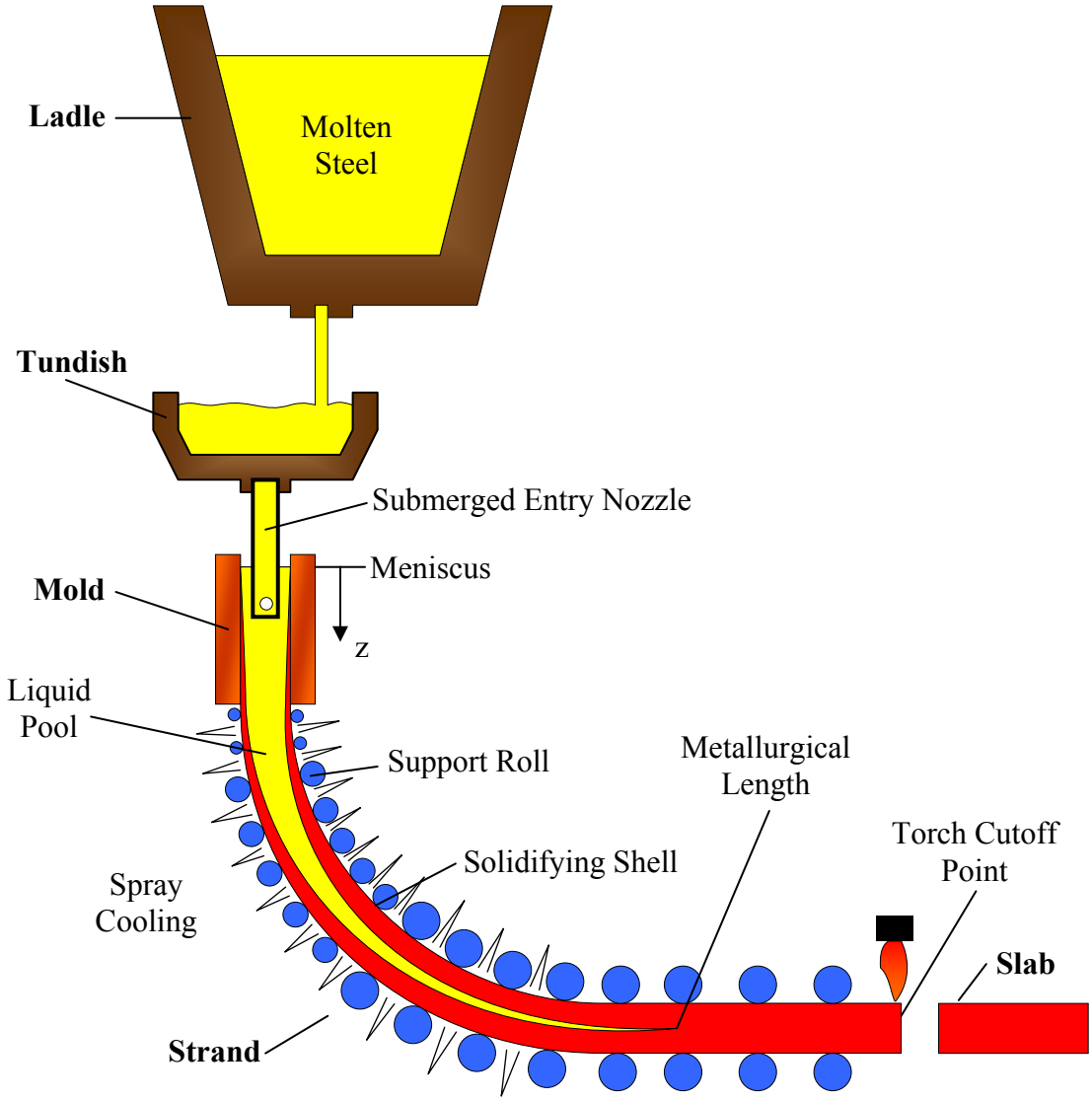

Figure 1.1. Schematic of Continuous Casting Process

The steel freezes soon after initial contact with the mold walls, forming a thin shell of material that is withdrawn continuously at the same rate at which it solidifies, called the casting speed. Upon exiting the mold, the steel travels through a region known as secondary cooling, which generally consists of several banks of nozzles that spray water against the shell between

the supporting (and driving) rolls that guide the steel strand from a vertical to a horizontal configuration. Once the steel strand is completely solidified, a torch or shear cuts the steel strand into separate slabs of a desired length, and then the section of steel continues downstream to further processing, such as hot-rolling, coiling, or whatever processes are required for the final product. Focusing on the section of the process upstream from the cutoff point, steady state conditions (relative to a stationary observer) are eventually obtained and the process normally continues for extended periods of time.

Continuous casting is capable of producing a wide variety of steel grades and shapes, from thick or thin slabs to billets and even near-final shapes such as wide-flanged beams. Each shape and grade present their own unique issues to the continuous casting process, but all possible combinations share the worries of defects or worse, a breakout. A breakout is the failure mechanism that occurs when the steel shell tears open in the secondary cooling zone (though the breakout-initiating problem need not start there), spilling molten steel over the spray nozzles, support rolls, and plant floor. A single breakout can cost steel producers on the order of one million dollars between lost product, damaged equipment, and down time in the plant.

Thin sheet steel has many uses, including automobile bodies, pipelines, and food cans. Conventional slab casting produces slabs around 250 mm thick at a rate of about 1.4 m/min, and several rolling operations are needed to reduce this section size to the around 3-7 mm thickness needed for thin sheet steels. The advent of thin-slab casting in the late 1980s at Nucor's Crawfordsville, Indiana plant with the Compact Strip Production (CSP) mold [5] was the first step in greatly reducing the number of costly rolling operations needed to make thin products. Thin-slab casting produces slabs with thicknesses ranging from 50-100 mm with casting speeds around 5 m/min, and in order to have equal throughput as the conventional process, producers are trying to increase casting speeds to 8 m/min. The main issue that arises in decreasing the mold thickness is that the SEN will no longer fit between the mold plates. As shown in Figures 1.2 and 1.3, mold designers solve this problem by using elliptical (rather than circular) SENs and by introducing a gentle funnel shape into the mold, so that the strand thickness is large at the top of the mold and tapers down into the nominal thickness, hence the term "funnel-shaped mold," or more succinctly, "funnel mold."

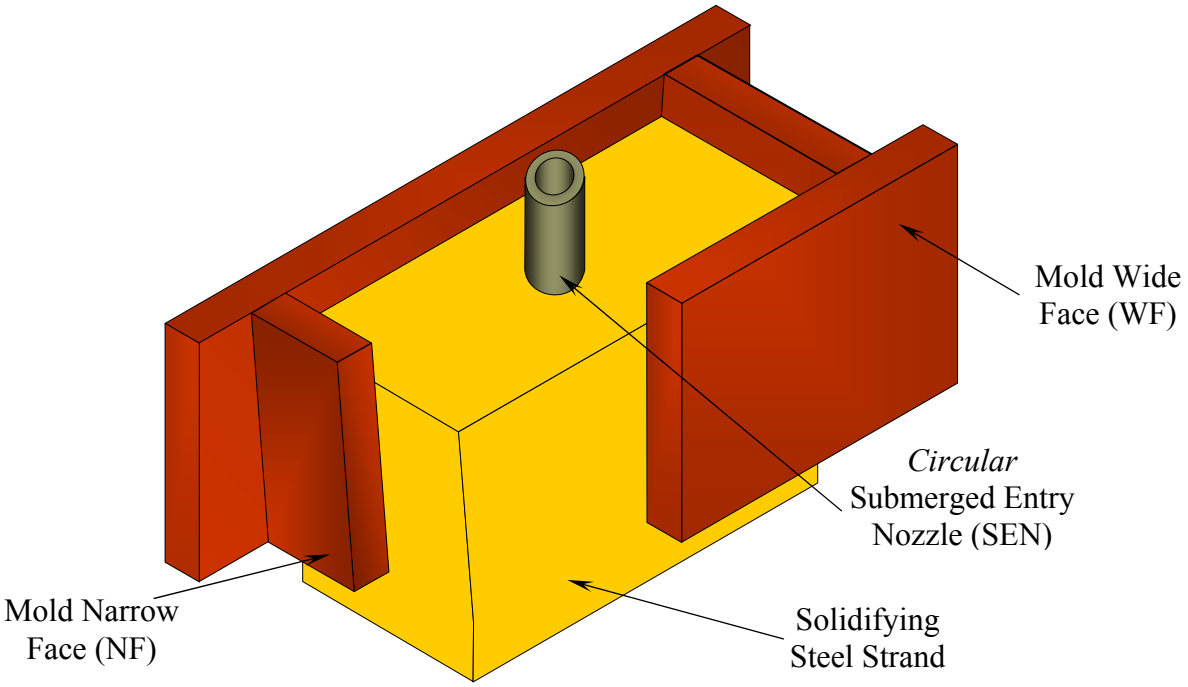

Figure 1.2. Schematic of Conventional Slab Casting Mold

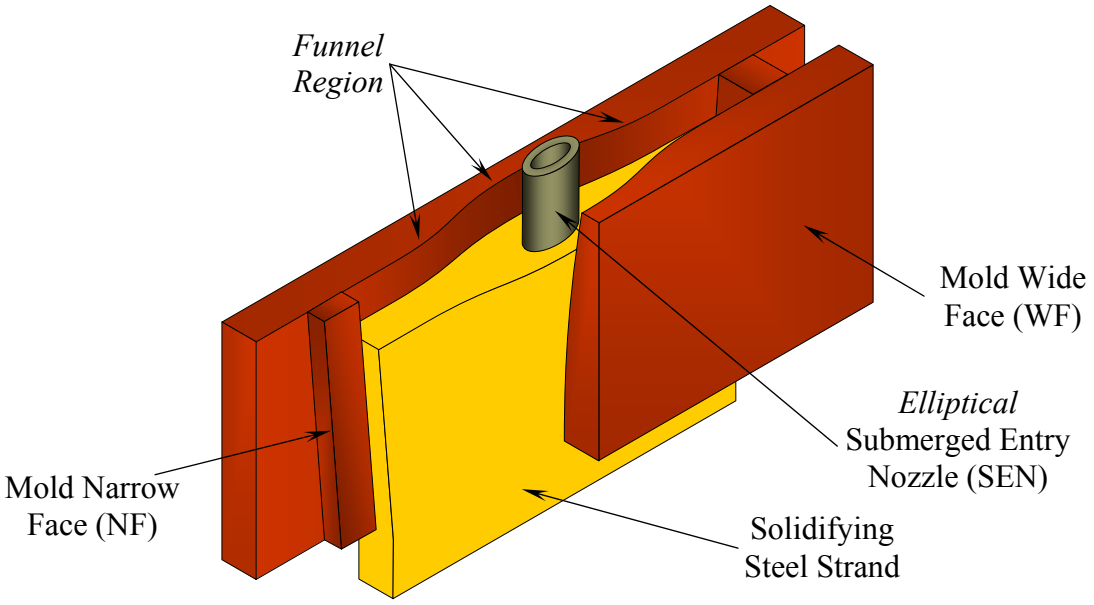

Figure 1.3. Schematic of a Thin-Slab Casting Funnel Mold

1.3. Objectives and Methodology of Current Work

The designs of funnel molds have evolved over the years, based mostly on expensive trial-and-error processes in steel plants. This work aims to lay the groundwork for optimizing funnel mold design for thin-slab continuous casting of steel, based on development and application of a computational model to obtain a fundamental understanding of the effects of the

funnel on the solidifying steel shell, especially with regards to shell cracking and breakouts. Thus, another objective is to understand the various mechanisms of cracking, in funnel molds, which have gone largely unstudied since the inception of the funnel mold. This requires a fundamental understanding of the mechanical behavior of the shell, which in turn needs a quantitative understanding of the heat transfer in both the mold and the shell.

Various modeling techniques are applied to the mold and the shell to qualitatively and quantitatively investigate this phenomenon of longitudinal facial cracking. After discussing the geometry of funnel molds, this work will cover the development and application of the mathematical models. Firstly, the thermal behavior of the mold and shell will be investigated, first using CON1D [6], a one-dimensional numerical model of the continuous casting process. Next, the thermal-mechanical behavior of the shell will be investigated with analytical models, as well as using ABAQUS [1], a commercial general-purpose finite-element code. The results of the coupled thermo-mechanical numerical models will then be used to evaluate the cracking potential in the shell. The models will be validated as much as possible with a database of plant measurements from the Corus Steel Direct Sheet Plant (DSP) in IJmuiden, The Netherlands. They will then be applied to investigate the behavior of the solidifying shell, focusing on the effect of funnel design. Finally, this work will suggest a better design for funnel molds.

1.4. References

1. ABAQUS 6.9 User Manuals, (2009), Simulia Inc., 166 Valley St, Providence, Rhode Island, USA, 02909.
2. H. Bessemer, "Improvement in the Manufacture of Iron and Steel." United States of America Patent, Number 49,053. 25 July 1865.
3. International Iron and Steel Institute, "Continuously-Cast Steel Output, 2004 to 2006." Website, http://www.worldsteel.org/?action=storypages&id=197#, visited 24 February 2008.
4. International Iron and Steel Institute, "Crude Steel Statistics Total 2006." Website, http://www.worldsteel.org/?action=stats&type=steel&period=latest&month=13&year=2006, visited 24 February 2008.
5. H. Malinowski, "First CSP Production Plant at Nucor Steel." *Steel Times*, **217**:11 (1989), pg. 600-603.
6. Y. Meng and B.G. Thomas, "Heat Transfer and Solidification Model of Continuous Slab Casting: CON1D." *Metallurgical and Materials Transactions*, **34B**:5 (2003), pg. 707-725.
7. B.G. Thomas, "Introduction to Continuous Casting." Website, http://ccc.mechse.uiuc.edu/introduction/concast.html, visited 24 February 2008.

CHAPTER 2

MOLD GEOMETRY

2.1. Introduction

Funnel molds, as the name suggests, differ from conventional mold shapes with the introduction of a funnel into the hot face of the wide faces. All other things being equal, the geometry is then the only difference between conventional slab molds and funnel molds. In order to understand the effect of the funnel geometry on the mold and on the solidifying shell, the geometry must first be understood and represented in a format that is compatible with the other models employed in this work. This exercise allows for easy and systematic mesh generation in numerical models as well as the development of various analytical models.

One of the issues that arises in decreasing the thickness of the cast product is that the submerged entry nozzle (SEN) no longer fits between the mold plates. One way around this problem is to use an SEN that has an ellipsoidal cross-section, rather than the traditional circular shape. Another method is to introduce a funnel shape into the mold, so that the strand thickness is larger at the top of the mold and tapers down to the nominal strand dimensions. Both approaches satisfy the design goal of creating space for the SEN; however, a well-designed funnel will seek to maximize the space for the nozzle, to reduce fluid-flow related defects, while minimizing the induced mechanical effects in the steel shell that are otherwise absent without the funnel, as explained in Chapter 5.

A review of the American patents reveals several ideas for funnel molds that the steel industry has produced. Flick *et al.* [2] proposed a funnel mold design with non-parallel "outer flat" regions (see below for description). To promote uniform heat transfer in the mold, Pleschiutschnigg proposed using copper mold plates of constant thickness with a funnel shape introduced into the water box [5]. Grove and Sears [3] suggest changing the depth of the cooling water channels from the hot face of the funnel to offset funnel curvature effects and create a uniform hot face temperature. Struebel [6] and Fehlemann and Struebel [1] promote the idea of changing the water channel size to locally change the velocity of the water channels by adding extra copper to the hot side or cold side of the water channels. This has been implemented practice by retrofitting molds with "accelerator plates" inserted into existing channels to increase local water velocity. Most relevant to the work at hand, Sucker and Capotosti [7] patented a

variety of funnel shapes, including those outlined in this chapter with the claim of reducing defects in the solidifying steel shell. Pleschiutschnigg [4] proposed using different funnel shapes on the inner and outer casting radius, and also tapering the funnel region away from the narrow faces with increasing distance down the mold. However, the utility of these various designs has not been demonstrated, so this work aims to gain a fundamental and quantitative understanding of the effects of the different geometric features on the thermal-mechanical behavior of the solidifying shell and the possible formation of longitudinal cracks.

2.2. Wide Faces

2.2.1. Horizontal Plane

First, consider the horizontal plane of the funnel, i.e. the plane perpendicular to the casting direction. The fundamental features of the funnel shape in this plane are the "inner funnel width," the "outer funnel width," and the "crown." These three features are sufficient to define completely the geometry in the horizontal plane of the funnel, and are all independent of the shape of the funnel in the vertical plane. Some molds used in practice such as the CSP mold have zero inner funnel width; this is a special case of the geometry presented here. Other features of interest include the "strand width" and the "strand thickness," although these features are not unique to funnel molds. Figure 2.1 illustrates the geometric features of a funnel mold.

Funnel molds typically have two planes of symmetry, one through the center of the wide faces and one through the center of the narrow faces. The intersection of these planes suggests a natural coordinate system for the mold, as shown in Figure 2.2, with the positive *z*-axis pointing along the casting direction ("into the page"). Consider in this work the quadrant in the horizontal plane bounded by the positive *x*- and *y*- axes.

Figure 2.2 defines the symbolic funnel dimensions: w_i is half of the inner funnel width, w_o is half of the outer funnel width, w_s is half of the strand width, c is the crown of one wide face, and t_s is half of the strand width in regions away from the funnel. Note that a physically admissible description of the mold surface requires $0 \le w_i < w_o < w_s$. The hot face surface of the mold, $s(x,z)$, is described as a function of these geometric features in the provided coordinate system by applying some basic principles of Euclidean geometry.

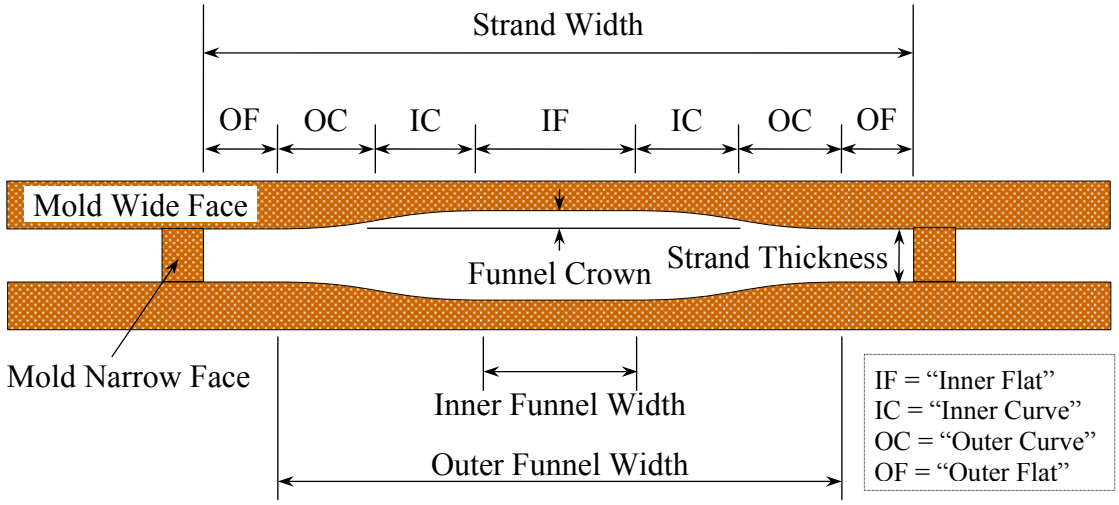

Figure 2.1. Horizontal Plane Funnel Geometry Features (Top View)

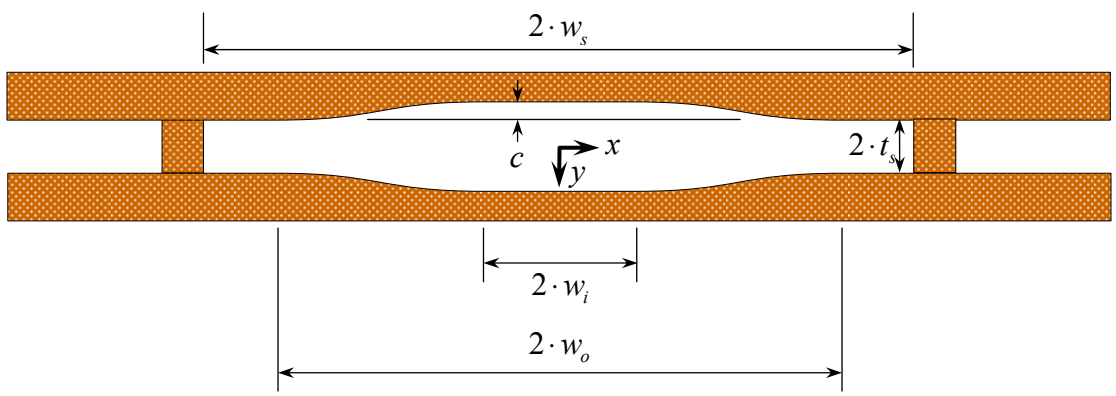

Figure 2.2. Horizontal Plane Funnel Geometry Variables

Some additional terminology is helpful when discussing the funnel geometry. The physical features mentioned earlier lend to subdividing the funnel into its distinct regions. The "inner flat" region, as the name suggests, is the straight segment in the center of the mold, bound by the inner funnel width, $0 \le x \le w_i$. Similarly, the "outer flat" regions are the straight segments in the outermost regions of the funnel, towards the narrow faces, that are bound by the outer funnel width and the strand width (technically the mold width, but for present purposes the strand width is sufficient), $w_o \le x \le w_s$. The region between the funnel widths is the "funnel transition" region, $w_i \le x \le w_o$, which may be further divided into an "inner curve" region and an "outer curve" region, depending on the sign of the local radius of curvature of the surface; the

inner curve region has negative curvature, the outer curve region has positive curvature. All of these additional features are highlighted in Figure 2.1.

The outer flat is one half of the strand thickness away from the center of the narrow faces, $y = t_s$, and the inner flat is further away by a distance equal to the crown of the mold, $y = t_s + c$. In the provided coordinate system, the funnel transition is defined by a curve that connects the (x, y) points $(w_i, t_s + c)$ and (w_o, t_s). The curve that describes the funnel transition is subject to additional constraints to avoid creating a damaging environment for the solidifying steel shell. These constraints are that the curve must be continuous, the curve must be tangent to the flat regions at each endpoint, the curve must be bound entirely by the intervals $w_i \le x \le w_o$ and $t_s \le y \le t_s + c$, and the curve must be monotonic (curvature changes signs at most once). Note that there is no constraint on the symmetry (or anti-symmetry) of the curve. Infinitely many curves meet all of these constraints, but here only three are discussed, the first of which is generally the design used in practice; two circles of equal-but-opposite radius, tangent to each other in the center of the funnel transition region, one-half of a sine wave, and a Bézier curve. These designs are shown in Figure 2.3 for the same funnel dimensions. The different effects of these seemingly similar designs on the mechanical behavior of the shell will be shown later.

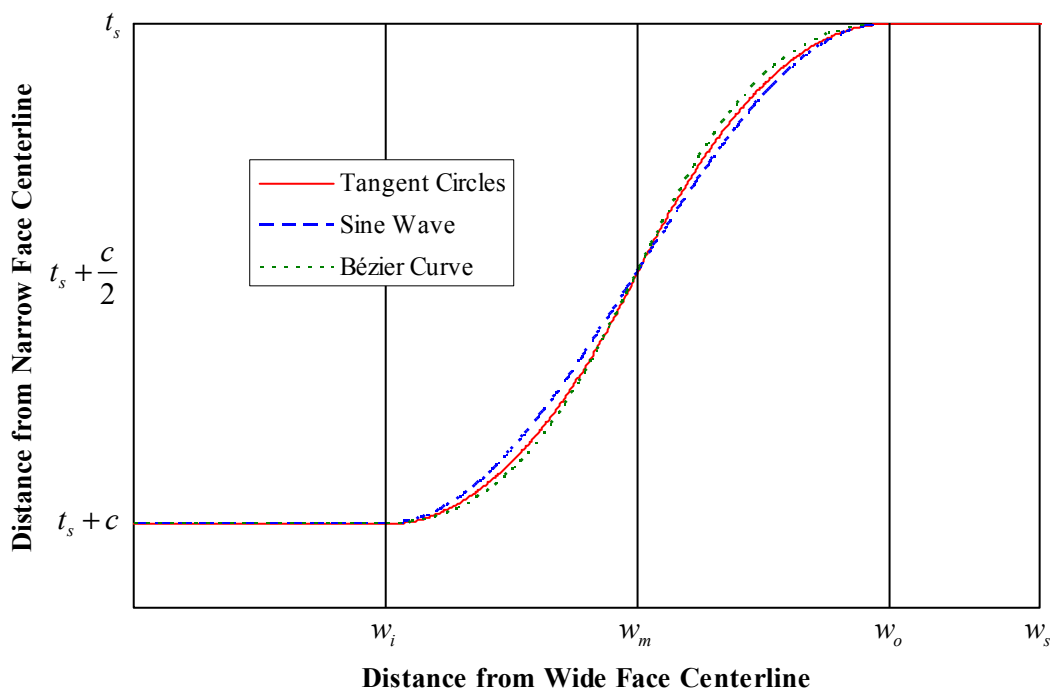

Figure 2.3. Horizontal Plane Funnel Shapes

2.2.1.1. Tangent Circles Design

Consider two circles of equal-but-opposite radius, tangent to the flat sections and to each other in the middle of the funnel transition region, as shown in Figure 2.4. The location of the middle of the funnel region is given by $w_m = (w_i + w_o)/2$. This physical description is sufficient to create a mathematical description of the curve formed by these two circles. Firstly, the (horizontal) radius r_h must be determined by applying the Pythagorean Theorem according to Figure 2.4, and then solving for the radius:

$$r_h^2 = \left(\frac{w_o - w_i}{2}\right)^2 + \left(r_h - \frac{c}{2}\right)^2 \quad \Rightarrow \quad r_h = \frac{c}{4} + \frac{(w_o - w_i)^2}{4 \cdot c} \tag{2.1}$$

The Pythagorean Theorem similarly is employed to locate the points on the hot face in the funnel transition region as a function of the x-coordinate:

$$s(x,z) = t_s + \begin{cases} c & 0 \le x \le w_i \\ c - r_h + \sqrt{r_h^2 - (x - w_i)^2} & w_i \le x \le w_m \\ r_h - \sqrt{r_h^2 - (w_o - x)^2} & w_m \le x \le w_o \\ 0 & w_o \le x \le w_s \end{cases} \tag{2.2}$$

2.2.1.2. Half Sine Wave Design

A portion of a sine wave, $y(x) = c_1 + c_2 \sin(c_3 + c_4 x)$, also meets the constraints for the funnel transition curve, granted the various constants c_i are defined correctly. The hot face of the mold wide face with a half sine wave funnel transition curve is given by:

$$s(x,z) = t_s + \begin{cases} c & 0 \le x \le w_i \\ \frac{c}{2}\left[1 + \sin\left(\frac{\pi}{2} + \pi\left(\frac{x - w_i}{w_o - w_i}\right)\right)\right] & w_i \le x \le w_o \\ 0 & w_o \le x \le w_s \end{cases} \tag{2.3}$$

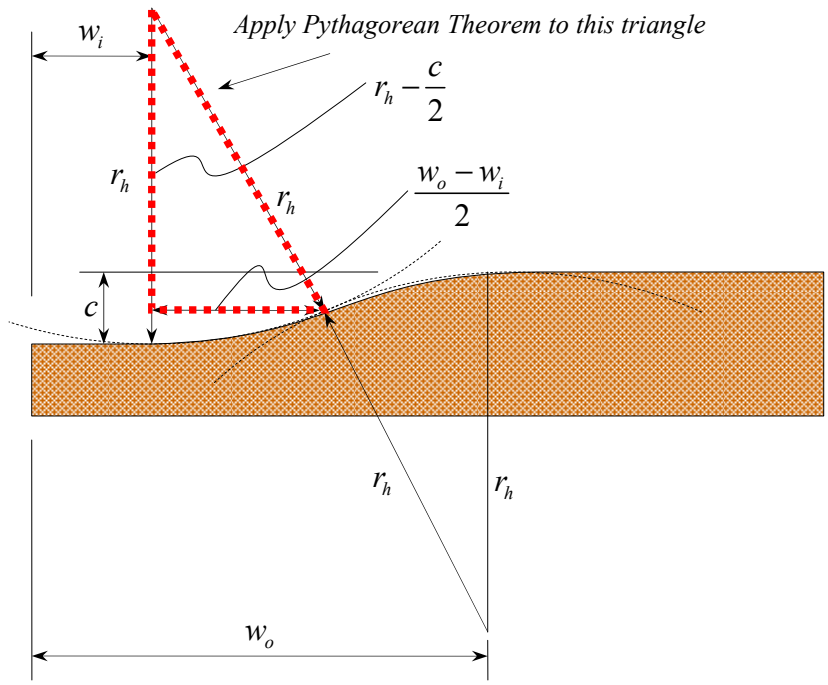

Figure 2.4. Calculation of Horizontal Radius

2.2.1.3. Bézier Curve Design

Bézier curves are parameterized cubic polynomials, commonly used in computer graphics. These curves are continuous and smooth, with a few exceptions, through several derivatives and are easy to compute. Consider any four points in space, with three line segments connecting them. Linearly interpolating along each line segment by the same fraction of unity locates three points in space; now connect these three points with two new line segments. Linearly interpolating along these two line segments by the same fraction of unity locates two new points in space; connect these two points by a new line segment, and linearly interpolate along it by the same fraction of unity to locate a point on the Bézier curve. This series of linear interpolations is known as de Casteljau's algorithm, and is the geometric basis for the Bézier curve. The equivalent mathematical expression for the Bézier curve $\boldsymbol{b}_c(\beta)$ is given by:

$$\boldsymbol{b}(\beta) = (1-\beta)^3 \boldsymbol{b}_0 + 3\beta(1-\beta)^2 \boldsymbol{b}_1 + 3\beta^2(1-\beta)\boldsymbol{b}_2 + \beta^3 \boldsymbol{b}_3 \tag{2.4}$$

where $0 \le \beta \le 1$ is the parametric variable and $\boldsymbol{b}_0$, $\boldsymbol{b}_1$, $\boldsymbol{b}_2$, and $\boldsymbol{b}_3$ are the "control points" of the curve. Choosing $\boldsymbol{b}_0 = (w_i, t_s + c)$, $\boldsymbol{b}_1 = (w_m, t_s + c)$, $\boldsymbol{b}_2 = (w_m, t_s)$, and $\boldsymbol{b}_3 = (w_o, t_s)$ as the (x, y) control points of the Bézier curve gives an anti-symmetric funnel transition curve that meets all of the constraints listed above:

$$s(x,z)=t_s+\begin{cases} c & 0\le x\le w_i \\ \boldsymbol{b}_c(\beta)[y] & w_i\le x\le w_o \\ 0 & w_o\le x\le w_s \end{cases} \tag{2.5}$$

where the operator $[y]$ means to take the y-coordinate of the curve. To use Equation (2.5) in an explicit (non-parametric) manner, the x-coordinate equation of Equation (2.4) is used to solve for β in terms of x, which requires solving a cubic equation:

$$\begin{aligned} x &= (1-\beta)^3 w_i + 3\beta(1-\beta)^2 w_m + 3\beta^2(1-\beta)w_m + \beta^3 w_o \\ &= (w_o - w_i)\beta^3 - \frac{3}{2}(w_o - w_i)\beta^2 + \frac{3}{2}(w_o - w_i)\beta + w_i \end{aligned} \tag{2.6}$$

Cubic equations have three real roots or one real root and two complex roots; so long as x is bound inclusively by w_i and w_o, the principal real root of this equation is given by:

$$\beta(x)=\frac{\psi}{2(w_i-w_o)}-\frac{w_i-w_o}{2\psi}+\frac{1}{2} \tag{2.7}$$

where ψ is given by:

$$\psi=\sqrt[3]{\left[2(w_i+w_o)-4x+\sqrt{5(w_i-w_o)^2+16(x-w_i)(x-w_o)}\right](w_i-w_o)^2} \tag{2.8}$$

This result is substituted into the y-coordinate equation of Equation (2.4), which is then used to define the mold surface:

$$\begin{aligned} y(x) &= (1-\beta)^3(t_s+c)+3\beta(1-\beta)^2(t_s+c)+3\beta^2(1-\beta)t_s+\beta^3 t_s \\ &= \left(2\beta^3-3\beta^2+1\right)c+t_s \end{aligned} \tag{2.9}$$

2.2.2. Vertical Plane

Each of the above funnel designs for the horizontal plane are defined in terms of the crown of the funnel, among other dimensions. Often, the funnel widths are constant in practice, though this is not required by the above equations. Usually, only the crown changes with position down the mold, so it is necessary to define it in terms of the geometric features of the mold. Where the crown becomes zero, the horizontal shape of the mold becomes a straight line (parallel mold walls). Figure 2.5 shows the vertical plane using three physical features to define the funnel: c_T is the crown at the top of the mold, c_B is the crown at the bottom of the mold, and

ℓ_f is the "funnel length." The funnel length is the distance below the top of the mold that the crown changes from a curve to a straight line. Another feature of interest is the "mold length," ℓ_m, which is not unique to funnel molds. The "upper mold" region contains the tapering part of the funnel, $0 \le z \le \ell_f$, while the "lower mold" is vertically straight, though a crown may still be present, $\ell_f \le z \le \ell_m$. A physically admissible mold is constrained to have $0 \le \ell_f < \ell_m$ and $0 \le c_B < c_T$.

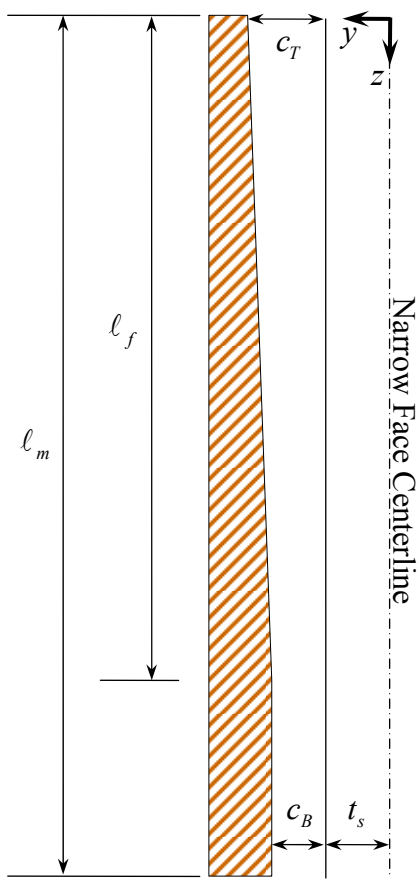

Figure 2.5. Vertical Plane Funnel Geometry Variables (Centerline Slice of Wide Face)

Similar to the horizontal plane, the curve that defines the crown in the vertical plane is constrained so that the curve must be continuous; the curve must be tangent to the line segment that defines the lower part of the mold; the curve must be bound entirely by $t_s + c_B \le y \le t_s + c_T$ and by $0 \le z \le \ell_f$ (with one exception, discussed shortly); and the curve must be monotonic, though preferably the local radius of curvature does not change sign at all. The curve connects

the two (y,z) points $(t_s + c_T, 0)$ and $(t_s + c_B, \ell_f)$. Again, infinitely many curves meet these constraints, but only three are discussed here; the "curved funnel," the "linear funnel," and a Bézier curve.

2.2.2.1. Curved Funnel

The curved funnel consists of an arc that is tangent to the lower mold at the funnel length and sweeps upward. The (vertical) radius in this case is calculated according to the other geometric features by applying the Pythagorean Theorem in a manner similar to the tangent circles case in the horizontal plane.

$$r_v = \frac{c_T - c_B}{2} + \frac{\ell_f^2}{2 \cdot (c_T - c_B)} \tag{2.10}$$

The curve that describes the crown is then given by:

$$c(z) = c_B + \begin{cases} r_v - \sqrt{r_v^2 - (\ell_f - z)^2} & 0 \le z \le \ell_f \\ 0 & \ell_f \le z \le \ell_m \end{cases} \tag{2.11}$$

2.2.2.2. Linear Funnel

The linear funnel consists of a straight line from the top of the mold to a point somewhere near the funnel length; in this case a vertical blending radius is specified so that the "corner" of the line segments is smoothed out and the curve is tangent to both the upper and the lower mold. In this case, the funnel length is slightly longer than the nominal value. The tangent points are located by creating a system of equations after applying the Pythagorean Theorem and the Law of Similar Triangles to the geometry, yielding the Cartesian components of the distance between the tangent points Δ_y and Δ_z:

$$\Delta_y(x) = r_v - \frac{r_v \cdot \ell_f}{\sqrt{\left(s(x,0) - s(x,\ell_m)\right)^2 + \ell_f^2}} \tag{2.12a}$$

$$\Delta_z(x) = \frac{\left(s(x,0) - s(x,\ell_m)\right) \cdot r_v}{\sqrt{\left(s(x,0) - s(x,\ell_m)\right)^2 + \ell_f^2}} \tag{2.12b}$$

where $s(x,0)$ is the funnel surface function evaluated at $z=0$ ($c=c_T$) for any x-coordinate and $s(x,\ell_m)$ is the same function evaluated at $z=\ell_m$ ($c=c_B$). Note that the tangent points are not equal for different points in the funnel transition region. Applying the Law of Similar Triangles again yields the location of the (upper) tangent point z_t on the curve that describes the crown:

$$z_t = \frac{\left[\left(s(x,0)-s(x,\ell_m)\right)-\Delta_y(x)\right]\left[r_v-\Delta_y(x)\right]}{\Delta_z(x)} \tag{2.13}$$

The curve that describes the crown is then given by:

$$c(z) = c_B + \begin{cases} (c_T - c_B)\left(1-\dfrac{z}{\ell_f}\right) & 0 \le z \le z_t \\ r_v - \sqrt{r_v^2 - (z_t + \Delta_z - z)^2} & z_t \le z \le z_t + \Delta_z \\ 0 & z_t + \Delta_z \le z \le \ell_m \end{cases} \tag{2.14}$$

2.2.2.3. Bézier-Curve Funnel

The third case is a Bézier curve in the vertical plane, which when combined with a Bézier curve in the horizontal plane forms what is called a Bézier surface. In general, the description of the curve is identical to that of the Bézier curve in the horizontal plane, using (y,z) control points $\boldsymbol{b}_0 = (c_T, 0)$, $\boldsymbol{b}_1 = \left(c_B + \phi\cdot(c_T - c_B), \eta\cdot\ell_f\right)$, $\boldsymbol{b}_2 = \left(c_B, \gamma\cdot\ell_f\right)$, and $\boldsymbol{b}_3 = \left(c_B, \ell_f\right)$. $0 \le \phi \le 1$ is a parameter that locates the y-coordinate of the top control point, $0 \le \eta \le \gamma$ is a parameter that locates the z-coordinate of the top control point, and $\eta \le \gamma \le 1$ is a parameter that locates the z-coordinate of the bottom control point. The curve that describes the funnel crown is given by:

$$c(z) = \begin{cases} \boldsymbol{b}_c(\beta)[y] & 0 \le z \le \ell_f \\ c_B & \ell_f \le z \le \ell_m \end{cases} \tag{2.15}$$

Again, the z-coordinate equation is used to solve explicitly for β:

$$\begin{aligned} z &= (1-\beta)^3\, 0 + 3\beta(1-\beta)^2\,\eta\ell_f + 3\beta^2(1-\beta)\gamma\ell_f + \beta^3\ell_f \\ &= (1+3\eta-3\gamma)\ell_f\beta^3 + 3(\gamma-2\eta)\ell_f\beta^2 + 3\eta\ell_f\beta \end{aligned} \tag{2.16}$$

This cubic equation is more difficult to solve than the horizontal plane Bézier curve, so a numerical solution is recommended, choosing the real root that gives $0 \le \beta \le 1$, and then proceed to substitute β into the y-coordinate equation of Equation (2.15), which then gives the crown curve:

$$\begin{aligned} y(z) &= (1-\beta)^3 c_T + 3\beta(1-\beta)^2 \left(c_B + \phi(c_T - c_B)\right) + 3\beta^2(1-\beta)c_B + \beta^3 c_B \\ &= c_T + \left[(3\phi-1)\beta^3 + 3(1-2\phi)\beta^2 + 3(\phi-1)\beta\right](c_T - c_B) \end{aligned} \tag{2.17}$$

2.3. Narrow Faces

The main feature to describe on the narrow faces is the taper that is applied to the mold pieces to ensure that the shell and mold remain in good contact, accounting for solidification shrinkage. Tapers used in practice are usually linear, bilinear, or parabolic, which are simple to describe mathematically. However, definitions of taper vary from plant to plant, so only the linear case is presented here. Given a difference in narrow face mold position from top to bottom δ_{NF}, and assuming the strand width is defined at the bottom of the mold, the Law of Similar Triangles gives an expression for the hot face of the narrow faces:

$$s(y,z) = w_s + \delta_{NF}\left(1 - \frac{z}{\ell_m}\right) \tag{2.18}$$

This is the most general way of defining linear narrow face taper; it is up to the user to calculate δ_{NF} correctly according to plant practice.

2.4. Funnel Volume

Another aspect of funnel design is the cost of machining a mold. Modern milling machines are capable of handling reasonably complicated geometries, so the remaining difference in machining cost is the volume of scrap that ends up on the shop floor, after both the initial machining and any subsequent machining that is performed as the mold is used and wears from the sliding contact with the steel shell. The above equations describing the geometry can be integrated to calculate the volume of copper V_f that must be removed to machine (initially) a given design, and allow another way to compare funnel designs:

$$V_f = \int_0^{\ell_m}\int_0^{w_s} \left(s(x,z) - t_s\right) dxdz \tag{2.19}$$

When the crown curve is not a function of the x-coordinate (the linear funnel, for which a numerical integration would be much simpler), the above-described geometries are anti-symmetric curves and the x-direction integral is very simply $(c/2)(w_i + w_o)$, and all that remains is to integrate the crown curve with this additional constant. For the radiused funnel, the volume of the funnel region is given by:

$$V_f = \frac{w_i + w_o}{2}\left[c_B \ell_m + \ell_f\left(r_v - \frac{\sqrt{r_v^2 - \ell_f^2}}{2}\right) + \frac{r_v^2}{2}\arctan\left(\frac{-\ell_f}{\sqrt{r_v^2 - \ell_f^2}}\right)\right] \tag{2.20}$$

Though the Bézier-curve funnel (in the vertical plane) describes a crown that is independent of the x-coordinate, the integrals quickly become analytically intractable, and a numerical integration method should be applied.

2.5. Present Work

This work considers funnel shapes with "tangent circles" design in the horizontal plane, with either the "curved" or "linear" funnel design in the vertical plane. For the curved funnel design, the geometry is completely specified by providing the inner funnel width w_i, the outer funnel width w_o, the mold length ℓ_m, the funnel length ℓ_f, and the crowns at the top and bottom of the mold c_T and c_B. The geometry for the linear funnel design requires these same dimensions in addition to the blending radius in the vertical plane r_v.

The different funnel shapes analyzed in this work are labeled simply "A," (curved) "B," (linear) and "C," (curved). These three funnels will be the base cases for most of the studies done in this work. In addition, the geometric parameters have been systematically varied to understand their effects on funnel mold design. The geometric parameters are summarized in Table 2.1 and Figures 2.6, 2.7, and 2.8. All cases have mold length ℓ_m = 1100 mm and funnel length ℓ_f = 850mm. From these parameters, the vertical radius of the A-type or C-type molds, r_v, is calculated with Equation (2.10), which is then used to calculate the crown, $c(z)$, at any position below the top of the mold with Equation (2.11). Once the crown is known, the size of the horizontal funnel radius, r_h, is calculated with Equation (2.1). Finally, the position of the hot face, $s(x,z)$, can be calculated anywhere across and down the mold surface with Equation (2.2)

for the "tangent circles" funnel design. The same procedure is used for the B-type mold, except that the vertical radius is specified and used to calculate the tangency adjustments Δ_y and Δ_z in Equations (2.12), allowing the position of the tangent point to be calculated with Equation (2.13). The crown for the linear funnel is then specified at any point below the top of the mold according to Equation (2.14), and then the horizontal radius and hot face position can be calculated as described above.

Table 2.1. Summary of Funnel Geometries Used in this Work

Label	Design	Funnel Geometry (mm)								
		ℓ_f	ℓ_m	w_i	w_0	c_T	c_B	r_v	$r_h(z=0)$	$r_h(z=\ell_m)$
A	Curved	850	1100	130	375	23.4	8	*23465*	*647.14*	*1877.8*
B	Linear	850	1100	130	475	30	0	2500	*999.4*	∞
C	Curved	850	1100	0	475	30	0	*12057*	*1887.7*	∞

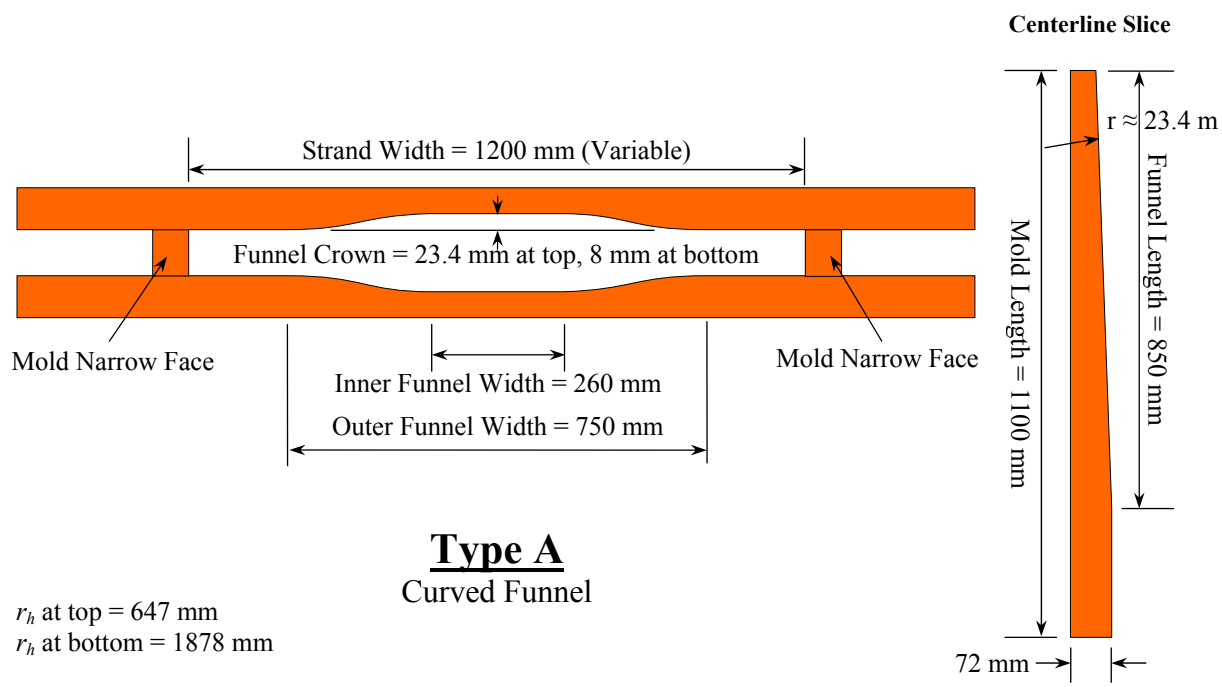

Figure 2.6. Geometry of Funnel Type A

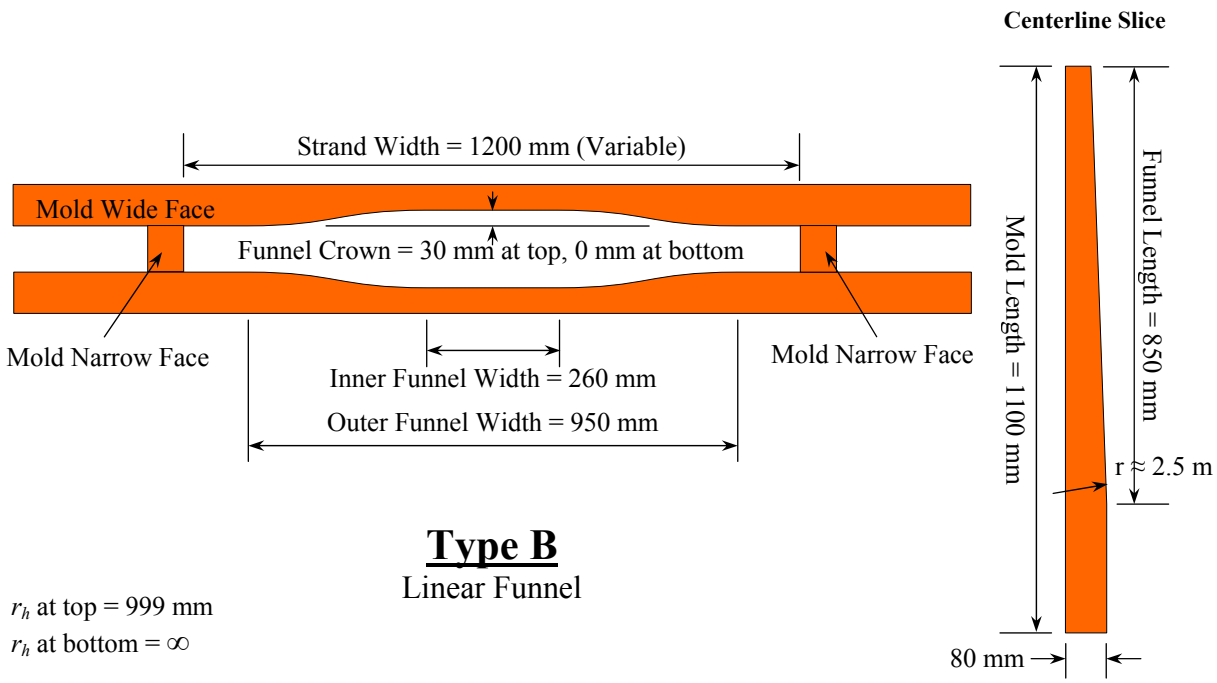

Figure 2.7. Geometry of Funnel Type B

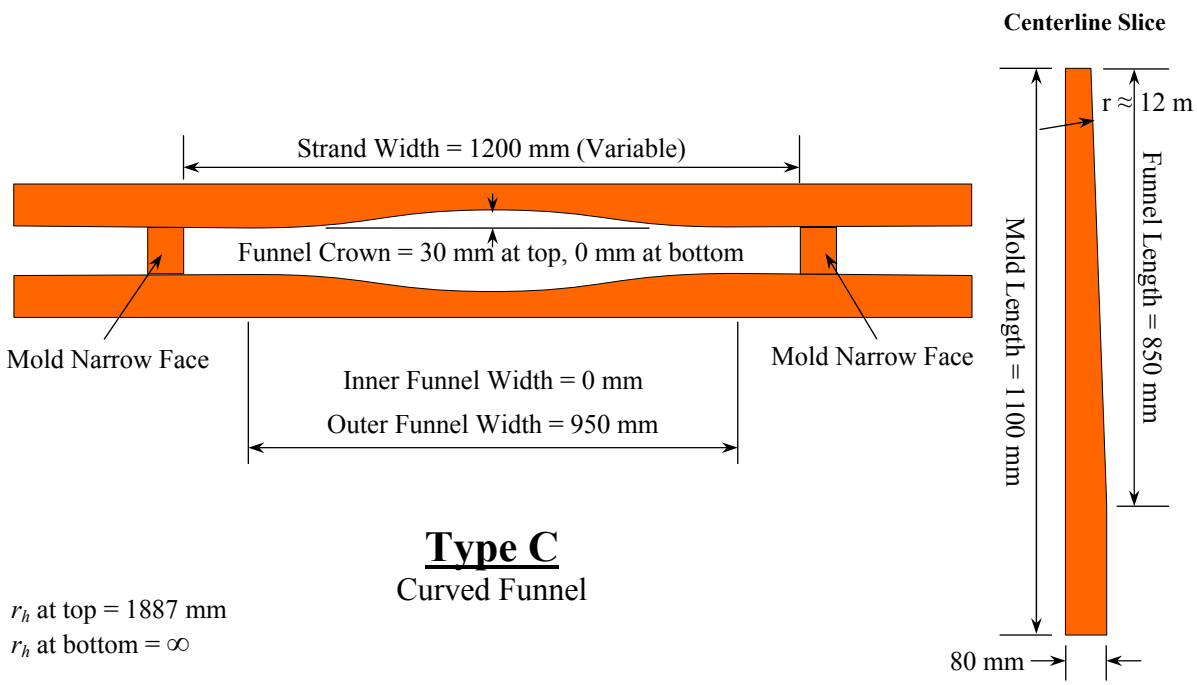

Figure 2.8. Geometry of Funnel Type C

2.6. References

1. G. Fehlemann and H. Streubel, "Continuous Casting Mold for Liquid Metals, Especially for Liquid Steel." United States of America Patent, Number 7,363,958. 29 April 2008.
2. A. Flick, G. Lettmayr, H. Eidinger, F. Wimmer, W. Jahn, and J. Watzinger, "Continuous Casting Mold." United States of America Patent, Number 6,585,029. 1 July 2003.
3. J.A. Grove and J.B. Sears, "Continuous Casting Mold and Method." United States of America Patent, Number 5,927,378. 27 July 1999.
4. F.-P. Pleschiutschnigg, "Optimized Shapes of Continuous Casting Molds and Immersion Outlets for Casting Slabs of Steel." United States of America Patent, Number 5,941,298. 24 August 1999.
5. F.-P. Pleschiutschnigg, "Continuous Casting Mould." United States of America Patent, Number 6,273,177. 14 August 2001.
6. H. Streubel, "Continuous Casting Mold." United States of America Patent, Number 6,474,401. 5 November 2002.
7. J. Sucker and R. Capotosti, "Funnel Geometry of a Mold for the Continuous Casting of Metal." United States of America Patent, Number 6,390,176. 21 May 2002.

CHAPTER 3

MOLD HEAT TRANSFER

3.0. Overview

The first step to understanding the thermal and mechanical behavior of the solidifying shell is to understand the heat transfer in the mold. Mold heat transfer is also important in its own right for understanding and quantifying the impact of funnel shape design. Some of the easiest plant measurements to obtain and use for validating numerical models are the temperatures from the thermocouples embedded in the mold plates. Calibration of such models requires the accurate prediction of the relationship between the mold temperatures and the shell-mold interfacial heat flux. Clearly, an accurate mold heat transfer model is needed for the current work, and the development of such is the subject of this chapter. The majority of the content of this chapter is published in the literature [14,15], though some new content is available here. This work was a collaborative effort with Corus researchers and plant personnel at the Direct Sheet Plant (DSP). Plant measurements and the parametric study using the one-dimensional model, CON1D, were provided by B. Santillana, A. Hamoen, A. Kamperman, and W. van der Knoop. The finite element models presented in this chapter were built and applied by L. Hibbeler.

3.1. Introduction

Mold heat transfer is important to mold life, slab surface quality, breakouts, and many other aspects of the steel continuous-casting process. Heat transfer in funnel molds has been investigated in only a few previous studies, examining heat flux profiles [12], mold distortion and cracking [11,12,13], phenomena in the steel/flux interface [3,8,9,16], and fluid flow coupled with solidification heat transfer [10]. Heat flux tends to be higher in thin-slab casting than in conventional billet or slab casting, which is attributed to the higher casting speeds [12]. Computational models can reveal insights into mold heat transfer, so long as they have been calibrated with plant data. Recent modeling studies of billet casting, which use thermocouple measurements and inverse heat transfer calculations to determine the heat flux profile, have shown that mold hot-face temperature increases with increasing mold plate thickness and casting speed [2,18,19]. Another such model, CON1D [7], simulates one-dimensional heat transfer in

the mold, interface, and solidifying shell [9], and has shown how interfacial slag properties affect heat transfer and lubrication [8].

In the present study, the CON1D model is applied to simulate high-speed thin-slab casting in a funnel mold. To account for the multidimensional thermal behavior around the cooling channels of the funnel mold, a three-dimensional finite-element model, developed using ABAQUS [1], is applied to find correction factors that enable CON1D to predict accurately the temperature at thermocouple locations. The model calculations have been validated using an extensive database of plant data obtained from the Corus Direct Sheet Plant (DSP) in IJmuiden, The Netherlands, including measurements of mold powder consumption, oscillation mark shape, mold temperature, and heat removal. The improved CON1D model is applied here to predict casting behavior for different speeds and to investigate the effect of mold plate thickness. The results will be used to extrapolate standard practices to higher casting speeds and new mold designs, and will also be used to create a calibrated thermo-mechanical numerical model of the solidifying steel shell in Chapters 4 and 5.

3.2. CON1D Model Description

The heat transfer model CON1D simulates several aspects of the continuous casting process, including shell and mold temperatures, heat flux, interfacial microstructure and velocity, shrinkage estimates to predict taper, mold water temperature rise and convective coefficient, interfacial friction, and many other phenomena. The heat transfer calculations are one-dimensional through the thickness of the shell and interfacial gap with two-dimensional conduction calculations performed in the mold.

Heat transfer in the mold is computed assuming a slab with attached rectangular fins that form the cooling-water channels. The process parameters used in this analysis are typical values used with the Corus DSP thin-slab continuous-casting machine. Key parameters include a strand thickness in the mold of 90 mm, low carbon steel poured at 1545 ºC, and a meniscus level of 100 mm below the top of the 1100 mm-long funnel mold. The casting speeds used in model calibration are 4.5 m/min for the narrow face and 5.2 m/min for the wide face. The different casting speeds were used to show that the correction factors calculated in this work depend only on mold geometry. To model accurately the complex geometry of the mold and water slots on

both faces, geometry modifications and an offset methodology [6] are applied to calibrate the CON1D model to match the temperature predictions of a full 3D finite element model.

3.2.1. Narrow Face

To create the simple mold geometry for CON1D, the actual narrow face cross-section was transformed into the one-dimensional rectangular channel geometry (dotted lines), as shown in Figure 3.1. The bolt holes are 22 mm in diameter and 20.5 mm deep; the thermocouple holes are 4 mm in diameter and extend into the mold such that they are 20 mm beneath the hot face. To approximate the actual geometry, the shortest distance between the water channels and the hot face was maintained at 24 mm and the pitch between the channels similarly was set to 12 mm. To match the water flow rate, the dimensions of the rectangular channels were chosen to keep the cross-sectional area nearly the same as that of the actual 14 mm diameter channels. In addition, to maintain heat transfer characteristics, the channel width was chosen to be about two-thirds of the diameter of the actual round channel. These two considerations yield a 9 mm by 17 mm channel and a 41 mm thick mold. CON1D aims only to model a typical section through the mold and cannot predict variations around the mold perimeter, such as corner and funnel effects.

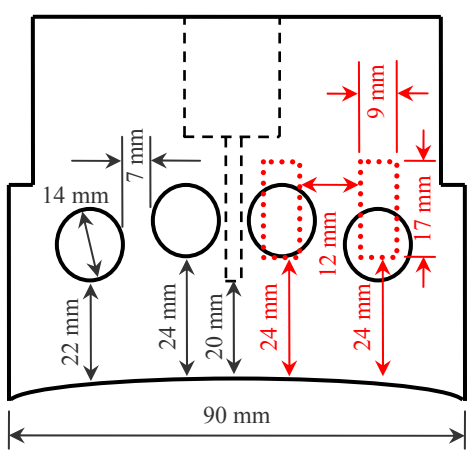

Figure 3.1. Narrow Face Mold Geometry and CON1D Simplification

3.2.2. Wide Face

Water channels in the wide face required similar dimensional adjustments for CON1D. The actual water channels are spaced 5 mm apart and are 5 mm wide by 15 mm deep with rounded roots. The CON1D water channels are 5 mm wide but only 14 mm deep, so that filled area equals the hatched area in Figure 3.2, and the cross sectional area again roughly equals that

of the actual channel. The mold thickness was maintained at 35 mm. As shown in Figure 3.3, this keeps the channels at a constant distance of 21 mm from the hot face, in comparison with the real mold, where closest point of the rounded channel root is 20 mm from the hot face. The bolt holes have the same dimensions as on the narrow face, but on the wide face the thermocouple holes extend into the mold such that they are 15 mm from the hot face.

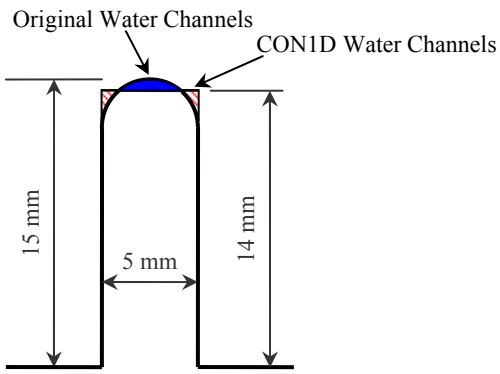

Figure 3.2. Wide Face Water Slot and CON1D Simplification

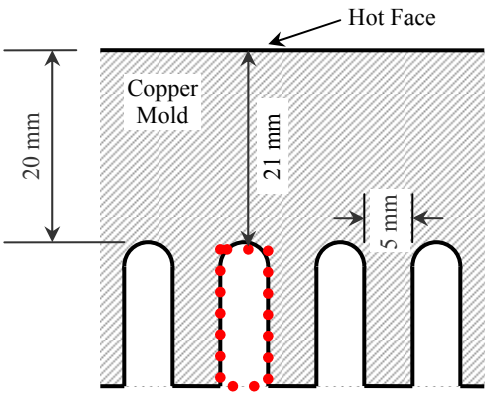

Figure 3.3. Wide Face Mold Geometry

3.3. CON1D Model Offset Determination

To enable CON1D to predict accurately the thermocouple temperatures, it was calibrated using a three-dimensional heat transfer calculation to determine an offset distance for each mold face to adjust the modeled depth of the thermocouples.

3.3.1. Narrow Face

Two different three-dimensional heat transfer models were developed of the mold copper narrow faces using ABAQUS. The first was a small, symmetric section of the mold geometry containing one quarter of a single thermocouple, which was used to determine the offset for CON1D. The second was a complete model of one symmetric half of the entire mold plate, used to determine an accurate temperature distribution including the effects of all geometric features and to evaluate the CON1D model.

To properly compare the finite-element model with CON1D, identical conditions were applied to both models. Figure 3.4 shows the location of a typical repeating portion of the entire mold plate, and Figure 3.5a shows the mesh and simplified boundary conditions used for this calibration domain. The applied heat flux q = 2.6 MW/m² to the hot face is constant and

uniform, as are the thermal conductivity k = 350 W/(m·K) of the mold, the convective heat transfer coefficient h_c = 40 kW/(m²·K) and the water temperature T_∞ = 36 ºC applied to the water channel surfaces. Unlabelled surfaces are insulated (q = 0). The finite-element mesh used 45840 hexahedron, tetrahedron and wedge quadratic finite elements and ran in 80 seconds (wall clock) on a 2.0 GHz Intel Core2 Duo PC.

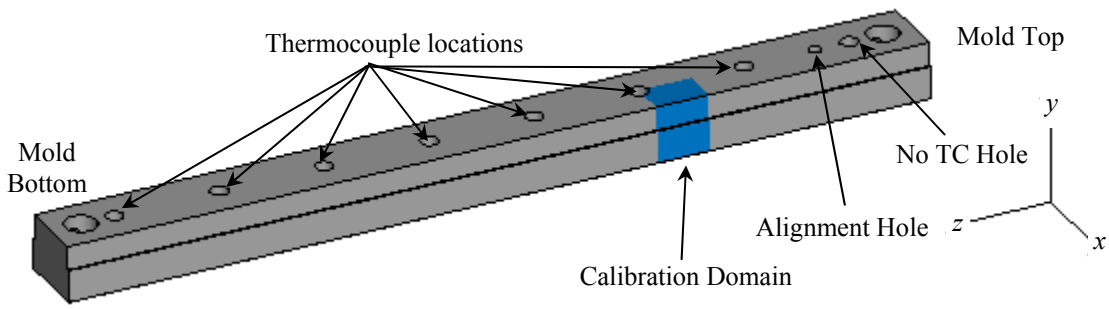

Figure 3.4. Location of Narrow Face Calibration Domain

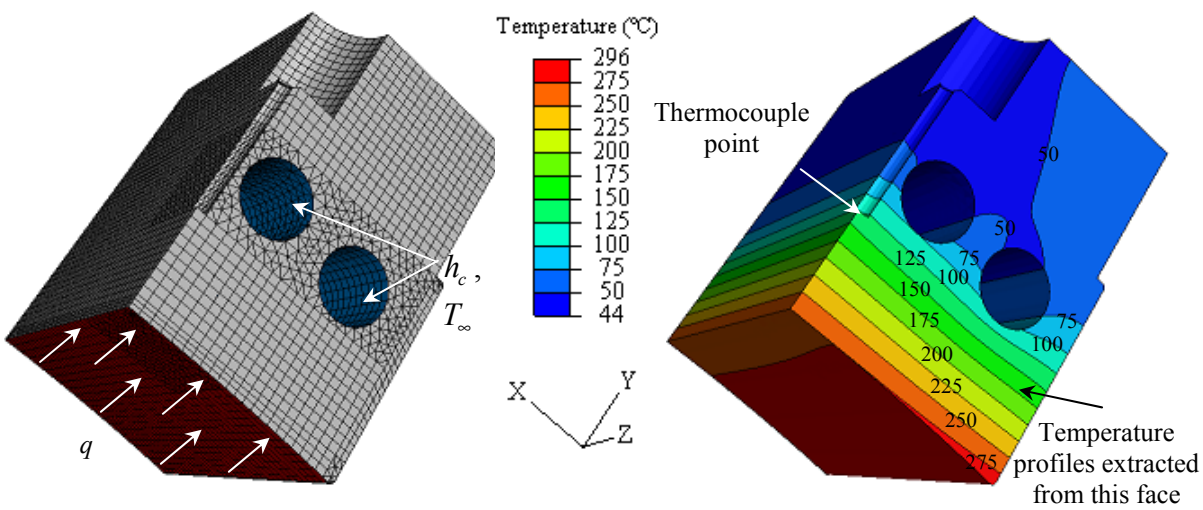

Figure 3.5. Narrow Face Model, Boundary Conditions, and Calibration Results

Figure 3.5b shows the computed three-dimensional temperature contours and identifies the location of the thermocouple, as well as the face from which further data were extracted. The maximum temperature of 296 ºC is found on the hot face corner, which is 20.5 ºC hotter than the hot face centerline. The temperature profiles along four paths are shown in Figure 3.6, in which a linear temperature gradient is evident between the hot face and the water channels. The temperature variation between these paths is small, with only 2 ºC difference across the hot face in the vicinity of the paths. The lowest temperature is found on the back (cold face side) of the

water channel (Path 3). However, the missing copper around the thermocouple causes the local temperature to rise about 10 ºC. To account for this effect in CON1D, an offset distance is applied to the simulated depth of the thermocouples.

An offset distance enables the one-dimensional model to relate accurately thermocouple temperatures by accounting for three-dimensional conduction effects from the complex local geometry [6]. The "offset" is the difference in position between the thermocouples in the mold and in the model, and is the distance the thermocouple position is shifted when input to CON1D.

Figure 3.7 compares the temperature distribution of CON1D with the Path 1 results from Figure 3.6. Although CON1D cannot capture the localized effects of the complex geometric features, the three-dimensional thermocouple temperature can be found by "moving" the thermocouple to a new location closer to the hot face. This small "offset distance," allows accurate thermocouple temperatures to be predicted by CON1D. The offset value can be determined from Equation (3.1) using the CON1D temperature profile as follows:

$$d_{offset} = \left(T_{TC} - T_{hf}\right)\frac{dx}{dT} - d_{TC} = \left(139.7 - 273.16\right)\frac{30}{50.21 - 273.16} - 20 = 2.05\,\text{mm} \tag{3.1}$$

where d_{offset} is the offset distance, T_{TC} is the thermocouple temperature from the 3D model, T_{hf} is the hot face temperature from CON1D, dx/dT is the reciprocal of the temperature gradient in the mold from CON1D, and d_{TC} is the actual depth of the thermocouple from the hot face.

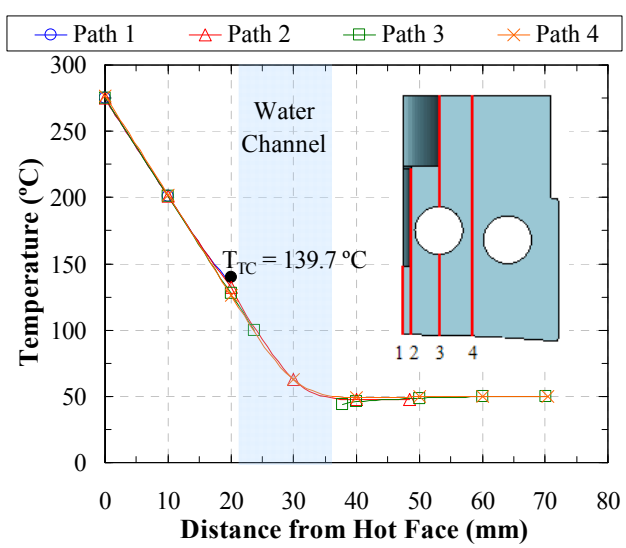

Figure 3.6. Temperature Profiles in Narrow Face

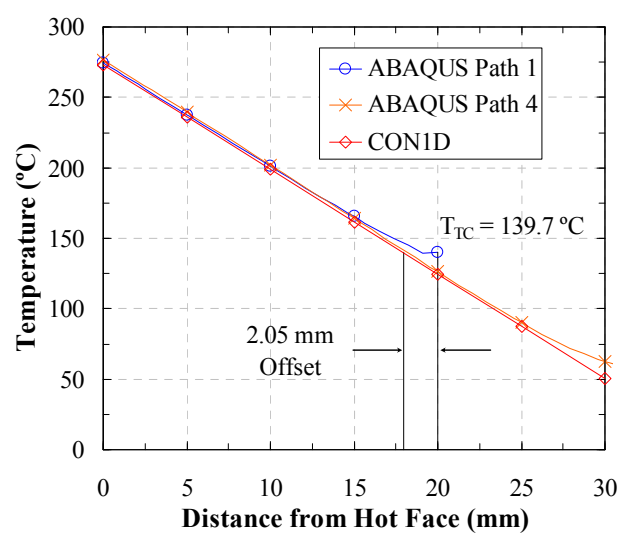

Figure 3.7. Determination of Offset

Figure 3.7 shows that CON1D is able to match the three-dimensional results from the hot face to the water channel roots. Its accuracy drops in the non-linear water-channel regions of the mold, and near the thermocouple location, where matching is achieved by via the offset method.

3.3.2. Wide Face

Following the same procedure used in the narrow face, the offset distance for the wide face was also calculated. Figure 3.8 shows a symmetric half of the wide face mold, and highlights the location of the calibration section. The boundary conditions and properties were maintained the same as in the narrow face. A top view of these conditions and the three-dimensional temperature distribution is plotted in Figure 3.9. The thermocouples in the real wide face are positioned 15 mm from the hot face. The offset was found to be 2.41 mm, meaning that the thermocouples in CON1D should be 2.41 mm closer to the hot face in order to produce accurate thermocouple predictions.

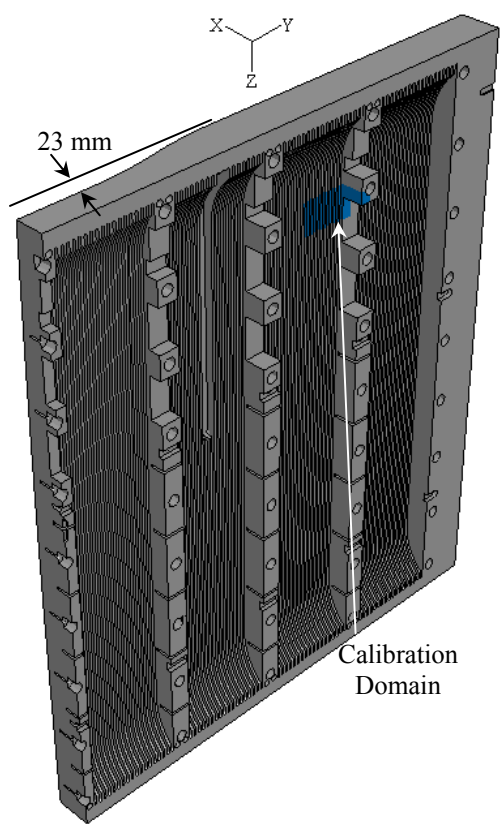

Figure 3.8. Location of Wide Face Calibration Domain

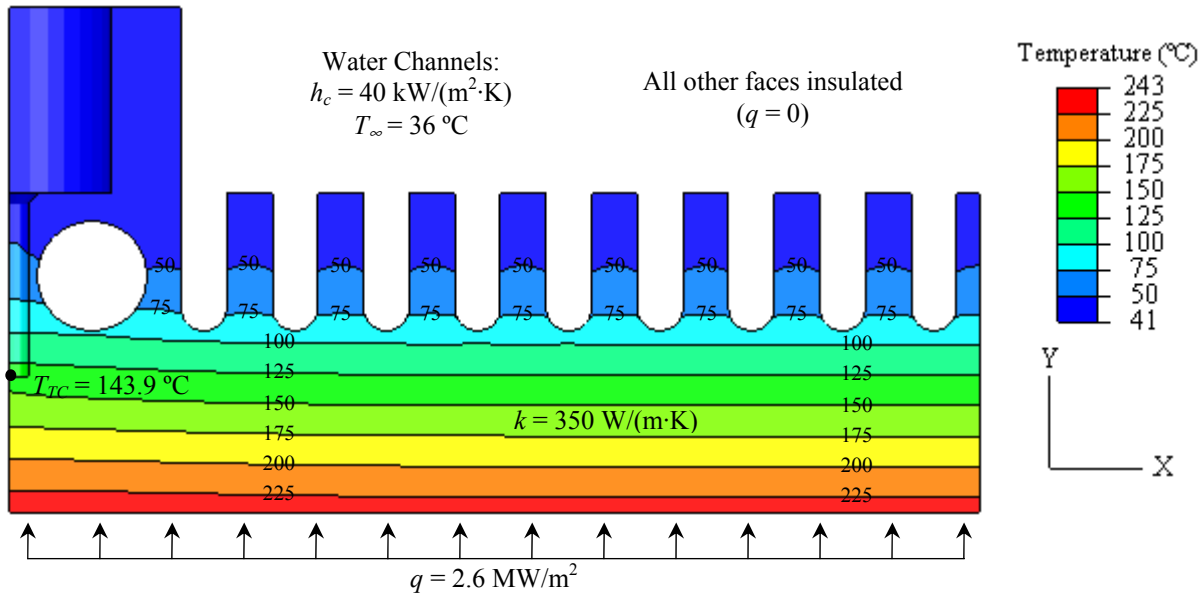

Figure 3.9. Wide Face Calibration Domain with Input Parameters

3.4. Three-Dimensional Mold Temperatures and CON1D Model Verification

Having calibrated the CON1D model by determining the offset distance, both the full three-dimensional model and CON1D simulation were run using realistic boundary conditions for the mold.

3.4.1. Narrow Face

One symmetric half of the entire three-dimensional narrow face geometry was analyzed in ABAQUS, using the DFLUX and FILM user subroutines to realistically vary the heat flux and water temperature down the mold, as given in Figure 3.10. The thermal conductivity and water channel boundary conditions were not altered from the calibration model. This ABAQUS model used 468583 quadratic tetrahedron elements and required 7.1 minutes (wall clock) to analyze. Figure 3.11 shows the temperature contours from the three-dimensional model of the entire mold narrow face. Localized three-dimensional effects are observed near the peak heat flux region and at mold bottom. The cooler spot around the centre of the hot face corresponds to an inflection point in the heat flux curve. The highest temperatures occur at the small, filleted corners of the mold at the peak heat flux because those locations are furthest away from the water channels.

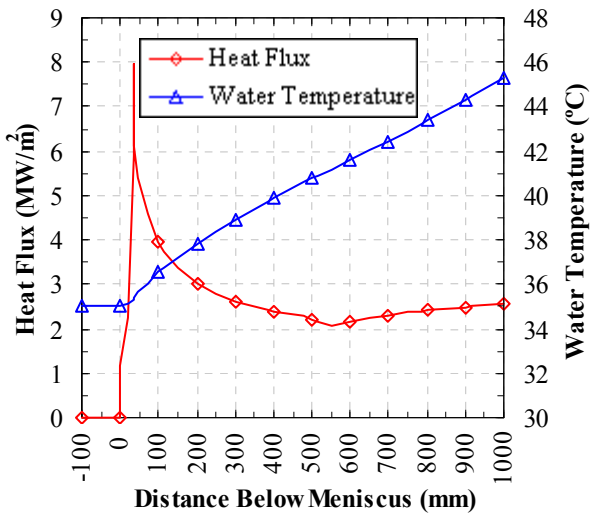

Figure 3.10. CON1D Output Heat Flux and Water Temperature Profiles

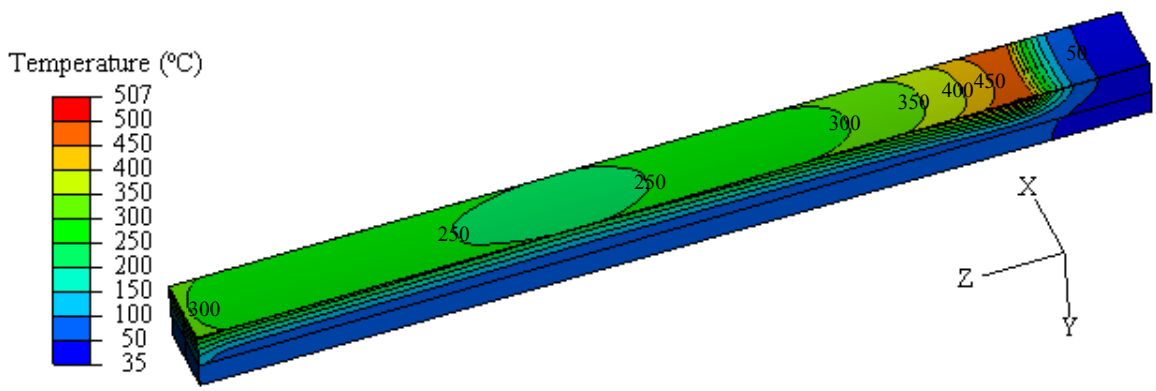

Figure 3.11. Narrow Face Three-Dimensional Model Temperature Results

Figure 3.12 shows the three-dimensional hot face temperatures extracted along the mold centerline compared with the hot face temperatures from CON1D. The two models match very well (typically within 2 ºC) except around the areas with strong three-dimensional effects. Maximum errors are 9.2 ºC near the heat flux peak and 27 ºC at mold bottom, where the water slots end and no longer receive the fin enhancement to the heat transfer.

Figure 3.13 shows the temperature contours around the area of peak heat flux, highlighting the localized thermal effects at this location. Although the CON1D model is least accurate at the hot face at this location, its two-dimensional mold temperature calculation in the vertical slice allows it to achieve acceptable accuracy.

The temperatures predicted at all seven of the thermocouple locations in the mold compare closely with the offset CON1D values in Figure 3.12. The topmost of the eight bolt

holes does not have a thermocouple and the middle hole in Figure 3.13 is for alignment. The results are tabulated in Table 3.1 and illustrated in Figure 3.12. The temperatures match almost exactly (within 1.4 ºC or less), which is within the finite-element discretization error. This is a great improvement over the error of 12 to 21 ºC produced by CON1D without the offset.

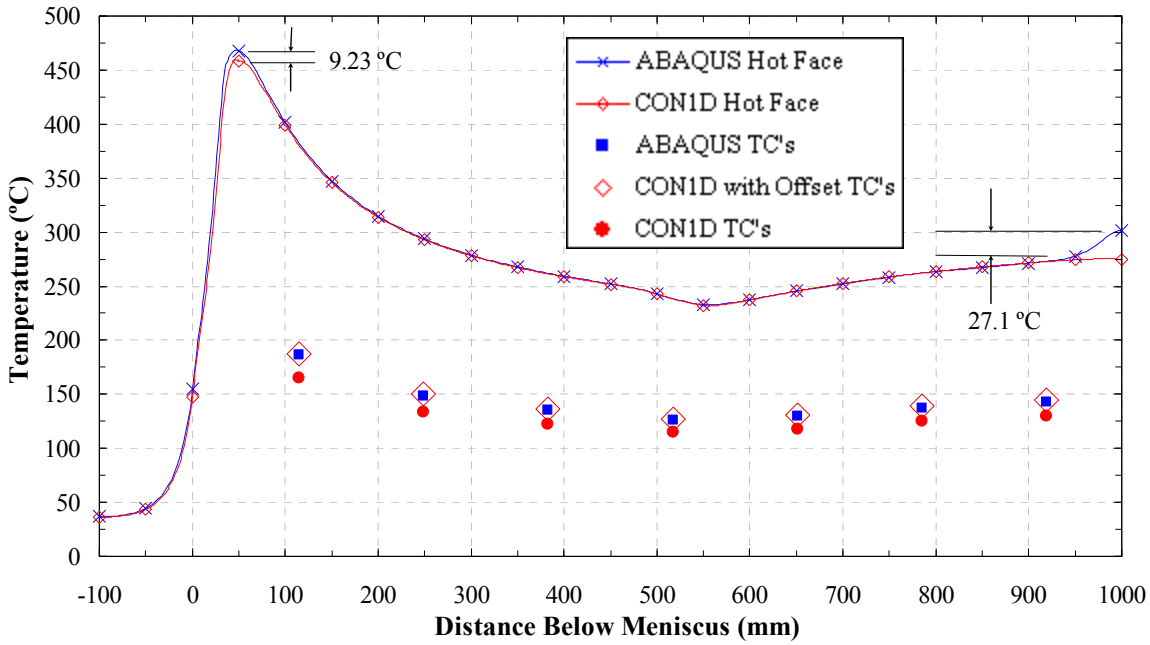

Figure 3.12. Narrow Face Hot Face and Thermocouple Temperatures Comparison

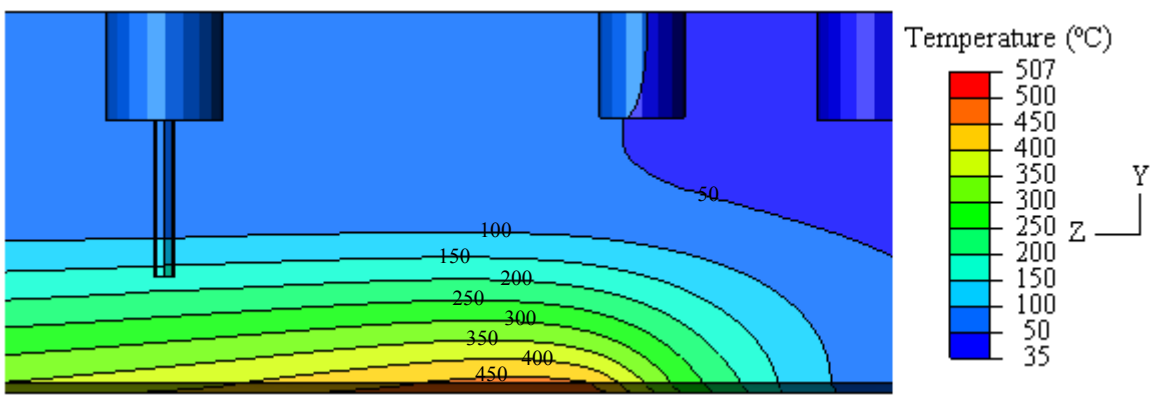

Figure 3.13. Temperature Contours around the Peak Heat Flux

Lowering the location of the peak heat flux by 80 mm to the level of the first thermocouple (such that localized three-dimensional effects are at a maximum at a thermocouple) and applying the offset method leaves an error of only -3.4 ºC at that thermocouple in CON1D [4]. Figure 3.12 also shows that the CON1D offset method is

independent of heat flux, since the same offset was applied to all thermocouples. This means that a given mold geometry needs to be modeled in three dimensions only once prior to conducting parametric studies using CON1D.

Table 3.1. Narrow Face Thermocouple Temperature Comparison

Distance Below Meniscus (mm)	3-D model	CON1D		CON1D with Offset	
	Temperature (ºC)	Temperature (ºC)	Difference (ºC)	Temperature (ºC)	Difference (ºC)
115	186.6	165.4	-21.2	187.5	0.9
249	148.9	133.6	-15.3	150.0	1.1
383	135.7	122.5	-13.2	136.7	1.0
517	126.3	114.7	-11.6	127.4	1.1
651	129.8	118.0	-11.8	131.1	1.3
785	137.6	124.9	-12.7	139.0	1.4
919	142.9	129.6	-13.2	144.3	1.4

3.4.2. Wide Face

In Table 3.2, ABAQUS and CON1D output results are compared along the mold perimeter in the calibration domain, 219 mm below the meniscus. The temperature at the cold face is tabulated at two points, and Figure 3.14 shows the temperature profile around the perimeter of a wide face water channel. As expected, point 1 is always hotter (around 90 °C) than point 2 (around 76 °C). CON1D predicts temperature of the water slot root (cold face) to be 81.4°C, which lies in between these two values. Water slot temperatures near the bolt hole are slightly hotter than those near the symmetry plane.

Table 3.2. Wide Face Temperature Comparison

Parameter	ABAQUS	CON1D
Hot face temperatures	237.2 - 243 ºC	237.4 ºC
Cold face temperatures in the cooling channels: Point 1- bottom of curved channel root Point 2- first straight points after the curve	Point 1- 89.44 – 91.43 ºC Point 2- 75.08 – 77.75 ºC	81.4 ºC
Temperature at the thermocouple location	143.9ºC	143.90 ºC (with offset)

Similar to the narrow face, a full three-dimensional model of one symmetric half of a wide face was constructed and boundary conditions applied according to the output from CON1D. Nearly all geometric details of the mold plate are included in this model to achieve as realistic results as possible. The mesh consisted of 4,223,072 tetrahedron elements and 855,235 nodes. The temperature contours of the hot face are shown in Figure 3.15.

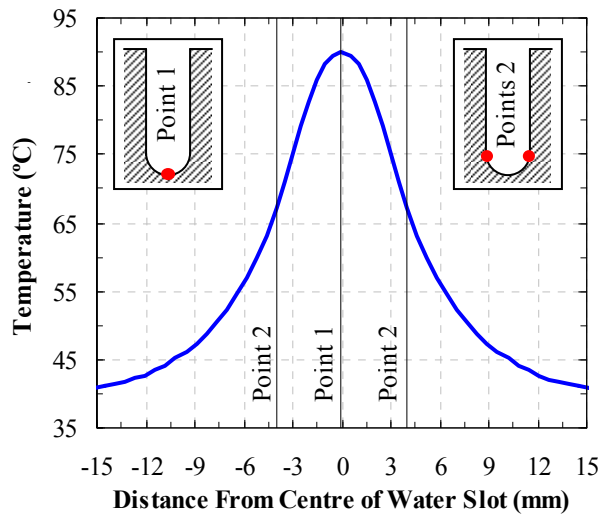

Figure 3.14. Temperature Profile around the Perimeter of a Wide Face Water Channel

The nonuniformity of the hot face temperatures in any horizontal plane is quite clear from Figure 3.15. These nonuniformities arise mainly from the columns of mold bolt holes, which are cooled by two round holes, which causes different cooling than in the adjacent slot-like water channels. Other researchers have observed the hot spots at the meniscus and corresponding temperature peaks running down the mold hotface opposite the bolt holes in both conventional slabs [17] and funnel molds [13]. O'Connor and Dantzig [11] isolated the glitches in the hot face temperature distribution observed along the funnel transition seams, in both Figures 3.15 and 3.16, which is a small effect. In addition, there is converging and diverging heat flow into the outer- and inner-curve surfaces of the funnel region, respectively, and nonuniform water channel depth below the hot face of the mold. The temperatures in several horizontal plane slices down the mold are shown in Figure 3.16. The inside flat and inside curve regions suffer from a local increase in temperature of about 25 ºC that persists from the meniscus until nearly mold exit. This coincides with a column of bolt holes, which has less cooling in most of the mold. This issue will be revisited in Chapter 5 in the context of cracks in the shell.

Towards the bottom of the mold, temperature generally increases, due to the curvature of the water slots, as seen in Figure 3.15. The exception to this observation is again due to the cylindrical cooling water channels bored vertically down the thicker copper regions containing the bolt holes, which still remove heat near the bottom of the mold, as observed in the temperature distribution presented in Figure 3.17. The cooling bores are fed and drained to the water box by smaller bores, also illustrated in the figure. While the high temperatures near mold

exit will certainly be detrimental to mold life, the shell is relatively thick at this location so is relatively insensitive to these changes in mold surface temperature.

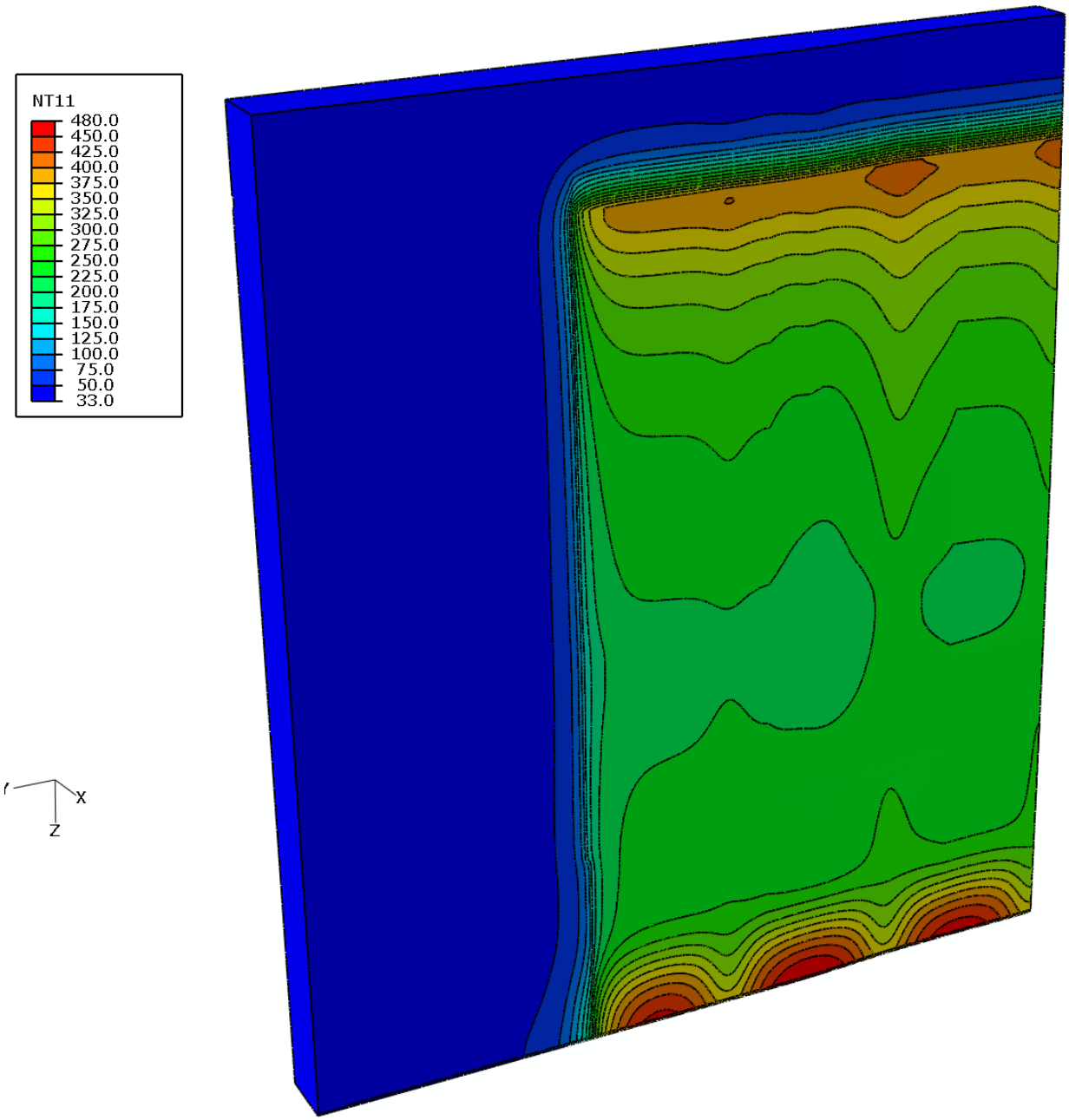

Figure 3.15. Wide Face Three-Dimensional Model Temperature Results

These results show that CON1D can produce temperature predictions with the accuracy of a three-dimensional model in both the wide and narrow faces for any heat flux profile. In addition to its increased speed and ease-of-use, the CON1D model includes powerful additional

calculations of the interfacial gap and solidifying shell. Thus, calibrating the CON1D model using the offset method to incorporate the three-dimensional ABAQUS results unleashes a powerful and accurate tool to study continuous casting phenomena.

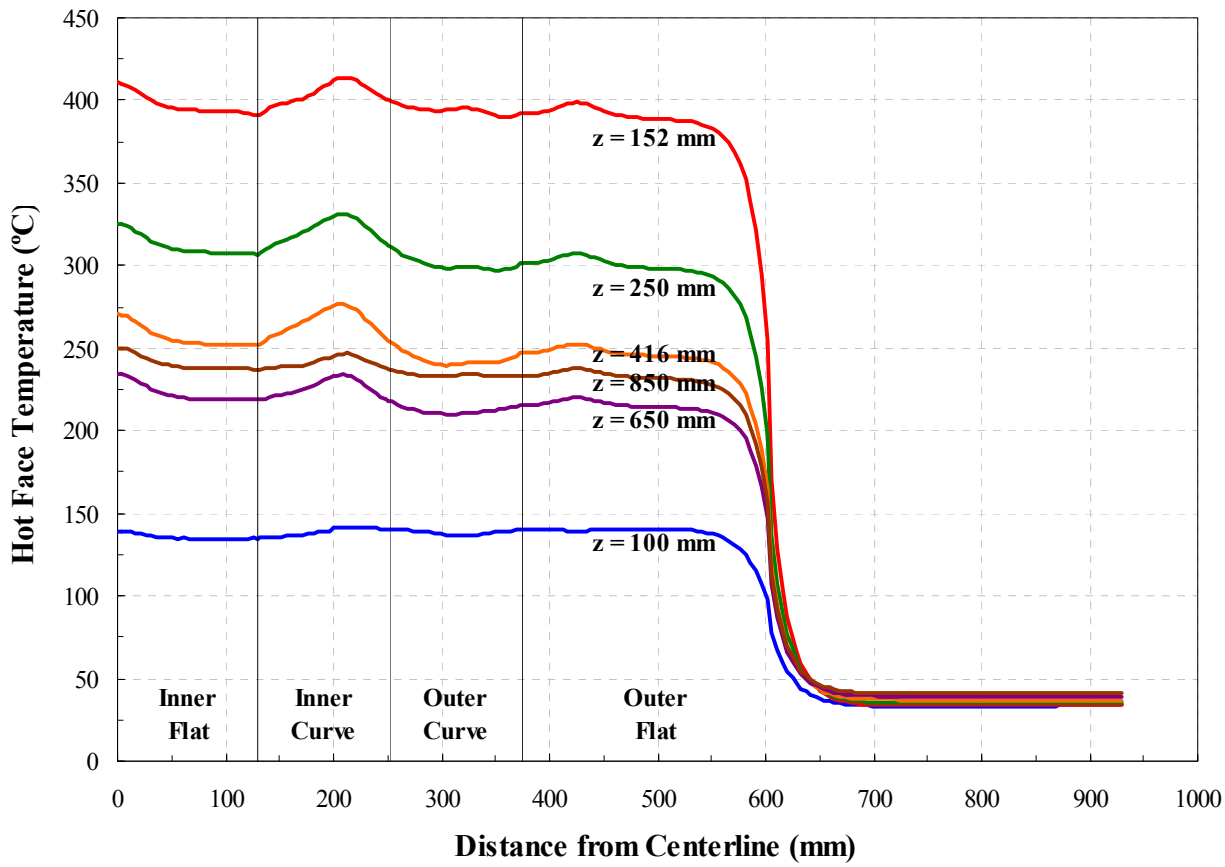

Figure 3.16. Wide Face Horizontal Plane Temperature Profiles

3.5. Validation with Plant Data and Typical Results

After verifying that the CON1D model matches with the full three-dimensional model, the next important step is to validate CON1D results with plant data and to check the accuracy of the model under different casting conditions.

3.5.1. Database Comparison

A large database of plant data was compared with CON1D simulation results. The database contains more than 700 average values of heat flux, thermocouple temperatures, and mold powder consumption (measured with a load cell), recorded from the wide faces during

stable casting periods. Stable casting periods are at least 30 minutes of operation when the most important casting parameters, including casting speed and width, are constant. These data were downloaded from the mold thermal monitoring (MTM) system of the level 2 control system.

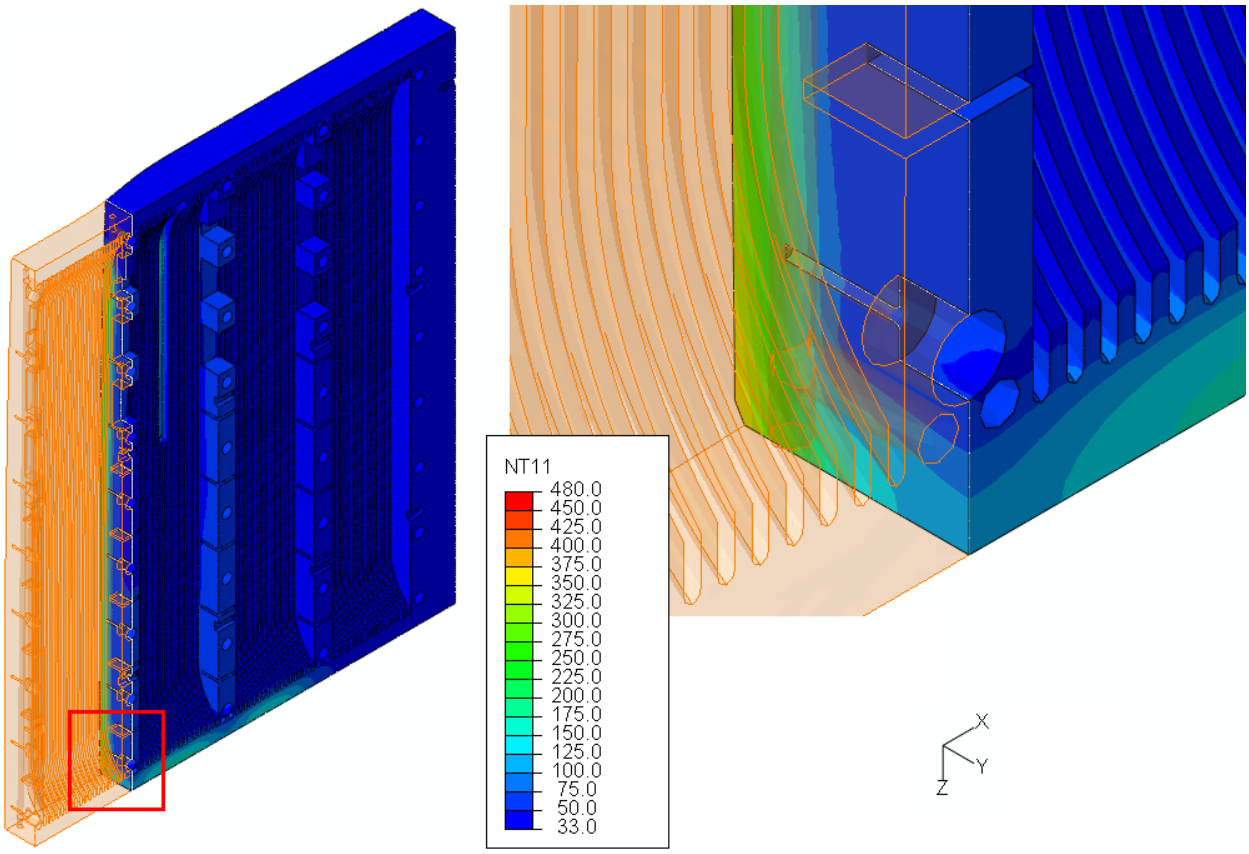

Figure 3.17. Effect of Cooling Bores at Mold Exit

The first comparison with plant data was done for the average mold heat flux (from the cooling water) for different casting speeds. The data were separated according to mold copper thickness into thick new plates (with 0 to 5 mm mold wear) and thin old plates (with 10 to 15 mm mold wear). The logarithmic curve-fit lines match very well with CON1D predictions, as shown in Figure 3.18. This match is partly due to the effect of a thinner shell decreasing the thermal resistance at higher casting speed and thinner mold lowering the mold resistance, which both increase heat flux. The realistic input data, given in Table 3.3, allow CON1D to capture these effects. The match was improved by incorporating changes in the solid slag layer velocity, as discussed later. In addition to investigating mold temperatures, shell growth and interfacial

phenomena, this calibrated and validated model enables extrapolation to predict behavior at higher casting speeds.

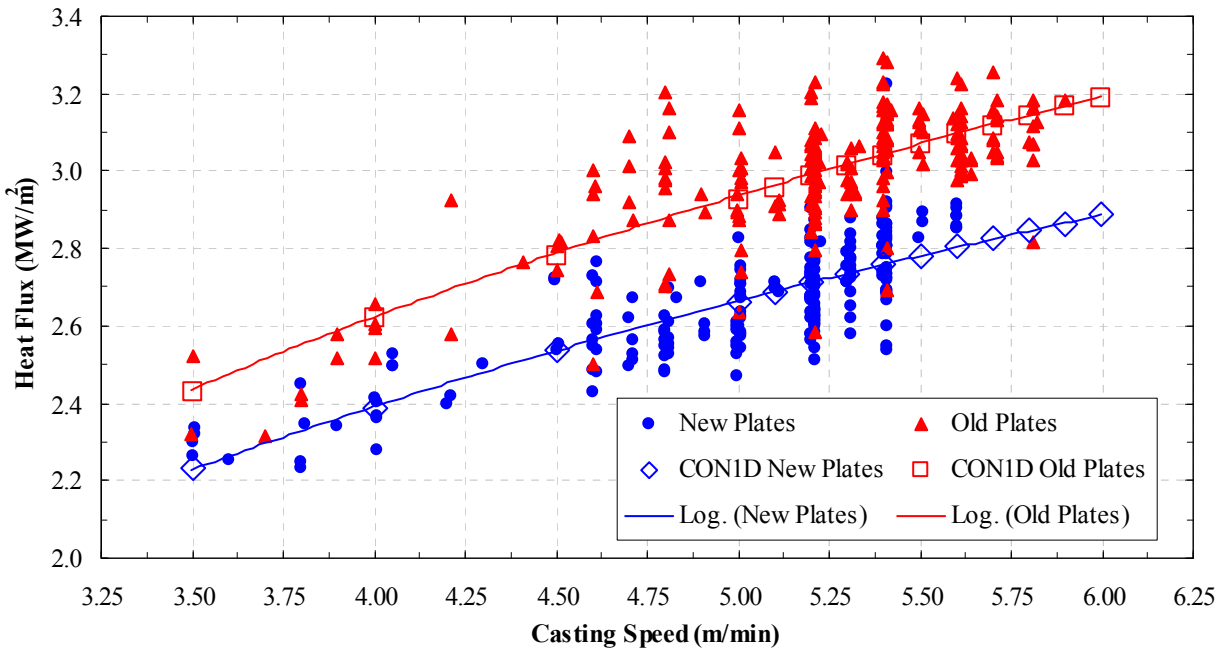

Figure 3.18. CON1D Mean Heat Flux Compared with Plant Data

Table 3.3. Simulation Conditions

Carbon Content, *C%*	0.045	%
Liquidus Temperature, T_{liq}	1531	°C
Solidus Temperature, T_{sol}	1509	°C
Steel Density, ρ_{steel}	7400	kg/m^2
Steel Emissivity, ε_{steel}	0.8	-
Initial Cooling Water Temperature, T_{water}	33	°C
Cooling Water Velocity, V_{water}	8.5	m/s
Mould Emissivity, ε_{mould}	0.5	-
Mould Slag Solidification Temp., T_{fsol}	1183	°C
Mould Slag Conductivity, k_{solid}, k_{liquid}	1.0, 1.5	W/(m·K)
Air Conductivity, k_{air}	0.06	W/(m·K)
Slag Layer/Mould Resistance, $r_{contact}$	9.5E-5	m^{2}K/W
Mould Powder Viscosity at 1300°C, μ_{1300}	0.9	Poise
Viscosity Temp.-dependence exponent, n	2.7	-
Slag Density, ρ_{slag}	2600	kg/m^3
Slag Absorption Factor, a	250	m^{-1}
Slag Refractive Index, m	1.667	-
Slag Emissivity, ε_{slag}	0.9	-
Pour Temperature, T_{pour}	1545	°C
Slab Geometry, width×thickness $W \times N$	1420×70	mm×mm
Nozzle Submergence Depth, d_{nozzle}	150	mm
Oscillation Mark Geometry, $d_{mark} \times w_{mark}$	0.08×1.5	mm×mm
Mould Oscillation Frequency, *freq*	325	cpm
Oscillation Stroke, *stroke*	6.0	mm

3.5.2. Velocity Ratio between Solid Slag Layer and Steel Shell

The solid slag layer is assumed to move down the mold at a time-averaged velocity that varies with distance down the mold according to the behavior of the liquid layer, interfacial friction, heat transfer, and other phenomena. This velocity, V_{flux}, ranges between zero (if the slag layer is attached to the mold) and the casting speed (if the slag layer is attached to the shell). The ratio between the solid slag speed and the casting speed must be input to the CON1D model. For a given powder consumption rate, this controls the time- and spatial-averages of the slag layer thickness, which greatly influences mold heat flux. This ratio is estimated from the following mass balance, assuming that liquid flux exiting the mold is negligible:

$$\frac{V_{flux}}{V_C} = \frac{Q_{MP}}{\rho_{slag} d_{slag}} \tag{3.2}$$

where V_{flux} is the velocity of the solid slag layer (m/min), V_C is the casting speed (m/min), Q_{MP} is the mold powder consumption rate (kg/m²), ρ_{slag} is the mass density of the mold slag (kg/m³), and d_{slag} is the slag layer thickness (m).

In practice, this velocity ratio varies with distance down the mold, which was characterized in this work to increase linearly between two values. At the meniscus, the ratio is zero, because the solid slag sticks to the mold wall and is relatively undisturbed due to the low friction associated with the liquid slag layer lubrication. At mold exit, Equation (3.2) is applied, based on the typical thickness of the solid slag layer that was measured at mold exit.

Slag film fragments previously taken from the mold exit of the Corus DSP caster ranged from 50 to 500 microns in thickness [5]. These thin plate-like fragments were found to be split into thinner mold-side and shell-side pieces, and the average thickness of 200 microns was used as a first approximation in calculating the velocity ratio with Equation (3.2). Further velocity ratios were found as a function of casting speed for both new and old mold plates, to match the average heat fluxes from the plant data. These two sets of ratios are plotted in Figure 3.19, and compared with mold powder consumption.

The velocity ratio has a strong correlation with the mold powder consumption, as given in Equation (3.2). This relation also can be seen in Figure 3.19, where both velocity-ratio curves drop with increasing casting speed in the same way as the mold powder consumption. This

finding is logical because a higher casting speed increases both hot face temperature and shell surface temperature in the mold. This encourages a hotter, thicker liquid slag layer that extends further down the mold, which encourages the solid slag layer to remain more attached to the mold wall, producing a lower velocity. Furthermore, the higher hot face temperature tends to keep the mold slag above its glass transition temperature, making slag fracture less likely and thus lower average velocity ratio at higher casting speed.

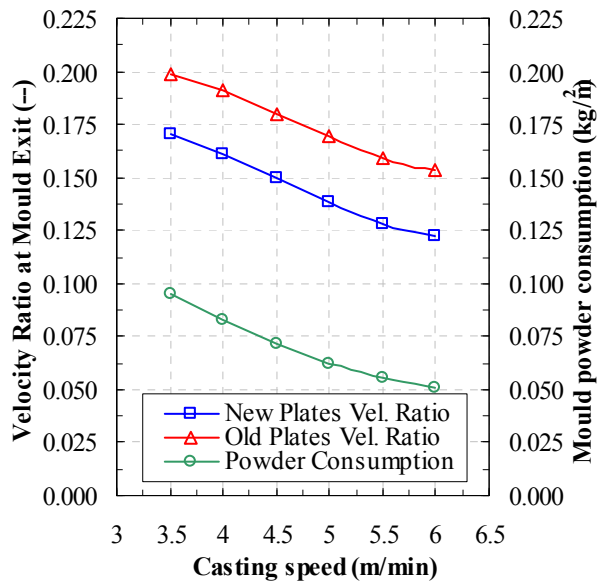

Figure 3.19. Effect of Casting Speed on Consumption and Velocity Ratios

Mold heat flux varies with casting speed, velocity ratio and mold plate thickness. The CON1D results indicate that the velocity ratio itself varies with plate thickness. As older plates become thinner with wear, the mold hot face temperature is reduced, which has a similar effect to decreasing casting speed. Thus, the velocity ratio is expected to increase with old plates, as shown in Figure 3.19. The actual speed of the moving solid slag layer is not easily measured. Thus, the application of calibrated and validated models such as CON1D is important to achieve the understanding of mold phenomena necessary to extrapolate plant data to new conditions and to solve product quality problems.

3.5.3. Temperature Validation

Plant data were obtained from a mold instrumented with forty thermocouples, as part of the standard MTM system to evaluate further the CON1D predictions. A period of 23 minutes of

stable casting at a speed of 5.2 m/min and a width of 1328 mm was chosen for this comparison, due to its stability in the thermocouples measurements. The meniscus level was measured to be about 100 mm below the top of the mold. Although the mold is capable of having a thermocouple in every bolt hole, the instrumented mold has only four rows of thermocouples. The first and fourth rows have 10 thermocouples, while the middle two rows have two thermocouples. The rows are 75, 200, 325, and 450 mm below the meniscus. Further details are provided elsewhere [14]. The 15 mm thermocouple depth below the hot face was offset by 2.41 mm to 12.59 mm for CON1D.

The predicted hot face temperature profile, cold face (water slot root) temperature profile and thermocouple temperatures from CON1D are shown in Figure 3.20. This figure also shows the average of the measured temperatures, which are slightly lower. This might be due to boiling in the water channels or minor contact problems, both of which result in a lower mold temperature. Scale formation in the water channels would cause the mold temperature to increase, providing another explanation for the variability in the measurements.

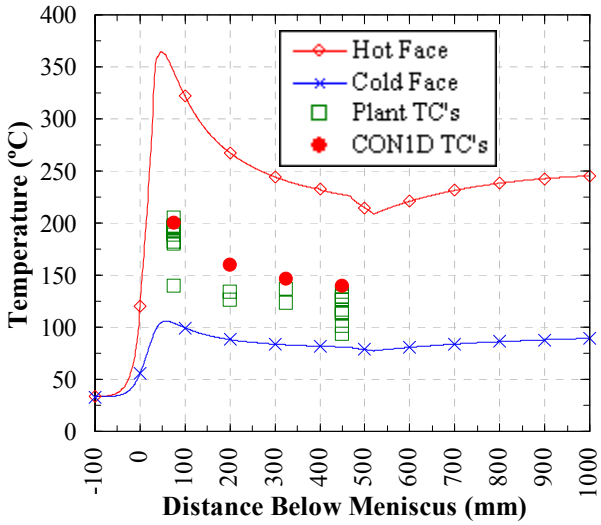

Figure 3.20. Predicted Thermocouple Temperatures Compared with Plant Data

3.5.4. Solidification Model Results

Having validated the CON1D model capability to predict heat flux and mold temperature distribution down the mold, this modeling tool was applied to predict solidification and temperature evolution of the steel shell, and the behavior of the mold flux layers in the interfacial

gap. Typical results are presented in Figures 3.21 and 3.22 for the conditions in Table 3.3, comparing the wide face of new and old molds at 5.5 m/min casting speed.

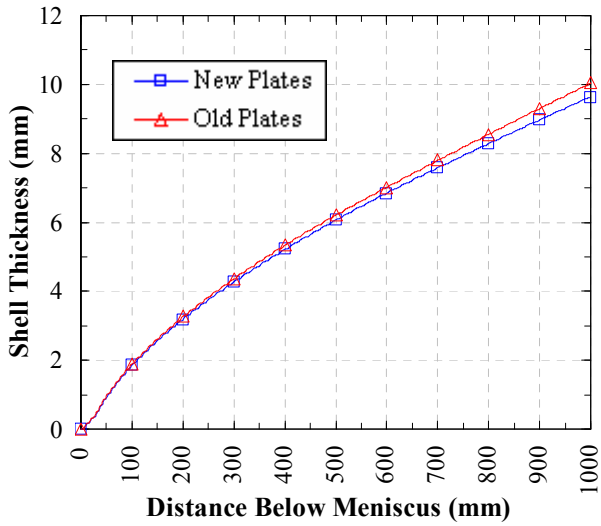

Figure 3.21. Shell Thickness Profiles

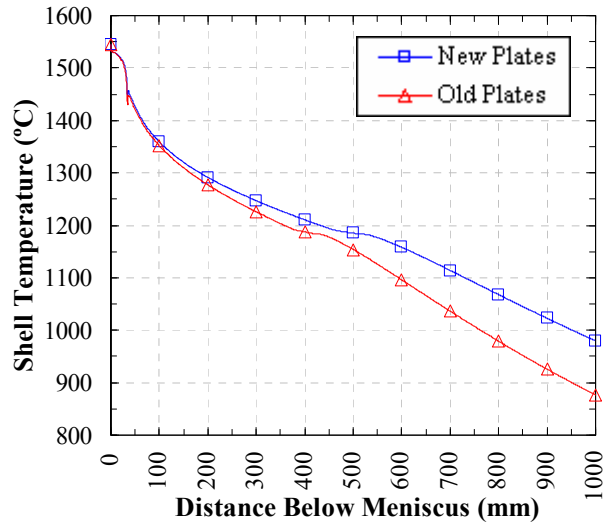

Figure 3.22. Shell Surface Temperature Profiles

Shell thickness increases down the mold at a decreasing rate, as the solid resistance increases. This contributes to lowering the heat flux across the interfacial gap. Shell thickness and heat flux are both lower for the new mold because the thicker mold provides additional thermal resistance, though he effect is very slight. The shell surface temperature also drops with distance down the mold, with variations that depend on the local heat flux. The lower surface temperature for old plates is due to the higher heat flux. The changes in slag layer thickness down the mold, which are governed by the changing velocity ratio, greatly affect all of these results. Further details on using the CON1D model under realistic conditions are given in [7].

3.6. Parametric Study

The verified, calibrated, and validated CON1D model is applied to investigate a range of mold thermal phenomena, including high-speed casting, mold powder properties, scale formation in the water channels and breakouts. The effect of mold plate thickness and casting speed on interfacial gap phenomena are investigated here. In each simulation, the velocity ratio and mold powder consumption were taken as functions of casting speed according to Figure 3.19.

The effects of casting speed and mold plate thickness on various parameters at mold exit are shown in Figures 3.23 to 3.26. Increasing casting speed naturally increases the mold hot face

temperature and decreases the shell thickness. This causes higher slab surface temperatures, although the increased heat flux with increasing casting speed tends to counter this trend. Slag layer thickness decreases with casting speed, owing to the smaller slag consumption rate, but the opposing effect of lower solid slag velocity ratio tends to lessen this trend. Decreasing the mold plate thickness (as the plates become older) decreases the hot face temperature as expected. This increases the solid slag layer velocity (Figure 3.19), which produces a thinner slag layer, as shown in Figure 3.26. Combined with the smaller resistance of the thinner mold plate, this increases the heat flux. This causes the shell thickness to increase slightly and slab surface temperature to decrease. These effects might be compensated by adding a thicker mold coating layer, or by carefully decreasing the water slot velocity as the molds age and become thinner.

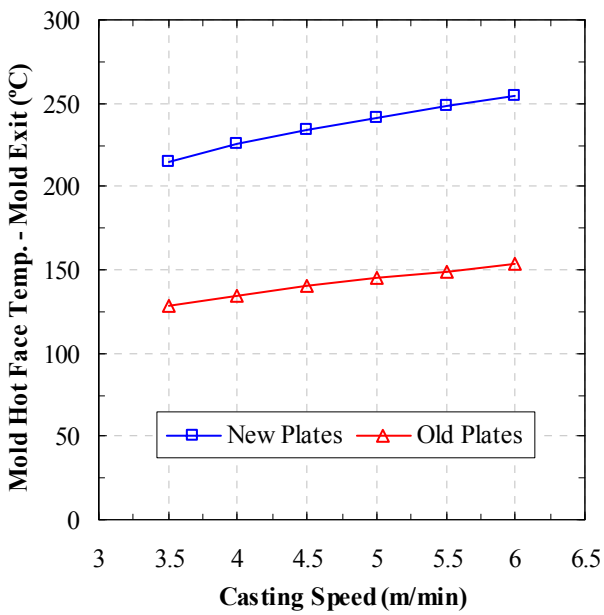

Figure 3.23. Effect of V_C on Hot Face Temperature

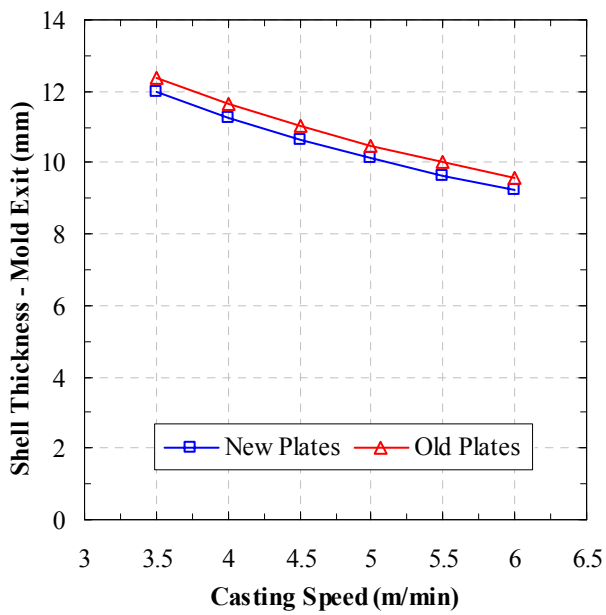

Figure 3.24. Effect of V_C on Shell Thickness

3.7. Conclusions

This work summarizes the development of an accurate computational tool for modeling heat transfer in the thin-slab continuous casting mold at the Corus DSP. Work towards this end includes model verification with a complete thermal three-dimensional analysis of the entire complex mold geometry, model calibration using the offset method to match thermocouple measurements and model validation with over 700 sets of plant data from an instrumented mold. The CON1D model is then applied together with plant measurements to gain new insights into

the effects of casting speed and mold plate thickness on mold heat transfer. The modeling study has revealed that increasing the casting speed causes a thinner solidified steel shell, higher heat flux, higher mold hot face temperature, a thinner slag layer and lower solid slag layer velocity. Also, increasing the mold plate thickness increases hot face temperature, lowers solid slag layer velocity, increases slag layer thickness, and lowers mold heat flux. The CON1D model is being applied to gain further insight into continuous casting of thin slabs, including the extrapolation of model predictions of heat transfer and interfacial phenomena to higher casting speed and the optimization of mold taper, mold distortion, and funnel design.

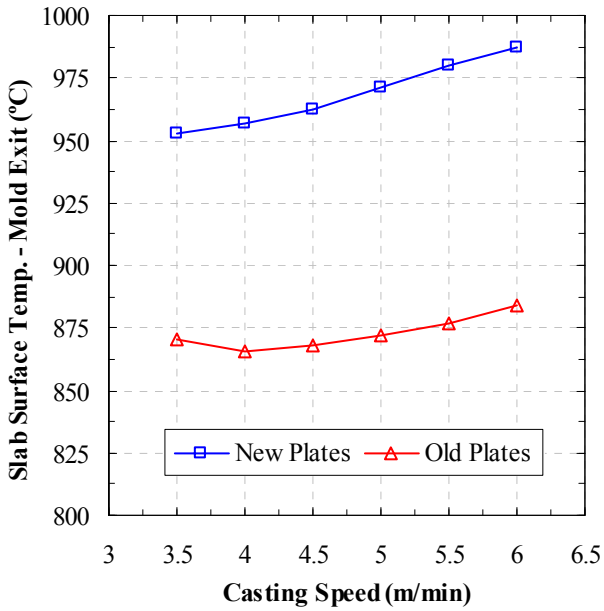

Figure 3.25. Effect of V_C on Slab Surface Temperature

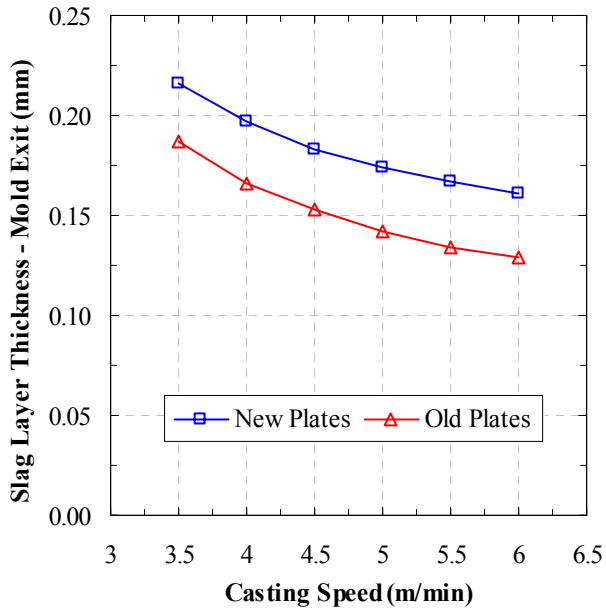

Figure 3.26. Effect of V_C on Slag Layer Thickness

3.8. References

1. *ABAQUS 6.6-1 User Manuals*. (2006), Dassault Simulia, Inc., 166 Valley Street, Providence, RI, USA 02909-2499.
2. C. Chow, I.V. Samarasekera, B.N.Walker, and G. Lockhart, "High Speed Continuous Casting of Steel Billets Part 2: Mould Heat Transfer and Mold Design." *Ironmaking and Steelmaking*, **29**:1 (2002), pg. 61-69.
3. L. Guo, X. Wang, H. Zhan, M. Yo, and D. Fang, "Mould Heat Transfer in the Continuous Casting of Round Billet." *ISIJ International*, **47**:8 (2007), pg. 1108-1116.
4. L.C. Hibbeler and B.G. Thomas, Continuous Casting Consortium Report 200701, (2007).
5. J.A. Kromhout, S. Melzer, E.W. Zinngrebe, A.A. Kamperman and R. Boom, "Mould Powder Requirements for High-Speed Casting." *Proceedings of the 2006 International Symposium*

on Thin Slab Casting and Rolling, The Chinese Society for Metals, Guangzhou, (2006), pg. 306-313.

6. M. M. Langeneckert, "Influence of Mold Geometry on Heat Transfer, Thermocouple and Mold Temperatures in the Continuous Casting of Steel Slabs." Masters Thesis, The University of Illinois at Urbana-Champaign, (2001).
7. Y. Meng and B.G. Thomas, "Heat-Transfer and Solidification Model of Continuous Slab Casting: CON1D." *Metallurgical and Materials Transactions*, **34B**:5 (2003), pg. 685-705.
8. Y. Meng and B.G. Thomas, "Modeling Transient Slag-Layer Phenomena in the Shell/Mold Gap in Continuous Casting of Steel." *Metallurgical and Materials Transactions*, **34B**:5 (2003), pg. 707-725.
9. Y. Meng and B.G. Thomas, "Simulation of Microstructure and Behavior of Interfacial Mold Slag Layers in Continuous Casting of Steel." *ISIJ International*, **46**:5 (2006), pg. 660-669.
10. H. Nam, H.-S. Park, and J.K. Yoon, "Numerical Analysis of Fluid Flow and Heat Transfer in the Funnel Type Mold of a Thin Slab Caster." *ISIJ International*, **40**:9 (2000), pg. 886-892.
11. T.G. O'Connor and J.A. Dantzig, "Modeling the Thin-Slab Continuous-Casting Mold." *Metallurgical and Materials Transactions*, **25B**:3 (1994), pg. 443-457.
12. J.K. Park, I.V. Samarasekera, B.G. Thomas, and U.S. Yoon, "Thermal and Mechanical Behavior of Copper Molds During Thin-Slab Casting (I): Plant Trial and Mathematical Modeling." *Metallurgical and Materials Transactions*, **33B**:3 (2002), pg. 425-436.
13. J.K. Park, I.V. Samarasekera, B.G. Thomas, and U.S. Yoon, "Thermal and Mechanical Behavior of Copper Molds During Thin-Slab Casting (II): Mold Crack Formation." *Metallurgical and Materials Transactions*, **33B**:3 (2002), pg. 437-449.
14. B. Santillana, B.G. Thomas, A. Hamoen, L.C. Hibbeler, A.A. Kamperman, W. van der Knoop, "Investigating Mould Heat Transfer in Thin Slab Casting with CON1D." *Iron and Steel Technology*, **5**:7 (2008), pg. 51-63.
15. B. Santillana, L.C. Hibbeler, B.G. Thomas, A. Hamoen, A. Kamperman, and W. van der Knoop, "Heat Transfer in Funnel-Mould Casting: Effect of Plate Thickness." *ISIJ International*, **48**:10 (2008), pg. 1380-1388.
16. J.W. Shaver, "Measurements of Molten Steel/Flux Interface Phenomena in Thin Slab Casting." Masters Thesis, The University of British Columbia, (2002).
17. B.G. Thomas, G. Li, A. Moitra, and D. Habing, "Analysis of Thermal and Mechanical Behavior of Copper Molds During Continuous Casting of Steel Slabs." *Iron and Steelmaker*, **25**:11 (1998), pg. 125-143.
18. Y. Xie, H. Yu, X. Ruan, B. Wang, and Y. Ma, "FE Numerical Simulation of Mould Temperature Field During the Continuous Casting of Steel." *International Journal of Advanced Manufacturing Technology*, **30**:7-8 (2006), pg. 645-651.
19. X.S. Zheng, M.H. Sha, and J.Z. Jin, "Experimental Research and Numerical Simulation of Mold Temperature Field in Continuous Casting of Steel." *Acta Metallurgica Sinica (English Letters)*, **19**:3 (2006), pg. 176-182.

CHAPTER 4

THERMAL BEHAVIOR OF THE SOLIDIFYING SHELL

4.1. Introduction

Heat transfer is the driving force for any solidification process, and continuous casting is no exception. The copper mold and water flow rate through it govern the heat extraction from the solidifying steel shell and thus the solidification characteristics of the steel. This chapter emphasizes the heat transfer characteristics of solidifying shells in funnel molds, independent of the mechanical response of the shell and interaction with the mold. The behavior of the shell is an inherently coupled thermo-mechanical phenomenon; this chapter analyzes the heat transfer in the shell with emphasis on the effects of the geometry of the funnel.

Previous work on thermal behavior of the solidifying shell is usually performed in the context of coupled thermo-mechanical phenomena (discussed in more detail in Chapter 5) or coupled heat-flow phenomena. Numerical models are employed in almost every investigation, employing both the finite-difference method and finite element methods, with both implicit and explicit time integration schemes (*cf.* reviews in [21,22,28,40]). Some of the earliest heat transfer models of the solidifying shell include that of Kung and Pollock [23], and Lait, Brimacombe and Weinberg [24]. More recently, the heat transfer and fluid flow around the shell were modeled in thin-slab casters both with a funnel [30] and without (parallel mold) [31]. The heat transfer in the shell was recently modeled in two dimensions [32], with numerous modeling issues, and three dimensions [22], as a proof-of-concept for stress modeling.

4.2. Governing Equations and Their Finite-Element Representation

The heat transfer in the shell is governed by the conservation of energy equation [10], which balances external work and heat transfer via the first law of thermodynamics:

$$\frac{DH}{Dt} = -\nabla \cdot \boldsymbol{q} + \boldsymbol{\sigma}' : \boldsymbol{D} + \rho \dot{R} \tag{4.1}$$

where H is the temperature-dependent total enthalpy, D/Dt is the "material derivative" with respect to time, $\boldsymbol{q}$ is the heat flux vector, $\boldsymbol{\sigma}'$ is the deviatoric stress tensor (*cf.* Chapter 5), $\boldsymbol{D}$ is the rate-of-deformation tensor, ρ is the mass density, and $\dot{R}$ is the internal heat generation per unit volume. For reasons to be discussed later, the mass density of the steel in this work is

assumed to be constant. The heat flux vector is related to temperature via the generalized Fourier's law, $\boldsymbol{q} = -\boldsymbol{K} \cdot \nabla T$, where $\boldsymbol{K}$ is the thermal conductivity tensor and T is temperature (use of Fourier's law is acceptable because the working temperatures are sufficiently higher than absolute zero, the temperature gradients are relatively small, and time periods of interest are sufficiently long). Neglecting internal heat generation and viscous dissipation effects, the conservation of energy equation is then:

$$\rho\left(\frac{Dh}{Dt}\right) = \nabla \cdot \left(\boldsymbol{K} \cdot \nabla T\right) \tag{4.2}$$

where h is the specific enthalpy. In the solid state, thermophysical properties exhibit very little dependence upon pressure, so applying the chain rule to the material derivative of enthalpy for temperature gives:

$$\rho\left(\frac{\partial h}{\partial T}\right)\left(\frac{DT}{Dt}\right) = \nabla \cdot \left(\boldsymbol{K} \cdot \nabla T\right) \tag{4.3}$$

Expanding the material derivative of temperature then yields the governing equation for the temperature field in the solidifying shell:

$$\rho\left(\frac{\partial h}{\partial T}\right)\left(\frac{\partial T}{\partial t} + v_x \frac{\partial T}{\partial x} + v_y \frac{\partial T}{\partial y} + v_z \frac{\partial T}{\partial z}\right) = \nabla \cdot \left(\boldsymbol{K} \cdot \nabla T\right) \tag{4.4}$$

where v_x, v_y, and v_z are the velocities of the material in the x-, y-, and z-directions.

Well-posed heat transfer boundary-value problems also require boundary conditions. A solid body can be described by its interior Ω, in which the energy balance Equation (4.4) must hold, and its boundary Γ, on which boundary conditions must be specified. Valid boundary conditions include specified temperatures $T = T_{sp}$ on part of the boundary Γ_T, specified heat flux $\boldsymbol{q} = \boldsymbol{q}_{sp}$ on part of the boundary Γ_q, or a combination of the two. Specified heat flux boundary conditions include direct specification of the heat flux $\boldsymbol{q}_{sp} = q_{sp}\boldsymbol{n}$, convection boundaries $\boldsymbol{q}_{sp} = \boldsymbol{q}_{conv} = h_c\left(T - T_\infty\right)\boldsymbol{n}$, or radiation boundaries $\boldsymbol{q}_{sp} = \boldsymbol{q}_{rad} = \varepsilon_e \sigma_{SB}\left(T^4 - T_\infty^4\right)\boldsymbol{n}$, where q_{sp} is the specified scalar heat flux, h_c is the convection coefficient, ε_e is the emissivity coefficient, σ_{SB} is the Stefan-Boltzmann constant, T_∞ is the far-field temperature, and $\boldsymbol{n}$ is the outward surface normal.

The solid and liquid regions which comprise solidification problems may be handled with an additional thermal boundary condition at the internal interface which connects them, which is known as the Stefan condition. The change of phase accompanies a release of heat at this interface, so along an initially unknown interior position in the domain (the solid-liquid interface), the local heat balance (considering only conduction and the phase change) includes the heat flux from the liquid, the heat flux from the solid, and the enthalpy of formation (latent heat of fusion), H_f:

$$\rho H_f \left(\boldsymbol{v}^* - \boldsymbol{v}\right) \cdot \boldsymbol{n}^* = \left(\boldsymbol{K}_\ell \cdot \nabla T_\ell\right) \cdot \boldsymbol{n}^* - \left(\boldsymbol{K}_s \cdot \nabla T_s\right) \cdot \boldsymbol{n}^* \tag{4.5}$$

where $\boldsymbol{v}^*$ is the velocity of the interface, $\boldsymbol{v}$ is the velocity of the bulk material, $\boldsymbol{n}^*$ is the normal vector pointing from the solid to the liquid, and Fourier heat conduction has been assumed.

The heat transfer in the solidifying shell is fairly complicated, so it is best to let a formal scaling analysis dictate how to simplify the governing equation. For the sake of the following argument, assume that the enthalpy consists of "sensible" and "latent" heats:

$$h = c_p T + H_f f_s \tag{4.6}$$

where c_p is the specific heat capacity assumed to be independent of temperature, and $f_s(T)$ is the mass fraction of the solid material in a given control volume. Furthermore, assume that the thermal conductivity tensor is constant with temperature and isotropic, $\boldsymbol{K} = k\boldsymbol{I}$. Define the following dimensionless variables:

$$x^* = x/w_s \tag{4.7}$$

$$y^* = y/\delta \tag{4.8}$$

$$z^* = z/\ell_m \tag{4.9}$$

$$T^* = \left(T - T_{\min}\right)/\left(T_{\max} - T_{\min}\right) \tag{4.10}$$

$$t^* = t/t_d \tag{4.11}$$

where a superscript asterisk denotes the quantity is dimensionless, w_s is the slab width, δ is the average shell thickness at mold exit, ℓ_m is the mold length, $T_{\max}$ and $T_{\min}$ are the maximum and minimum shell temperatures in the mold, and $t_d = \ell_m / V_C$ is the dwell time of the shell inside the mold with casting speed V_C. The scaled governing equation is, with $v_x = v_y = 0$ and $v_z = V_C$:

$$\rho\left(c_p+\frac{H_f}{\left(T_{\max}-T_{\min}\right)}\frac{\partial f_s}{\partial T^*}\right)\left(\frac{\left(T_{\max}-T_{\min}\right)}{\ell_m/V_C}\frac{\partial T^*}{\partial t^*}+V_C\frac{\left(T_{\max}-T_{\min}\right)}{\ell_m}\frac{\partial T^*}{\partial z^*}\right)$$
$$=k\frac{\left(T_{\max}-T_{\min}\right)}{w_s^2}\frac{\partial T^{*2}}{\partial x^{*2}}+k\frac{\left(T_{\max}-T_{\min}\right)}{\delta^2}\frac{\partial T^{*2}}{\partial y^{*2}}+k\frac{\left(T_{\max}-T_{\min}\right)}{\ell_m^2}\frac{\partial T^{*2}}{\partial z^{*2}} \tag{4.12}$$

Dividing through by the coefficient of the last term gives a dimensionless form of the governing equation:

$$\frac{\ell_m V_C}{k/\rho c_p}\left(1+\frac{H_f}{c_p\left(T_{\max}-T_{\min}\right)}\frac{\partial f_s}{\partial T^*}\right)\left(\frac{\partial T^*}{\partial t^*}+\frac{\partial T^*}{\partial z^*}\right)=\frac{\ell_m^2}{w_s^2}\frac{\partial T^{*2}}{\partial x^{*2}}+\frac{\ell_m^2}{\delta^2}\frac{\partial T^{*2}}{\partial y^{*2}}+\frac{\partial T^{*2}}{\partial z^{*2}} \tag{4.13}$$

Identifying the thermal diffusivity of the steel as $\alpha_T=k/\rho c_p$ reveals some classic dimensionless numbers. The Péclet number, $\mathrm{Pe}=V_C\ell_m/\alpha_T$, is the ratio of heat advection to heat diffusion, and the Stefan number, $\mathrm{Ste}=c_p\left(T_{\max}-T_{\min}\right)/H_f$, is the ratio of sensible heat to latent heat. These terms substituted into the dimensionless governing equation gives:

$$\mathrm{Pe}\left(1+\frac{1}{\mathrm{Ste}}\frac{\partial f_s}{\partial T^*}\right)\left(\frac{\partial T^*}{\partial t^*}+\frac{\partial T^*}{\partial z^*}\right)=\frac{\ell_m^2}{w_s^2}\frac{\partial T^{*2}}{\partial x^{*2}}+\frac{\ell_m^2}{\delta^2}\frac{\partial T^{*2}}{\partial y^{*2}}+\frac{\partial T^{*2}}{\partial z^{*2}} \tag{4.14}$$

Relative to a stationary observer, the continuous casting process operates at a steady state, so the transient term $\partial T^*/\partial t^*$ is zero. Using typical values for continuous casting of steel, including a casting speed of V_C = 5 m/min, mold length of ℓ_m = 1 m, thermal conductivity of k = 33 W/(m·K), mass density of ρ = 7500 kg/m³, specific heat capacity of c_p = 661 J/(kg·K), enthalpy of formation of H_f = 272 kJ/kg, and a characteristic temperature drop of $T_{\max}-T_{\min}$ = 500 ºC, the Péclet number is Pe = $8.26\cdot10^5$ and the Stefan number is Ste = 1.22. Clearly, the advection dominates the heat transfer in the casting direction. With δ = 10 mm and w_s = 1.6 m, the aspect ratio terms are ℓ_m^2/w_s^2 = 0.444 and ℓ_m^2/δ = 10^5, which shows that the heat transfer through the thickness of the shell is the most important conduction term.

With negligible heat conduction in the casting direction, a Lagrangian domain may be used to analyze the heat transfer in the solidifying shell. This approximation follows a two-dimensional slice, perpendicular to the casting direction, of the solidifying strand as it moves down the mold at the casting speed. This approximation essentially transforms the physical z-direction into a temporal quantity, which is valid so long as the overall process remains at steady

state with respect to a stationary observer. The relation between time and the z-direction, relative to the top of the mold, is given by:

$$z = V_C t + z_m \tag{4.15}$$

where z_m is the average depth of the liquid pool below the top of the mold. This relation is only valid for constant casting speeds; the generalization requires integrating the "casting acceleration" over the relevant period of time. Continuous casting molds are oscillated at Hertzian frequency f_{osc} with peak-to-peak stroke of S_{osc} to avoid the shell from sticking to the hot faces of the mold; this effect can be included with a simple adjustment to the above space-time transformation with:

$$z = V_C t + z_m + \frac{S_{osc}}{2}\sin\left(2\pi f_{osc} t\right) \tag{4.16}$$

for sinusoidal oscillation patterns. Non-sinusoidal patterns are sometimes used in commercial practice, and the above equation can be changed accordingly for those cases. In practice, the oscillation frequency and stroke are functions of casting speed, both often increasing with increasing casting speed. The governing equation for the two-dimensional slice of the solidifying shell is then:

$$\rho \frac{\partial h}{\partial T}\frac{\partial T}{\partial t} = \nabla \cdot \left(\boldsymbol{K} \cdot \nabla T\right) \tag{4.17}$$

where the gradient operators consider only the x- and y-directions.

The governing equation for the temperature field, Equation (4.16), is a transient partial differential equation. While analytical or "exact" methods do exist for solving such an equation, the many nonlinearities presented by the physics of the problem, as well as the nontrivial solution domain, make such an analytical solution extraordinarily difficult at best, and hence a numerical method is employed in this work to discretize and solve the governing equation. The finite element method [7,41] is one such numerical method, and is particularly suited for the problem at hand because of its ability to treat complicated domain shapes. The finite element method has several manifestations, including a specific case of the method of weighed residuals known as the (Bubnov-) Galerkin method, stated as:

$$\int_\Omega \left[N\right]^T \left\{R\right\} d\Omega = 0 \tag{4.18}$$

where $[N]$ is the matrix of basis functions for a finite element, $\{R\}$ is the residual vector of the governing equation, and V is the volume of the domain. This statement forces the residual of the governing equation to zero in some average sense, and is enforced over each small finite element in which the domain has been sub-divided. The formulation of the finite element method used here uses the nodal temperatures $\{T\}$ as solution variables, and so within an element the temperatures are interpolated according to:

$$T = [N]\{T\} \tag{4.19}$$

For the equation that governs the temperature field, this gives:

$$\int_{\Omega} [N]^T \left\{ \rho \frac{\partial h}{\partial T} \frac{\partial T}{\partial t} - \nabla \cdot (\boldsymbol{K} \cdot \nabla T) \right\} d\Omega = 0 \tag{4.20}$$

Integrating by parts gives the finite element statement of the governing equation:

$$\int_{\Omega} [N]^T \rho \frac{\partial h}{\partial T} [N] d\Omega \{\dot{T}\} + \int_{\Omega} [B]^T [K][B] d\Omega \{T\} = \{F\} \tag{4.21}$$

where $[B]$ is the matrix of derivatives of element basis functions, $\{\dot{T}\}$ are the nodal cooling rates, and the boundary conditions are lumped together in the thermal force vector $\{F\}$. The boundary conditions are calculated according to:

$$\{F_q\} = -\int_{\Gamma_q} [N]^T q_{sp} d\Gamma_q \tag{4.22}$$

$$\{F_h\} = \int_{\Gamma_h} [N]^T h_c T_\infty d\Gamma_h \tag{4.23}$$

$$\{k_h\} = \int_{\Gamma_h} [N]^T h_c [N] d\Gamma_h \{T\} \tag{4.24}$$

$$\{F_r\} = \int_{\Gamma_r} [N]^T \varepsilon_e \sigma_{SB} \left(T^2 + T_\infty^2\right)(T + T_\infty) T_\infty d\Gamma_r \tag{4.25}$$

$$\{k_r\} = \int_{\Gamma_r} [N]^T \varepsilon_e \sigma_{SB} \left(T^2 + T_\infty^2\right)(T + T_\infty) [N] d\Gamma_r \{T\} \tag{4.26}$$

where the radiation condition has been factored to resemble a convection boundary condition. Note that the convection and radiation boundary conditions contribute to the thermal stiffness matrix of the system, in addition to the force vector on the right-hand-side. The time integration of Equation (4.21) is treated with the fully implicit "Backward Euler" method:

$$\{\dot{T}^{t+\Delta t}\} = \frac{1}{\Delta t}\left(\{T^{t+\Delta t}\} - \{T^t\}\right) \tag{4.27}$$

where a given timestep has size Δt. The governing equation is now:

$$\int_\Omega [N]^T \rho \frac{\partial h}{\partial T}^{t+\Delta t} [N] d\Omega \frac{1}{\Delta t}\left(\left\{T^{t+\Delta t}\right\}-\left\{T^t\right\}\right)+\int_\Omega [B]^T \left[K^{t+\Delta t}\right][B] d\Omega \left\{T^{t+\Delta t}\right\}=\left\{F^{t+\Delta t}\right\} \quad (4.28)$$

Since enthalpy, thermal conductivity, and the boundary conditions are dependent upon temperature, this equation is nonlinear. In this work, the Newton-Raphson method is employed to solve the system of nonlinear equations:

$$\begin{aligned}&\left(\int_\Omega [N]^T \rho \frac{\partial h}{\partial T_i}^{t+\Delta t} [N] d\Omega \frac{1}{\Delta t}+\int_\Omega [B]^T \left[K_i^{t+\Delta t}\right][B] d\Omega\right)\left\{\delta T_i\right\}= \\ &-\int_\Omega [N]^T \rho \frac{\partial h}{\partial T_i}^{t+\Delta t} [N] d\Omega \frac{\left(\left\{T_i^{t+\Delta t}\right\}-\left\{T^t\right\}\right)}{\Delta t}-\int_\Omega [B]^T \left[K_i^{t+\Delta t}\right][B] d\Omega \left\{T_i^{t+\Delta t}\right\}-\left\{F_i^{t+\Delta t}\right\}\end{aligned} \quad (4.29)$$

The tangent operator is calculated analytically, though not all contributions are calculated, so the Newton-Raphson method is best classified as a hybrid method. At each iteration i, this matrix equation is solved for the temperature correction $\left\{\delta T\right\}_i$, and a new guess of the nodal temperature field is calculated simply with:

$$\left\{T_{i+1}^{t+\Delta t}\right\}=\left\{T_i^{t+\Delta t}\right\}+\left\{\delta T_i\right\} \quad (4.30)$$

The criteria for convergence are based on the maximum temperature correction and the maximum residual at any node.

Given that the change in enthalpy during the liquid-solid phase change is so severe, the quantity $\partial h/\partial T$ at a given integration point is recalculated using a spatial-temporal averaging procedure to help the global iterative solution procedure converge better while maintaining a global heat balance [1]. Bonacina *et al.* [2] used a three-level implicit scheme that treats latent heat effects as enhanced specific heat capacity at an intermediate time step. Comini *et al.* [6] improved upon this by using spatial gradients of enthalpy and temperature to better approximate the effective specific heat capacity. Lemmon [27] used a slightly different version which better estimates the average enthalpy of the element. Chidiac *et al.* [5] later proposed a spatial-averaging technique for finite elements that uses the nodal temperatures and fraction solids to enhance the accuracy of the $\partial h/\partial T$ prediction in both space and time. Thomas *et al.* [34] compared many of the methods used for solidification heat transfer with finite element method and recommended that of Lemmon. Voller *et al.* [37] expanded upon this comparison, and concluded that the appropriate method for treating the latent heat effects depends upon the

needed level of robustness, including geometric complexity, non-constant properties, ability to couple with other effects, and computational effort and accuracy.

4.3. Thermal Material Properties

The conservation of energy equation (continuum or finite-element) requires the specification of thermophysical properties, including the specific enthalpy, thermal conductivity, and implicitly, the phase fractions. These properties in real materials exhibit a dependence upon temperature, which must be known accurately for realistic simulations.

4.3.1. Phase Fractions

Steels experience both liquid-to-solid and solid state phase transitions over a range of temperatures owing to their complex alloy compositions and competing thermal and solutal effects. The change of phase from liquid to solid occurs over a specified temperature range often called the mushy zone, beginning at the liquidus temperature T_{liq}, where solid first starts to form, and completing at the solidus temperature T_{sol}, where the last liquid freezes. A release of heat accompanies the phase change, which is quantified in the enthalpy of formation, also called the latent heat of fusion, H_f, which will be discussed in the next section. These physics are built into a phase diagram, which can then be used to calculate the mass fractions of the individual phases within a given control volume. Pure iron has three distinct solid phases, including the high-temperature body-centered cubic delta ferrite, the intermediate temperature face-centered cubic austenite, and the low-temperature body-centered cubic alpha ferrite. A mixture of iron and carbon, the basis for steel, exhibits these phases as well as several other low-temperature phases (*e.g.*, pearlite, bainite, *etc.*), which are not treated in this work since the temperatures of the solidifying steel shell do not become low enough within the mold itself. The liquid and solid phases exhibit different thermal and mechanical behaviors, and the phase fractions are needed to accurately capture both the phase transformations and the differing behaviors.

Two different models are used in this work to calculate the phase fractions. The low-temperature phase fractions are calculated using the lever rule and a linearized Fe-Fe_3C phase diagram. The linearized phase diagram is defined by 15 points, as shown in Figure 4.1, which are functions of the compositions of elements present in the alloy [19]. The high-temperature

phase fractions are calculated using the microsegregation model of Won and Thomas [38], which is also a function of the alloy composition, and calculates the liquidus and solidus temperatures based on the fact that the segregation around the secondary dendrite arms significantly suppresses the solidus temperature. The composition of the steel grade used in this work is given in Table 4.1. Regardless of the model used, the mass fractions of the liquid, delta-ferrite, austenite, and alpha-ferrite phases, f_ℓ, f_δ, f_γ, and f_α, respectively, can be calculated as a function of temperature, as shown in Figure 4.2. The liquidus temperature is calculated as 1528.2 ºC and the solidus temperature is calculated as 1508.1 ºC.

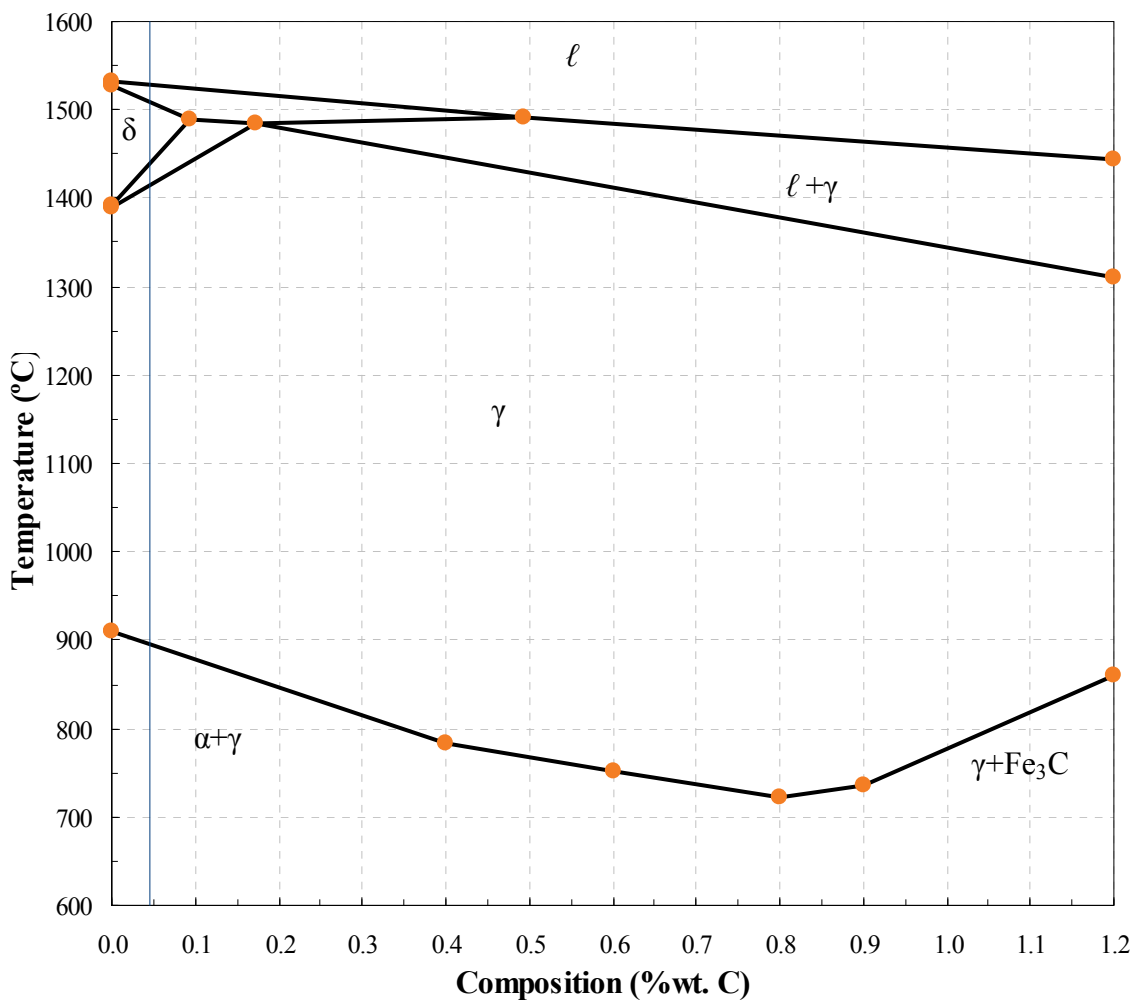

Figure 4.1. Linearized Fe-Fe_3C Phase Diagram

Table 4.1. Composition of Steel Used in This Work, in % wt.

C	Cr	Cu	Fe	Mn	Mo	N	Ni	P	S	Si	Ti	V
0.045	0.015	0.012	99.66	0.210	0.002	0.003	0.020	0.008	0.006	0.011	0.003	0.002

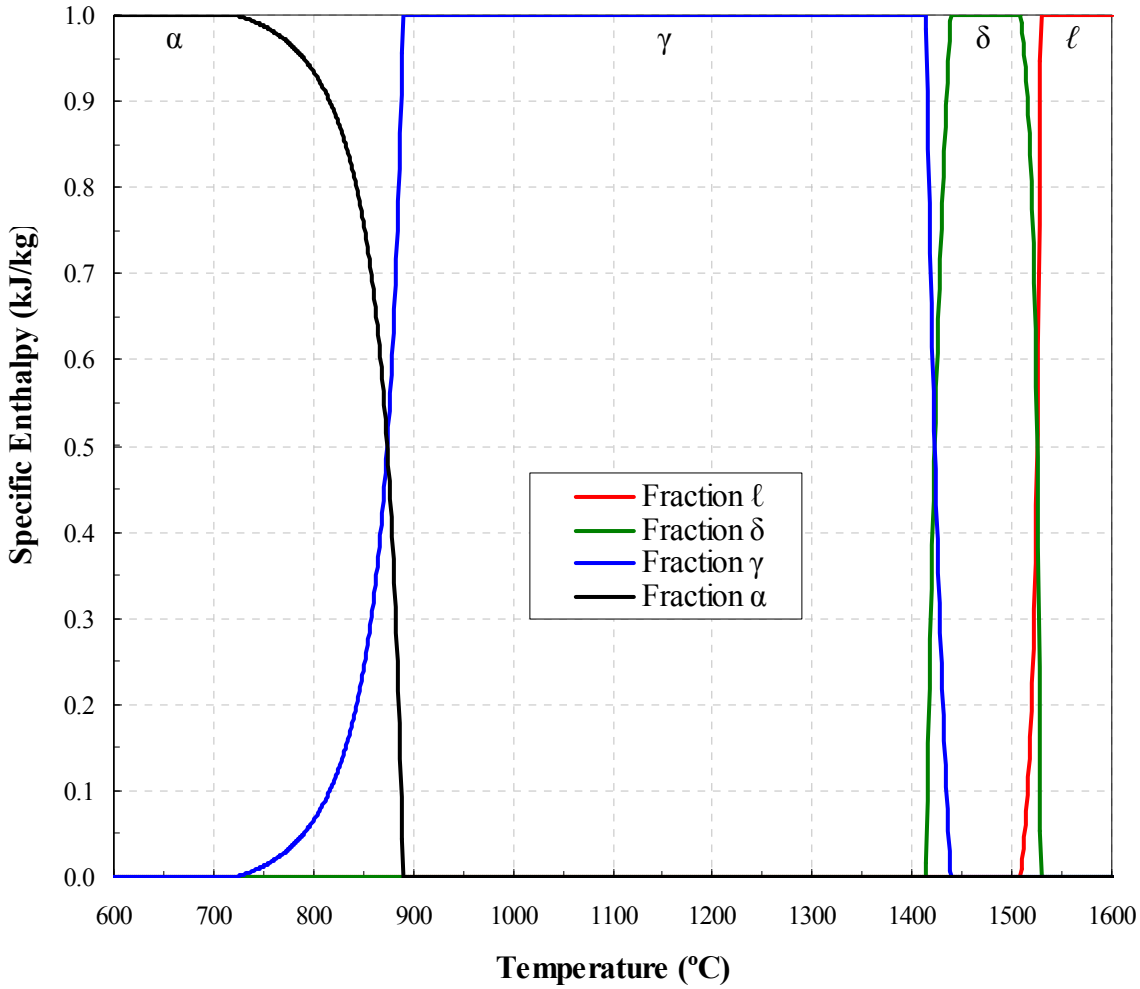

Figure 4.2. Phase Fractions of 0.045 %wt. C Steel

4.3.2. Enthalpy

Enthalpy is an auxiliary thermodynamic function consisting of internal energy and the work done by pressure during volume changes, or, mathematically:

$$H = U + pV \tag{4.31}$$

where H is the total enthalpy, U is the total internal energy, p is pressure, and V is volume. Or, more conveniently, on a per-unit-mass basis:

$$h = u + p/\rho \tag{4.32}$$

where h is the specific enthalpy, u is the specific internal energy, and ρ is the mass density. Enthalpy is convenient to use because it equals the heat input to a system at constant pressure,

which is an appropriate assumption to make in the context of materials processing at atmospheric pressure, such as the continuous casting process.

When several phases are present in a given control volume, the mixture enthalpy may be derived by assuming that the total energy content of the control volume is the sum of its parts:

$$H_{mix} = H_\ell + H_\delta + H_\gamma + H_\alpha \tag{4.33}$$

where H_{mix} is the mixture total enthalpy and H_ℓ, H_δ, H_γ, and H_α are the total enthalpies of the liquid, delta-ferrite, austenite, and alpha-ferrite phases, respectively. Or, more conveniently, on a per-unit-mass basis:

$$h_{mix} = f_\ell h_\ell + f_\delta h_\delta + f_\gamma h_\gamma + f_\alpha h_\alpha \tag{4.34}$$

where h_{mix} is the mixture specific enthalpy and h_ℓ, h_δ, h_γ, and h_α are the specific enthalpies of the liquid, delta-ferrite, austenite, and alpha-ferrite phases, respectively. Harste [13] compiled measurements from several sources of the enthalpies of plain-carbon steels over a variety of temperatures and compositions and fit an equation to the measurements:

$$h_\ell = -104642.3 + 824.6157T + \Delta H_f^\ell \tag{4.35}$$

$$h_\delta = 50882.26 + 441.3942T + 88.72118 \cdot 10^{-3} T^2 \tag{4.36}$$

$$h_\gamma = 93453.72 + 429.8495T + 74.8901 \cdot 10^{-3} T^2 + \Delta H_f^\gamma \tag{4.37}$$

$$h_\alpha = \begin{cases} 12.82244 \cdot 10^6 - 5.217657 \cdot 10^9 T^{-1} - 10068.2T + 2.9934T^2 & 1184 \geq T \geq 1060 \\ -18.379674 \cdot 10^6 + 34871.21T - 16.0133T^2 & 1060 \geq T \geq 1042 \\ 5780384.0 - 11501.07T + 6.238181T^2 & 1042 \geq T \geq 1000 \\ 4055624.6 - 1.109483 \cdot 10^9 T^{-1} - 4720.324T + 2.29168T^2 & 1000 \geq T \geq 800 \\ -85.8 \cdot 10^3 + 5.19 \cdot 10^6 T^{-1} + 505T - (65.6 - 0.15 \cdot T) \cdot 10^{-3} T^2 & 800 \geq T \geq 298 \end{cases} \tag{4.38}$$

where temperatures are given in K and specific enthalpies are given in J/kg. The enthalpy of mixing was observed to have a dependence upon the composition of the steel, giving:

$$\Delta H_f^\ell = 18125C + 1.96612 \cdot 10^6 \frac{C^2}{43.839C + 1201.1} \tag{4.39}$$

$$\Delta H_f^\gamma = 36601C + 1.90793 \cdot 10^6 \frac{C^2}{43.839C + 1201.1} \tag{4.40}$$

where carbon compositions are given in %wt. C. A plot of the mixture specific enthalpy against temperature is given in Figure 4.3 for the 0.045 %wt. C steel considered in this work.

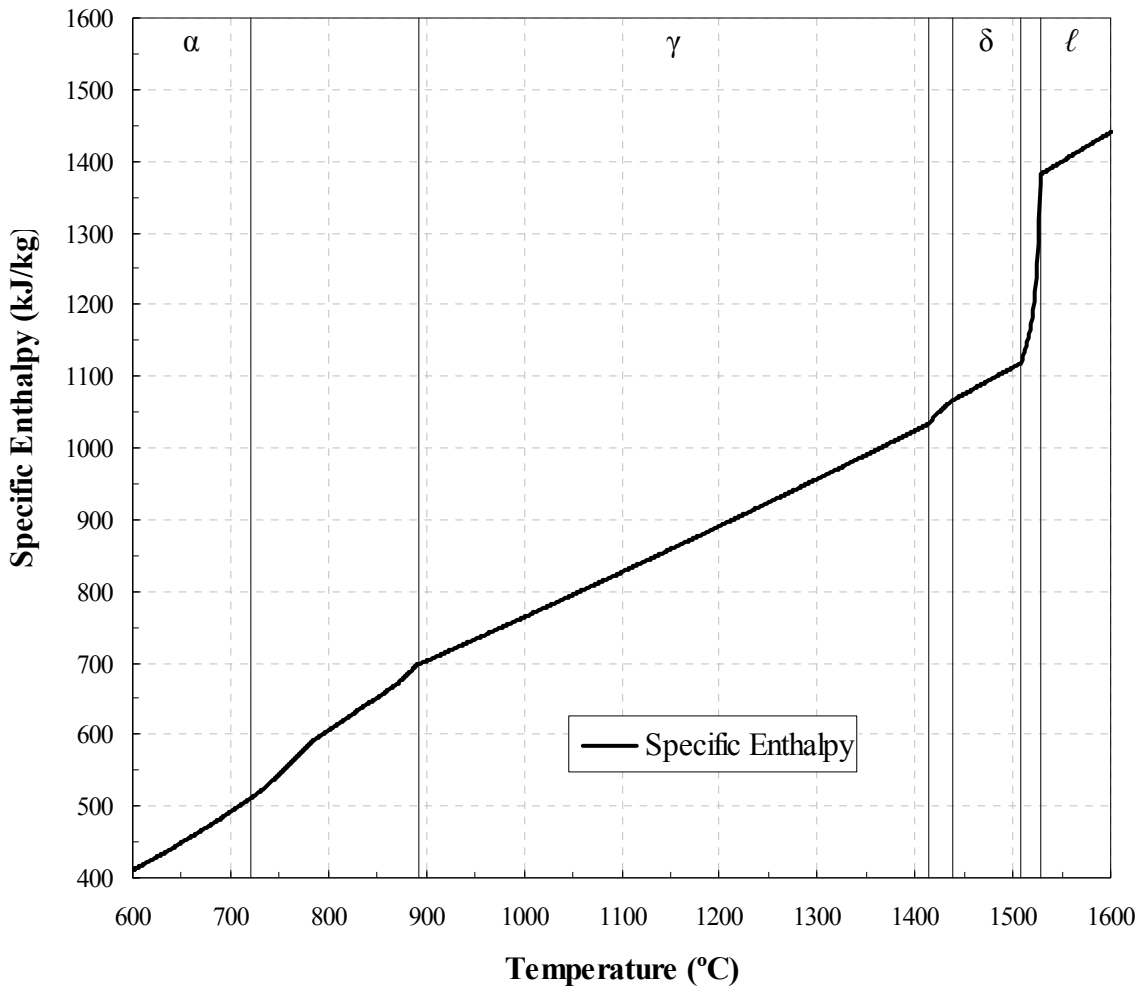

Figure 4.3. Specific Enthalpy of 0.045 %wt. C Steel

4.3.3. Thermal Conductivity

Fourier's law of heat conduction requires the definition of a constant of proportionality between the heat flux and the temperature gradient, called thermal conductivity. Thermal conductivity is a measure of the ability of a material to transfer energy without moving the material itself. Metals are typically very good conductors because of the ability of electrons to move freely through the lattice crystal structure. Interpreting temperature as a measure of molecular energy, thermal conductivity can exhibit a dependence upon temperature because as temperature increases, molecules both vibrate more intensely and move faster, carrying more energy and thus more heat throughout the lattice.

Individual crystals of metals have different conductivities along different directions because of different stacking patterns. Polycrystalline solids generally do not exhibit this effect because the constituent crystals of the bulk material are often not all identically aligned. In the case of continuously-cast steel, the subsurface material solidifies with parallel columnar dendrites, so some orientation effects might be present in this region. This issue is left for future work; for the present work, the thermal conductivity is treated as isotropic, although its value is assumed to depend upon temperature and composition C:

$$\boldsymbol{K}(T,C) = k(T,C)\boldsymbol{I} \tag{4.41}$$

Another source of anisotropy of thermal conductivity is phase-change regions. The thermal conductivities of the solid state phases of iron are not significantly different, as shown below, to warrant special treatment, but the liquid-to-solid phase change is affected by the anisotropic nature of the thermal conductivity; heat flows differently in the direction of dendrite growth than it does perpendicular to the growth direction, which consists of layers of liquid and solid material. The "resistor" model of heat conduction [17] applied to layers of two materials identifies the effective thermal conductivity in the directions parallel $k_{\parallel}$ and perpendicular $k_{\perp}$ to primary dendrite growth as:

$$k_{\parallel} = g_1 k_1 + g_2 k_2 + \cdots \tag{4.42}$$

$$\frac{1}{k_{\perp}} = \frac{g_1}{k_1} + \frac{g_2}{k_2} + \cdots \tag{4.43}$$

where g_i is the volume fraction of phase i in a given control volume. Once these othrotropic thermal conductivities are known, a rotation tensor can be constructed to transform the values from directions along the dendrites to the analysis coordinate system. In general, the dendrites may be assumed to grow in the direction of the temperature gradient, but this is not always the case, especially in sharp corners. Depending upon the difference in conductivity between the phases, the heat flow can be significantly shunted in one direction, changing the solidification behavior at the solid-liquid interface. The difficulty in using this mixture law lies in the fact that the apparent thermal conductivity in the liquid is affected by turbulent flow in the bulk liquid and the local fluid-solid interactions around the dendrites.

For the sake of simplicity, this work uses the mass-fraction mixture law which has been used by many others [21,28,40]. Mizikar [29] proposed enhancing the thermal conductivity of

the liquid phase to account for convection and turbulence in the liquid pool. Choudhary *et al.* [8] investigated the value of the enhancement to the conductivity in the liquid, and found that an enhancement factor between 1 and 7 has little effect on the solidification behavior, and further increases in the enhancement factor retarded the solidification in their simulations of continuous casting. Nevertheless, in this work the thermal conductivity of the liquid phase is enhanced by a factor of 6.65 [15] to account for the effects of convection in the liquid pool:

$$k_{mix} = f_\ell k_\ell + f_\delta k_\delta + f_\gamma k_\gamma + f_\alpha k_\alpha \tag{4.44}$$

Thermal conductivity is a difficult quantity to measure accurately because steady-state conditions are required, and other modes of heat transfer are proportional to the temperature difference across a distance. Harste [13] compiled measurements from several sources of the thermal conductivity of plain-carbon steels over a variety of temperatures and compositions and fit a unified equation to the measurements:

$$k_\ell = 39.0 \cdot 6.65 \tag{4.45}$$

$$k_\delta = \left[21.6 + 8.35 \cdot 10^{-3} T\right]\left[1 - a_1 C^{a_2}\right] \tag{4.46}$$

$$k_\gamma = 20.14 + 9.313 \cdot 10^{-3} T \tag{4.47}$$

$$k_\alpha = \left[80.91 - 99.269 \cdot 10^{-3} T + 46.13 \cdot 10^{-6} T^2\right]\left[1 - a_1 C^{a_2}\right] \tag{4.48}$$

where temperatures are given in ºC, carbon compositions are given in %wt. C, and thermal conductivities are given in W/(m·K), k_{mix} is the mixture thermal conductivity and k_ℓ, k_δ, k_γ, and k_α are the thermal conductivities of the liquid, delta-ferrite, austenite, and alpha-ferrite phases, respectively. The ferrite phases where observed to have a noticeable dependence upon carbon composition, as manifested in the $\left[1 - a_1 C^{a_2}\right]$ terms, where the parameters a_1 and a_2 are calculated from:

$$a_1 = 0.425 - 0.4385 \cdot 10^{-3} T \tag{4.49}$$

$$a_2 = 0.209 + 1.09 \cdot 10^{-3} T \tag{4.50}$$

A plot of the mixture thermal conductivity against temperature is given in Figure 4.4 for the 0.045 %wt. C steel considered in this work.

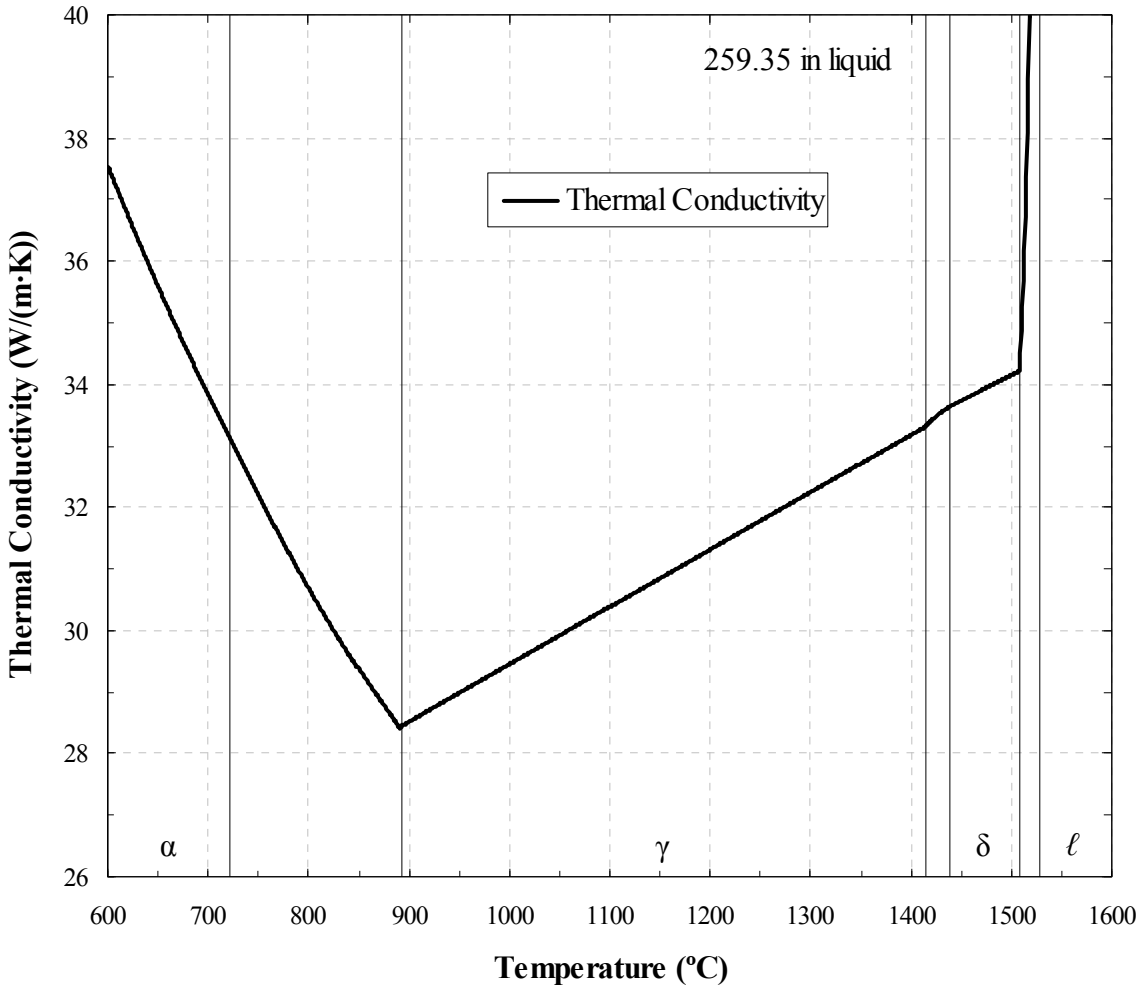

Figure 4.4. Thermal Conductivity of 0.045 %wt. C Steel

4.4. Model Verification with Analytical Solution

Most practical engineering problems do not lend themselves to closed-form analytical solutions. At the very least, the shape of the analysis domain leads to intractable mathematics. Realistic material properties, boundary conditions, and constitutive laws serve only to increase complexity. Analytical models easily provide information about the influence of different problem parameters on the solution, although they are restricted to simple, often one-dimensional domains and ideal constitutive behavior. Obtaining the same information from a numerical model requires a parametric study, incrementally changing one variable at a time and examining the effect upon the solution. Analytical solutions also provide the means to benchmark and verify (address programming issues and estimate numerical errors) numerical models.

Physicists and mathematicians began looking into change-of-phase problems that included a moving boundary in 1831 when Lamé and Clapeyron [25] considered a simple model for a solidifying liquid sphere. Stefan would also investigate the problem while looking into the melting and freezing of polar ice caps, publishing the first of a series of papers in 1889 [33]. Stefan would later become the eponym of the class of problems involving moving boundaries. Franz Neumann presented the more general solution of the moving-boundary problem, which accounts for superheat in the liquid region, in his lectures at Königsberg University in the 1860's [4], and his development is generally the adopted method for solving this class of problems.

The difficulty in solidification problems is that the position of the solidification front is unknown and it is coupled directly to the transient heat transfer solution. The boundary conditions of a problem of course dictate the tractability of the solution, and this class of problems has relatively few scenarios that yield a closed-form solution. Dantzig and Tucker [10] present a generalization of Neumann's solution that includes the casting mold in the analysis.

Consider a pure material (or eutectic alloy) in the liquid state with the uniform initial temperature T_0, which is greater than the melting temperature T_m of the material, solidifying in a mold whose surface temperature T_w is everywhere lower than T_m. The analysis domain is free of heat sources or heat sinks. The solidifying material has uniform, isotropic, and constant, but not necessarily equal, properties in the solid and liquid phases. For the purposes of verifying a numerical model, the properties in the solid and liquid will be taken as equal; the most general case is given elsewhere [10]. Similarly, the mold is assumed to have high heat extraction capabilities and have uniform and constant temperature T_w. The mass density of the material is included in the list of constant properties, which is an appropriate assumption for the nearly incompressible solid and liquid phases.

Note that practical casting materials are usually alloys that solidify over a range of temperatures, and have temperature-dependent thermophysical properties. The mold-solid interface governs the heat extraction by the mold that drives the solidification, and the interface heat transfer can be affected by air gaps caused by solidification shrinkage or by contamination with another material, such as scale build-up on the mold surface or mold flux powder entrapment. However, for the purposes of this solution assume that there is perfect contact everywhere along the mold-solid interface. Casting operations involve pouring the molten material into a mold, so generally the fluid motion cannot be ignored. Fluid flow can transport

heat by the bulk motion of the material, and can effect solidification by breaking the growing dendrites, mixing away the solute gradients, and introducing impurities and gas bubbles. In the interest of simplicity, this solution assumes no liquid or solid movement, so advection and viscous dissipation can be neglected in the entire solution.

Restricting the analysis to a one-dimensional plane Cartesian domain greatly simplifies the task at hand. Numerical solution of the one-dimensional Stefan problem has received considerable treatment over the past few years [9,11,12,14,35,36]. Two-dimensional solidification heat transfer solutions exist both numerically [26] and analytically [3], which both show good agreement with experimental results [18]. This particular analytical solution [3] for a wedge (a generalized corner) assumes a hyperbolic shape for the solidification front and uses a moving heat source to account for the energy required to change phases. King *et al*. [20] present a thorough review of the methods used to solve two-dimensional Stefan problems, which are not treated here. The assumption of a one-dimensional domain of course limits the validity of this solution to areas in molds away from corners and other two- or three-dimensional heat transfer effects. In addition to a one-dimensional domain, the solidifying material considered here extends out to infinity in one direction. The semi-infinite assumption makes the mathematics tractable but limits the validity of the solution to short times when considering finite domains.

Returning to the problem, the uniform surface temperature of the mold T_w is significantly lower than T_m such that solidification occurs immediately. This is equivalent to saying that at time $t = 0$, the surface temperature of the solidifying material is instantly lowered to T_w. The mold has a far-field temperature of T_0. As previously mentioned, the position of the solidification front must be determined simultaneously with the heat transfer solution, and for now it is defined as a general function of time $\delta = \delta(t)$. In the solid material, the governing equations and boundary conditions are:

$$\frac{\partial T}{\partial t} = \alpha_T \frac{\partial^2 T}{\partial x^2} \qquad \text{for } 0 < x \le \delta(t) \tag{4.51}$$

$$T = T_w \qquad \text{at } x = 0 \tag{4.52}$$

$$T = T_m \qquad \text{at } x = \delta(t) \tag{4.53}$$

In the liquid material, the governing equations and boundary conditions are:

$$\frac{\partial T}{\partial t} = \alpha_T \frac{\partial^2 T}{\partial x^2} \qquad \text{for } \delta(t) \le x < \infty \tag{4.54}$$

$$T = T_m \qquad \text{at } x = \delta(t) \tag{4.55}$$

$$T = T_0 \qquad \text{as } x \to \infty \tag{4.56}$$

The boundary condition at the solid-liquid interface is known as the Stefan condition, which equates the difference in heat fluxes to the heat liberated by the phase change:

$$k \left.\frac{\partial T}{\partial x}\right|_s - k \left.\frac{\partial T}{\partial x}\right|_\ell = \rho H_f \frac{d\delta}{dt} \qquad \text{at } x = \delta(t) \tag{4.57}$$

Since the far-field boundary conditions match the initial conditions for the liquid and mold, a similarity solution will reduce the partial differential equation that governs the heat conduction into an ordinary differential equation in terms of both x and t. The normalized Gaussian error function has the properties $\text{erf}(0) = 0$ and $\text{erf}(\pm\infty) = \pm 1$, which yield the desired behavior to match the boundary conditions given the form of the governing equation. The normalized error function is defined as:

$$\text{erf}(x) = \frac{2}{\sqrt{\pi}} \int_0^x \exp\left(-\xi^2\right) d\xi \tag{4.58}$$

The error function compliment is also used here, and is defined as:

$$\text{erfc}(x) = 1 - \text{erf}(x) \tag{4.59}$$

Assume a solution with:

$$T = c_1 + c_2 \,\text{erf}\left(\frac{x}{\sqrt{4\alpha_T t}}\right) \qquad \text{for } 0 < x \le \delta(t) \tag{4.60}$$

$$T = c_3 + c_4 \,\text{erf}\left(\frac{x}{\sqrt{4\alpha_T t}}\right) \qquad \text{for } \delta(t) \le x < \infty \tag{4.61}$$

Considering the temperature distribution in the solid, the mold-solid interface condition gives $c_1 = T_w$, and then the solid-liquid interface condition yields:

$$T_m = T_w + c_2 \,\text{erf}\left(\frac{\delta(t)}{\sqrt{4\alpha_T t}}\right) \tag{4.62}$$

Since T_m is constant by nature and T_w assumed to be a constant, the position of the interface $\delta(t)$ must be proportional to $\sqrt{t}$. For generality, introduce a constant ϕ and take:

$$\delta(t) = \phi\sqrt{4\alpha_T t} \tag{4.63}$$

Note that the velocity of the interface, or the solidification rate, is then given by:

$$\frac{d\delta}{dt} = \frac{\phi\sqrt{\alpha_T}}{\sqrt{t}} \tag{4.64}$$

The remaining constant in the temperature distribution can now be expressed in terms of the new constant $c_2 = (T_m - T_w)/\mathrm{erf}(\phi)$, thus the temperature distribution in the solid is:

$$T = T_w + \frac{T_m - T_w}{\mathrm{erf}(\phi)}\mathrm{erf}\left(\frac{x}{\sqrt{4\alpha_T t}}\right) \qquad \text{for } 0 < x \le \delta(t) \tag{4.65}$$

For later use, the temperature gradient in the solid is:

$$\frac{dT}{dx} = \frac{T_m - T_w}{\sqrt{\pi\alpha_T t}\,\mathrm{erf}(\phi)}\exp\left(-\frac{x^2}{4\alpha_T t}\right) \qquad \text{for } 0 < x \le \delta(t) \tag{4.66}$$

The far-field condition in the liquid gives:

$$T_0 = c_3 + c_4 \tag{4.67}$$

The solid-liquid interface temperature boundary condition gives:

$$T_m = c_3 + c_4\,\mathrm{erf}(\phi) \tag{4.68}$$

Combining these two conditions resolves the unknown constants:

$$c_3 = \frac{T_m - T_0\,\mathrm{erf}(\phi)}{\mathrm{erfc}(\phi)} \tag{4.69}$$

$$c_4 = \frac{T_0 - T_m}{\mathrm{erfc}(\phi)} \tag{4.70}$$

So then the temperature distribution in the liquid is:

$$T = T_0 - \frac{T_0 - T_m}{\mathrm{erfc}(\phi)}\mathrm{erfc}\left(\frac{x}{\sqrt{4\alpha_T t}}\right) \qquad \text{for } \delta(t) \le x < \infty \tag{4.71}$$

For later use, the temperature gradient in the liquid is:

$$\frac{dT}{dx} = \frac{T_m - T_0}{\mathrm{erfc}(\phi)\sqrt{\pi\alpha_T t}}\exp\left(-\frac{x^2}{4\alpha_T t}\right) \qquad \text{for } \delta(t) \le x < \infty \tag{4.72}$$

Now the constant ϕ must be determined, and the only boundary condition left to use is the Stefan condition. Upon substituting in the appropriate temperature gradients, letting $x = \delta(t)$ and simplifying, the resulting expression is:

$$\frac{c_p\left(T_m - T_w\right)}{H_f\sqrt{\pi}} = \phi\exp\left(\phi^2\right)\operatorname{erf}(\phi) + \frac{\operatorname{erf}(\phi)}{\operatorname{erfc}(\phi)}\frac{c_p\left(T_0 - T_m\right)}{H_f\sqrt{\pi}} \tag{4.73}$$

All terms in this expression are known except for the monotonically increasing variable ϕ, which can be found using any of the numerical root-finding techniques. The second term on the right-hand side of the above equation is the change to ϕ due to superheat. The description of the temperature solution is now complete.

To validate the finite-element heat transfer model of this work using the analytical solution derived above, a single column of 300 or 600 0.1-mm-square bilinear 4-node quadrilateral heat-transfer finite elements was used to mesh a 60 mm (or 30 mm) × 0.1 mm domain. As shown in Figure 4.5, the 30- or 60-mm edges are modeled as insulated, the 0.1-mm cold edge is given fixed a temperature boundary condition of T_w and the hot edge is insulated.

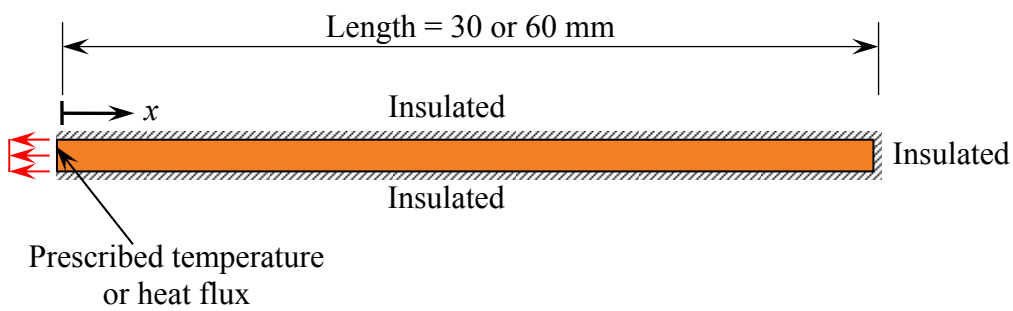

Figure 4.5. Solidification Test Problem Domain and Boundary Conditions

Table 4.2 gives the various conditions used in the validation problem. To accommodate the numerical solution, the melting point was approximated with a very narrow mushy zone. The boundary condition at the mold wall was enforced directly, which required a very small initial time step in the numerical simulation. Previous researchers [21] have used a convection boundary with a very high heat transfer coefficient to aid convergence; this technique is not necessary here because of the large number of iterations necessary anyway for convergence with the large superheat in the liquid material.

Table 4.2. Properties Used in Solidification Thermal Test Problem

Property	Symbol	Value	Units
Mass density	ρ	7500.0	kg/m³
Specific heat capacity	c_p	661.0	J/(kg·K)
Enthalpy of formation	H_f	272.0	kJ/kg
Thermal conductivity	k	33.0	W/(m·K)
Initial temperature	T_0	1525.0	ºC
Melting temperature	T_m	1495.0	ºC
Liquidus temperature	T_{liq}	1494.48	ºC
Solidus temperature	T_{sol}	1494.38	ºC
Mold wall temperature	T_w	1000.0	ºC

Figure 4.6 shows a comparison between the numerical solution to this problem (with the 30-mm domain) and the analytical solution just derived. At the given level of mesh resolution, the numerical solution matches very well with the analytical solution. The main mismatch between the methods occurs at the solidification front, which is caused by the mass lumping scheme used in the finite element method. On coarser meshes, this effect is manifested as the "wiggles" in the predicted shell thickness. The comparison between methods shows that in general, the numerical solution is no better than the width of the element in which the solidification front currently resides. Experimentation with this numerical verification exercise shows that in the case with zero superheat, the numerical solution is valid until the shell thickness is approximately the length of the domain. However, changing the hot edge boundary condition to a fixed temperature of T_0 delays solidification, by acting as a heat source.

Figure 4.7 shows that despite the favorable match of the spatial temperature solution, the prediction of the shell thickness eventually starts to deviate from the analytical solution. Reducing the maximum simulation time step from 0.1 seconds to 0.01 seconds reduced this error, as shown in Figure 4.8. Figure 4.9 shows that shell thickness predictions in the case without superheat match better, even with the larger timestep size. A convergence study of this problem without superheat has been performed elsewhere [28,40]. This study shows that the numerical solution is reasonably accurate within 2% for meshes with 2-mm elements and time steps of 0.1 seconds, which was the basis for mesh selection for simulations of the real process.

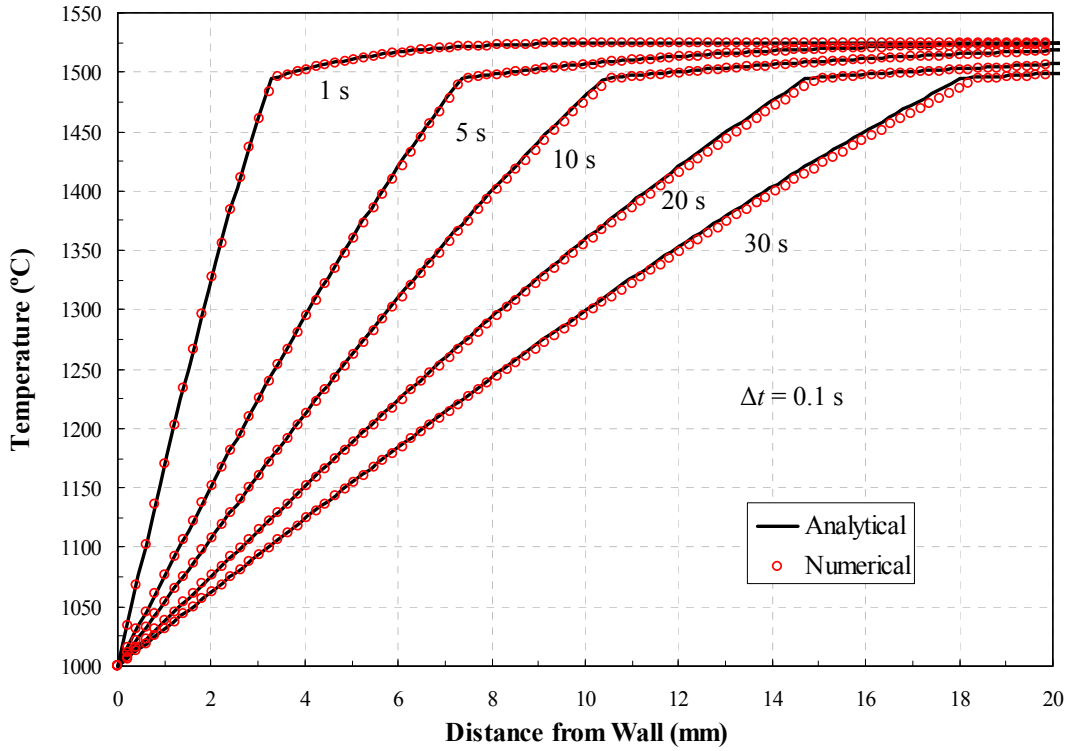

Figure 4.6. Solidification Test Problem Temperature Verification

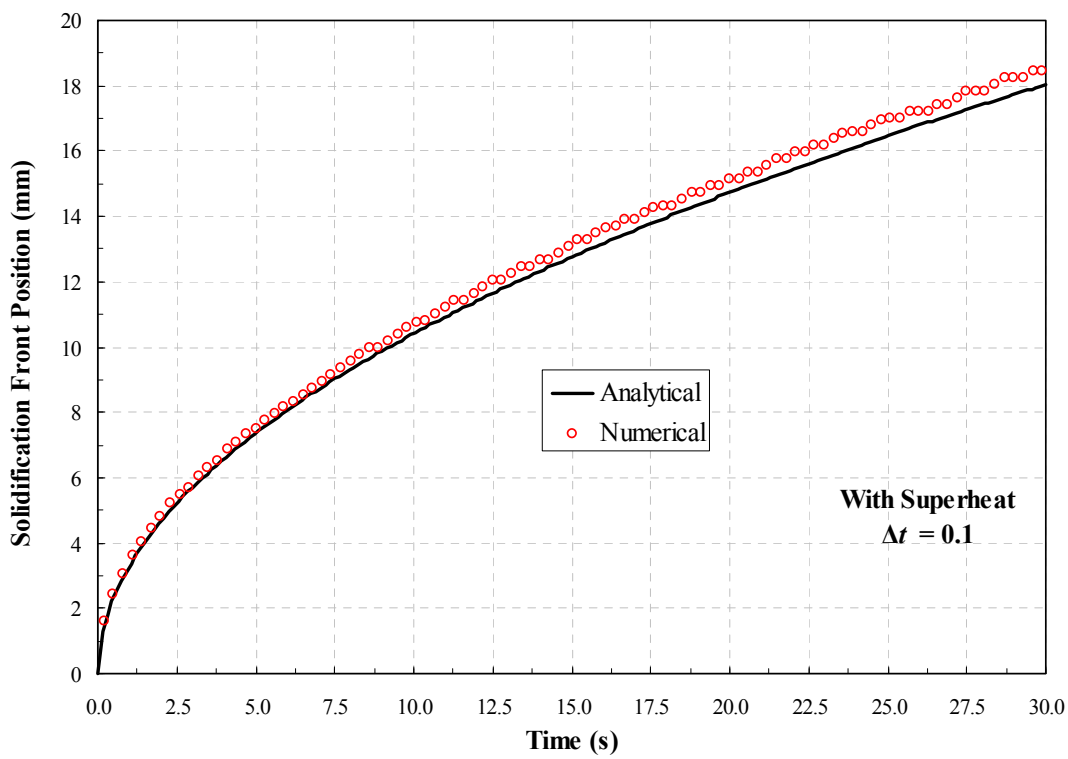

Figure 4.7. Shell Thickness Verification with Superheat, Large Time Step

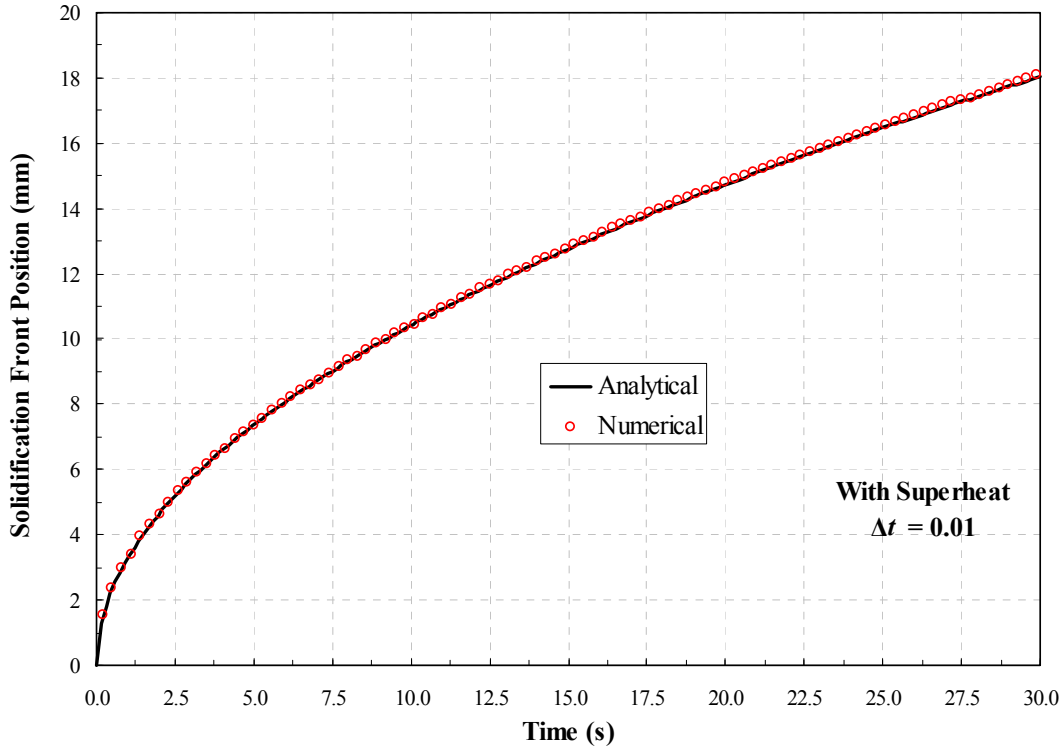

Figure 4.8. Shell Thickness Verification with Superheat, Small Time Step

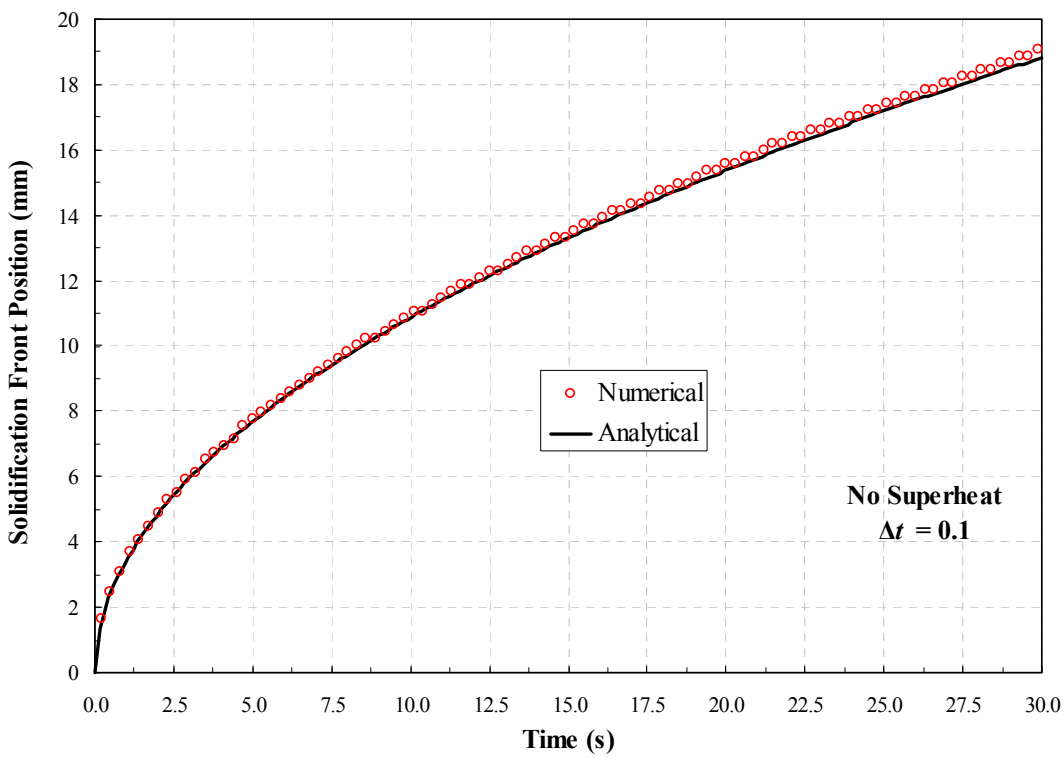

Figure 4.9. Shell Thickness Verification without Superheat

4.5. Shell Model Setup

A finite element model of the solidifying shell was constructed to investigate the effect of the funnel mold geometry on the thermal behavior of the shell. The model takes advantage of the two-fold symmetry present in funnel molds, and also considers only a two-dimensional slice that moves at the casting speed down the mold, as discussed in Section 4.2. The material properties are defined as discussed above for a 0.045 %wt. C steel. The analysis domain, as shown in Figure 4.10, is initialized to the pouring temperature of the molten steel, 1545 ºC, and the surface that would be in contact with the mold hot face is given a prescribed heat flux boundary conditions, which was calculated with CON1D and validated with plant measurements, which is the subject of Chapter 3.

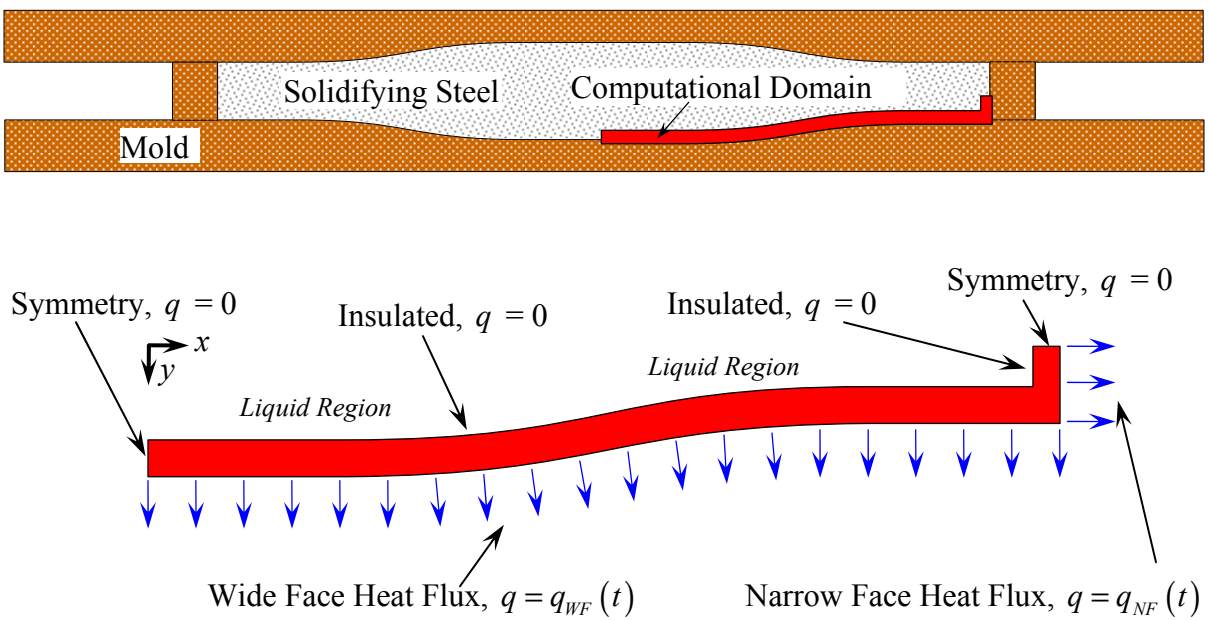

Figure 4.10. Schematic of Computational Domain and Boundary Conditions

The symmetry planes have the appropriate zero normal heat flux boundary condition. The analysis domain does not include the entire quadrant of the two-dimensional slice plane; the region closest to the center of the plane will always be in the liquid state while the analysis plane is in the mold, so inclusion in this analysis is not necessary and will only serve to increase the computational cost. As discussed earlier, the necessary thickness of the analysis domain is approximately twice the expected shell thickness at mold exit, and in this work the domain thicknesses used are 20 and 25 mm. The inner surface, which is always liquid, is modeled as

thermally insulated in this work. The actual behavior of the material in the liquid region can be calculated with simulations of the fluid flow, and does affect the results of the solidification heat transfer modeled here by advecting superheated liquid throughout the liquid pool in the casting machine. This is left for future work, and the results of the present work should be interpreted accordingly. For example, the jet of molten steel leaving the SEN contains the most superheat of the domain, and the point at which the jet impinges upon the narrow face shell is known to be locally thinner than its surroundings because of it [16,39].

The two-dimensional heat transfer found in the corner of the domain increases the local heat removal rate, which causes the shell to grow the fastest in the corner. However, due to lack of constraint, the solidification shrinkage (*cf.* Chapter 5) causes the shell in the corner to pull away from the mold, thereby opening a gap and reducing the heat flow out of the shell. While it is certainly possible to construct a numerical model of the solidifying shell which includes this strongly nonlinear coupling between heat transfer and gap size [21,28], in this work a much simpler approach is adopted to save computational effort. The heat applied heat flux in the corner region is reduced by a certain percentage to simulate the effect of the gap opening. In the present work, this reduction factor grows from zero at 20 mm away from the corner to 50% at the corner itself, as illustrated in Figure 4.11. Comparison of the calculated temperature field with previous work [21,28] shows that this method of treating the corner produces both reasonable shell temperatures and shell thicknesses. Better treatment of the gap requires a fully coupled thermo-mechanical model, accurate mold temperatures, and information about the composition of the gap, and measurements for calibration, and is left for future work.

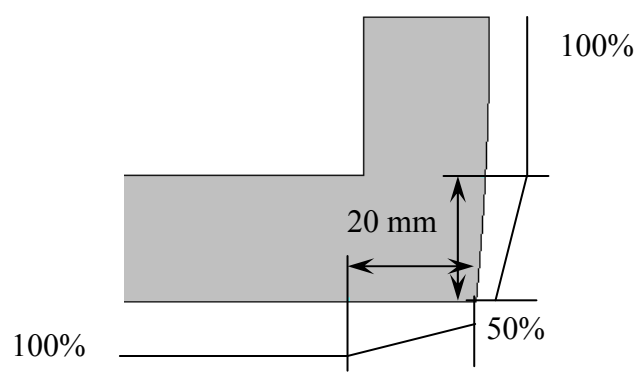

Figure 4.11. Treatment of Interfacial Heat Flux Boundary in Corner Region

The finite-element mesh used in this work was constructed by a simple preprocessing program that takes as input the dimensions of the different geometric features of a funnel mold, as explained in Chapter 2, and builds a mesh accordingly. This approach saves the effort of building a mesh by hand for every simulation case and allows for easy study of the effects of the funnel geometry. All meshes consist of standard four-node, "fully integrated" (2×2 Gaussian quadrature) bilinear quadrilateral finite elements, which are slightly biased towards the shell-mold interface for increased accuracy in the solid region while saving computational effort in the liquid region that is present in the numerical model, as shown in Figure 4.12. Node and element counts are given in the next section with the discussion of results.

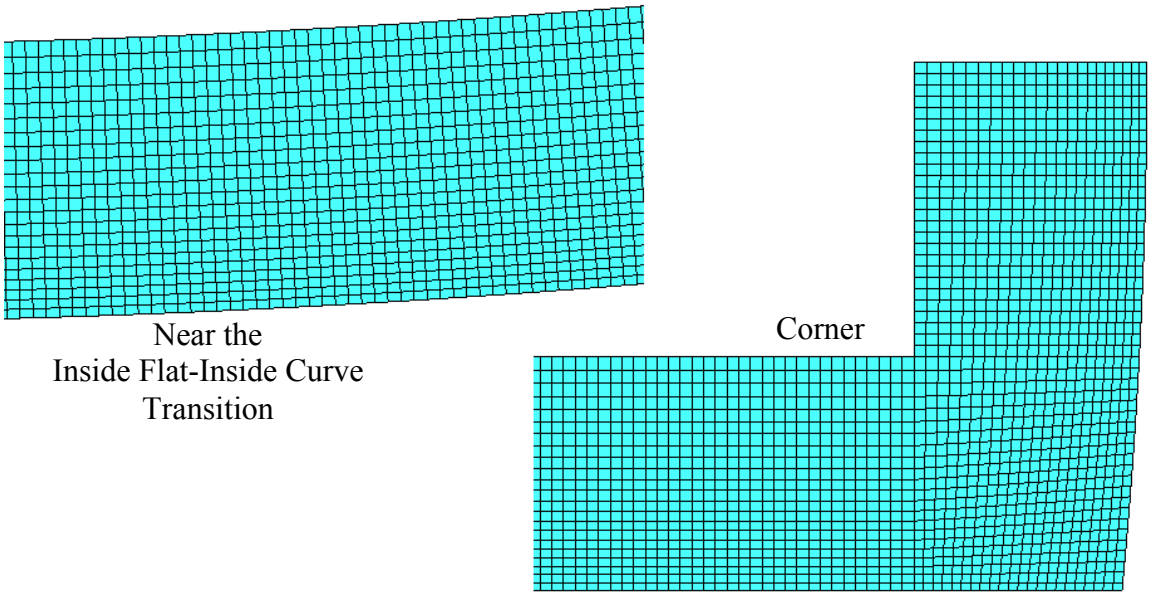

Figure 4.12. Detail of Finite Element Mesh of Solidifying Shell

4.6. Shell Model Results

Typical results from the thermal model investigation are presented below. These "typical" results are examined in the through-thickness direction as well as around the perimeter of the domain, and then a short parametric study is performed to investigate the effect of funnel geometry on the thermal behavior of the solidifying shell.

4.6.1. Through-Thickness Direction

Typical temperature predictions through the thickness of the shell are shown in Figures 4.13 and 4.14 for several times in the simulation, i.e., several distances below the meniscus, and

several positions below the surface of the shell. The surface is of course always the coldest location due to the heat removal at the interface, and the effect of increasing the thermal conductivity to account for convection is manifested in the very low temperature gradients in the liquid region. In general, the temperature gradients are stronger at the surface than near the solidification front. The solid-state phase change from delta-ferrite to austenite has little effect on the thermal response of the steel, in both space and time, because the enthalpy of formation for that phase change is so low and the thermal properties are relatively similar.

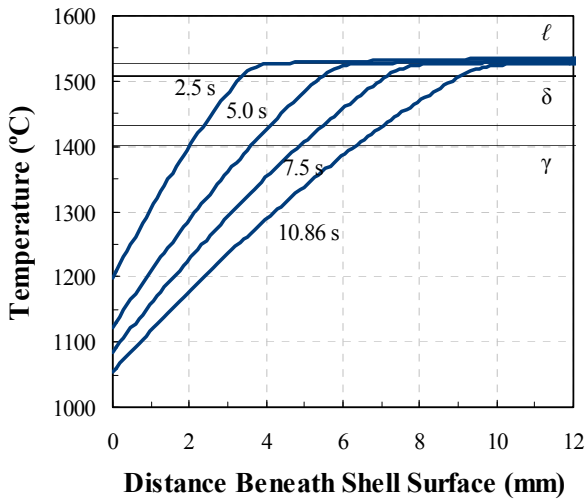

Figure 4.13. Through-Thickness Shell Temperatures

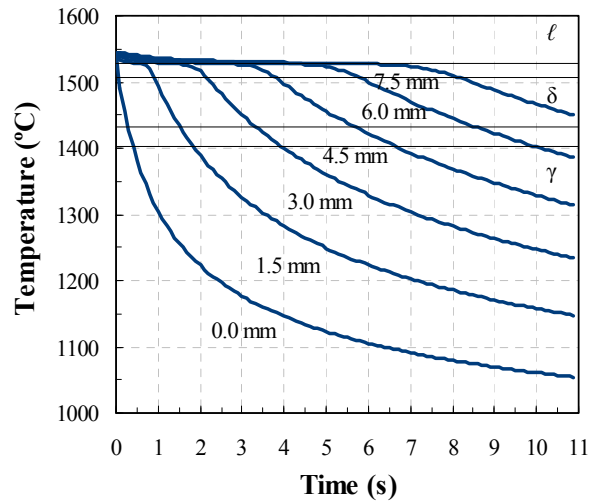

Figure 4.14. Shell Temperature Histories

The temperature history data can be used to reconstruct the spatial results in the casting direction, which is presented in Figure 4.15. The profile of the shell is evident in the shape of the isotherm lines, and the results can be further processed for the model predictions of shell thickness, which is presented in Figure 4.16. The mushy zone is observed to increase in thickness as the shell moves down the mold, which will have consequences for crack formation, as discussed in Chapter 5.

4.6.2. Circumferential Direction

A contour plot of the temperature field of the slice domain at mold exit is shown in Figure 4.17. The plot shown is for the A-type mold discussed in Chapter 2. The field is smooth everywhere around the perimeter, and the minimum temperature in the corner of 960 ºC indicates that the treatment of the heat flux in the corner is a reasonable approach. The surface

temperatures around the perimeter of the shell are shown at different times in Figure 4.18, and with the geometric features delineated, it is clearly seen that the funnel geometry has a slight two-dimensional effect on the thermal behavior of the solidifying shell. The inner and outer flat regions have identical temperatures, and from that temperature the inner curve region is at most 3.4 ºC cooler and the outer curve region is at most 3.3 ºC warmer. The transition from the flat region temperature value to the curved region temperature (where $\partial T/\partial x \neq 0$) occurs over 50 mm for both the inside and outside curve regions, while the transition from the inside curve temperature to the outside curve temperature occurs over nearly 60 mm.

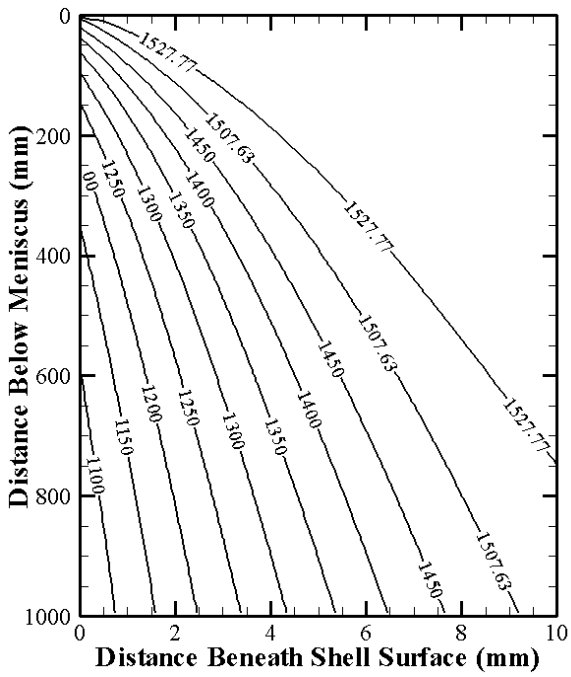

Figure 4.15. Temperature Field in Casting Direction

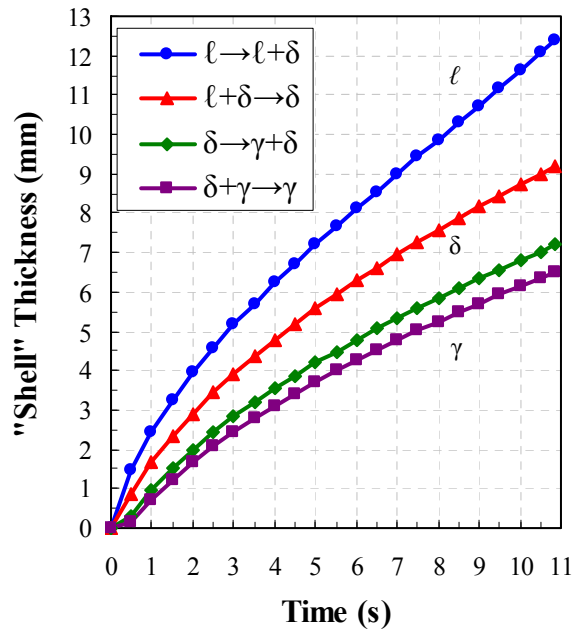

Figure 4.16. Shell Thickness Profiles

Several hypothetical funnel molds based on the A-type design presented in Chapter 2 were studied with identical boundary conditions and properties while systematically varying the funnel geometry. The geometry and model sizes and run times (using 2 CPUs on a Dell PowerEdge 1750 Linux Cluster with Intel Xeon 3.2 GHz processors) of the cases presented here are summarized in Table 4.3, and the surface temperatures at 500 mm below the meniscus (halfway down the mold) are presented in Figure 4.19. All cases used a mold length of 1100 mm and funnel length of 850 mm. None of the cases exhibited large changes in shell thickness in the transition region compared with in the flat regions, even at early times. The largest calculated

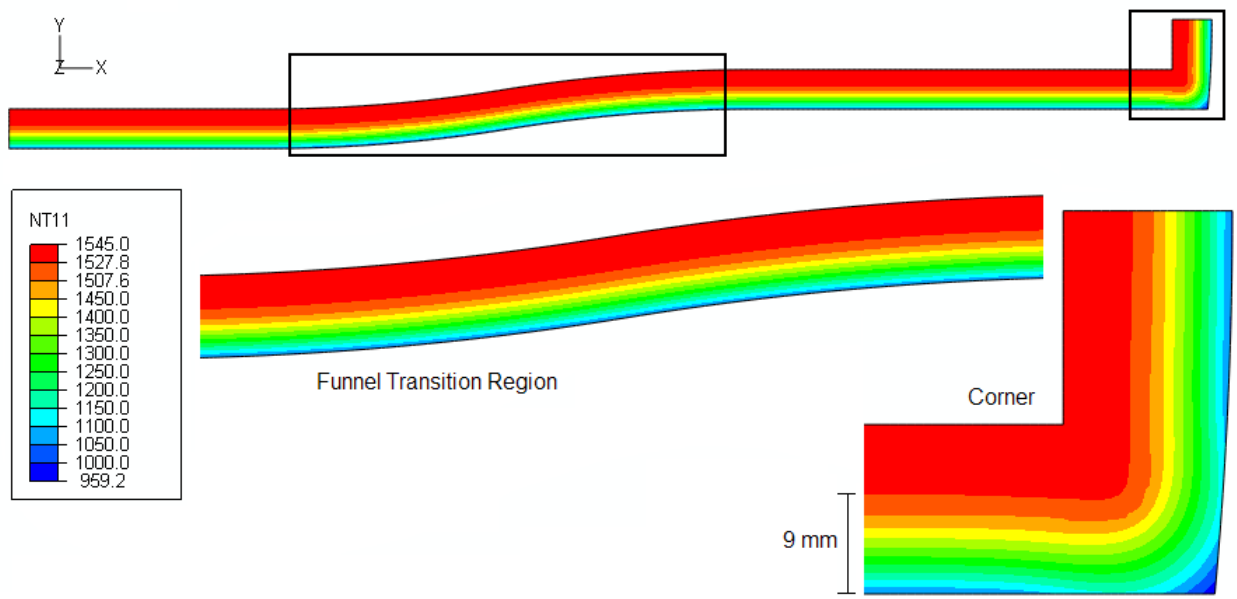

Figure 4.17. Two-Dimensional Temperature Results at Mold Exit

difference in shell thickness was 35 μm by mold exit (case 5). The width of the regions of $\partial T/\partial x \neq 0$ seems to be constant across the different cases, and is likely a function only of the thermal diffusivity of the steel and the heat load. In general, the difference in temperature between the flat regions and the curved regions decreases with increasing funnel width and decreasing crown, *i.e.*, the effect of the funnel geometry on the thermal behavior of the shell reduces as the funnel approaches a completely parallel mold. Similar results were found in a study of the shell in B-type molds. These trends are also observed in the results of previous work [22,32], though they did not attempt to quantify the results. A review of the funnel geometry in Chapter 2 indicates that a single parameter, the horizontal plane funnel radius r_h, can be related with the temperature difference in the funnel transitions regions relative to the flat regions, which is discussed next.

Table 4.3. Summary of Funnel Geometries Simulated for Thermal Behavior Study

Case	Description	Funnel Geometry (mm)				Simulation Data		
		w_i	w_0	c_T	c_B	Nodes	Elements	Runtime (hr)
1	Base Case	130	375	23.4	8	15456	14762	3.52
2	No Inner Flat	0	375	23.4	8	15456	14762	3.48
3	Wider Funnel	130	475	23.4	8	15479	14784	3.49
4	Shallow Crown	130	375	13	8	15456	14762	3.46
5	Deep Crown	130	375	48	8	15456	14762	3.47

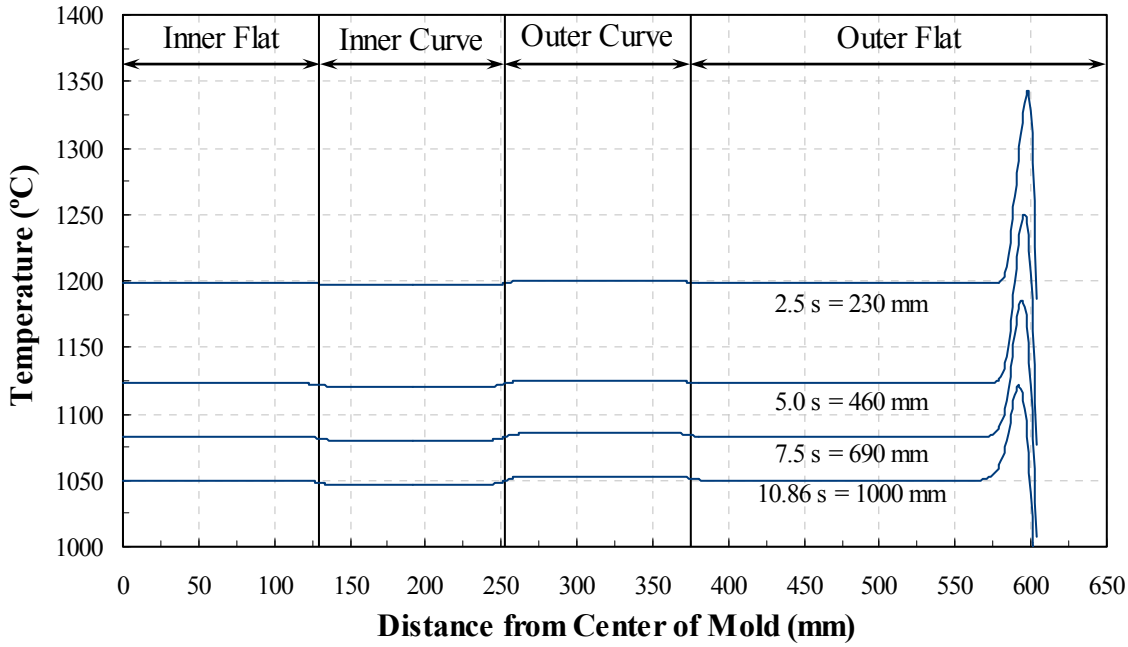

Figure 4.18. Shell Surface Temperatures at Different Times

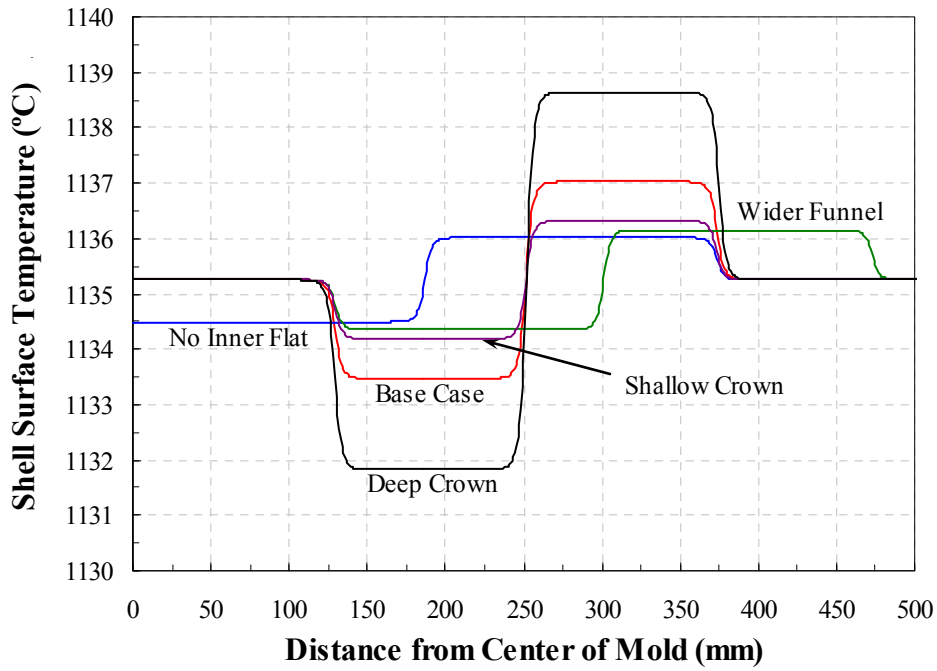

Figure 4.19. Effect of Funnel Geometry on Shell Surface Temperature

The funnel transition region, regardless of its shape, serves to locally increase or decrease the heat extraction from the steel shell because of its two-dimensional nature. This effect can be

quantified easily by considering only conduction effects in the conservation of energy equation on a simple curved domain using cylindrical coordinates in one dimension. Motivated by the scaling arguments in Section 4.2.1, consider the conduction in the "through-shell-thickness" direction only of a slice through the shell with a fixed temperature on the hot liquid side and a prescribed heat flux to remove heat from the cold surface. This analysis is applied to a rectilinear domain, representative of the regions away from the funnel transition and the corners, and is applied to a slice of cylindrical domain with no conduction in the circumferential direction, representative of the funnel transition region. The locations of these sample domains in the solidifying shell are shown in the inset of Figure 4.20. The models in both coordinate systems neglect conduction in the casting direction. The energy conservation equation with constant thermal conductivity is:

$$0 = \nabla^2 T \tag{4.74}$$

In one rectilinear dimension, this reduces to:

$$0 = \frac{d^2 T}{dx^2} \tag{4.75}$$

which has the general solution:

$$T(x) = c_1 x + c_2 \tag{4.76}$$

Subject to a fixed-temperature boundary of $T = T_0$ at $x = \ell$ gives $c_2 = T_0 - c_1 \ell$, and a specified heat flux boundary $q = -k(dT/dx)$ gives $c_1 = -q/k$, so the temperature distribution is given by:

$$T(x) = T_0 - (q/k)(x - \ell) \tag{4.77}$$

In cylindrical coordinates, the governing equation (4.72) reduces to:

$$0 = \frac{d}{dr}\left(r \frac{dT}{dr} \right) \tag{4.78}$$

which has the general solution:

$$T(r) = c_1 \ln(r) + c_2 \tag{4.79}$$

This domain presents two scenarios, i.e. the case where heat flows from the inner radius (where temperature is fixed) to the outer radius (where heat flux is extracted), as in the "inner curve" regions of the funnel, and the opposite case, which is representative of the "outer curve" regions of the funnel. The fixed temperature boundary gives $c_2 = T_0 - c_1 \ln(R_o)$ if applied at the outside

radius $r = R_o$ or $c_2 = T_0 - c_1 \ln(R_i)$ if applied at the inside radius $r = R_i$. The corresponding specified heat flux boundary $q = -k(dT/dr)r$ gives $c_1 = -qR_i/k$ if applied on the inside radius, or $c_1 = qR_o/k$ if applied on the outside radius. Thus, the temperature distribution if the heat flux is applied on the inner radius ("outer curve" region) is:

$$T(r) = T_0 - qR_i/k \ln(r/R_o) \tag{4.80}$$

Alternatively, the temperature distribution for the heat flux applied on the outer radius ("inner curve" region) is:

$$T(r) = T_0 + qR_o/k \ln(r/R_i) \tag{4.81}$$

Figure 4.20 compares the three though-shell-thickness temperature profiles in terms of distance away from the heat flux boundary with k = 33 W/(m·K), T_0 = 1525 ºC, q = 1000 kW/m² outward, R_i = 675 mm, R_o = 700 mm, and ℓ = 25 mm. As intuitively expected, when heat flux is extracted from the outer radius, which is a gentle outside corner that enhances two-dimensional heat transfer, heat flowing through the domain diverges so the temperatures are slightly cooler than the rectilinear case. Similarly, when heat flux is extracted from the inner radius, heat flowing through the domain converges so the temperatures are slightly warmer. The horizontal radii found in funnel molds are on the order of the given size and larger, and with larger radii the difference between the rectilinear and cylindrical cases becomes even smaller.

This exercise shows that variations in shell surface temperature, though small, are caused by the geometry of the mold, due to changes in curvature associated with the funnel shape. The shell that solidifies along the inner curve regions of the funnel is expected to have a slightly cooler surface, and the shell solidifying along outer curves is expected to be slightly hotter. The variations depend on the curvature. For the conditions assumed here, surface temperature variations of about 13 ºC are predicted with Equations.(4.78) and (4.79). This overpredicts the variations relative to the numerical variations of about 6 ºC observed in Figure 4.19, owing to geometry oversimplification and ignoring solidification. However, the analytical solution does reveal that the surface temperature variations are caused by two-dimensional conduction effect associated with the funnel, which increases in proportion to decreasing horizontal funnel radius. Later sections of this work will show that these seemingly small differences in temperature have

the potential for severe consequences in the resulting mechanical behavior of the shell, given the sensitivity of constitutive laws to temperature at elevated temperatures.

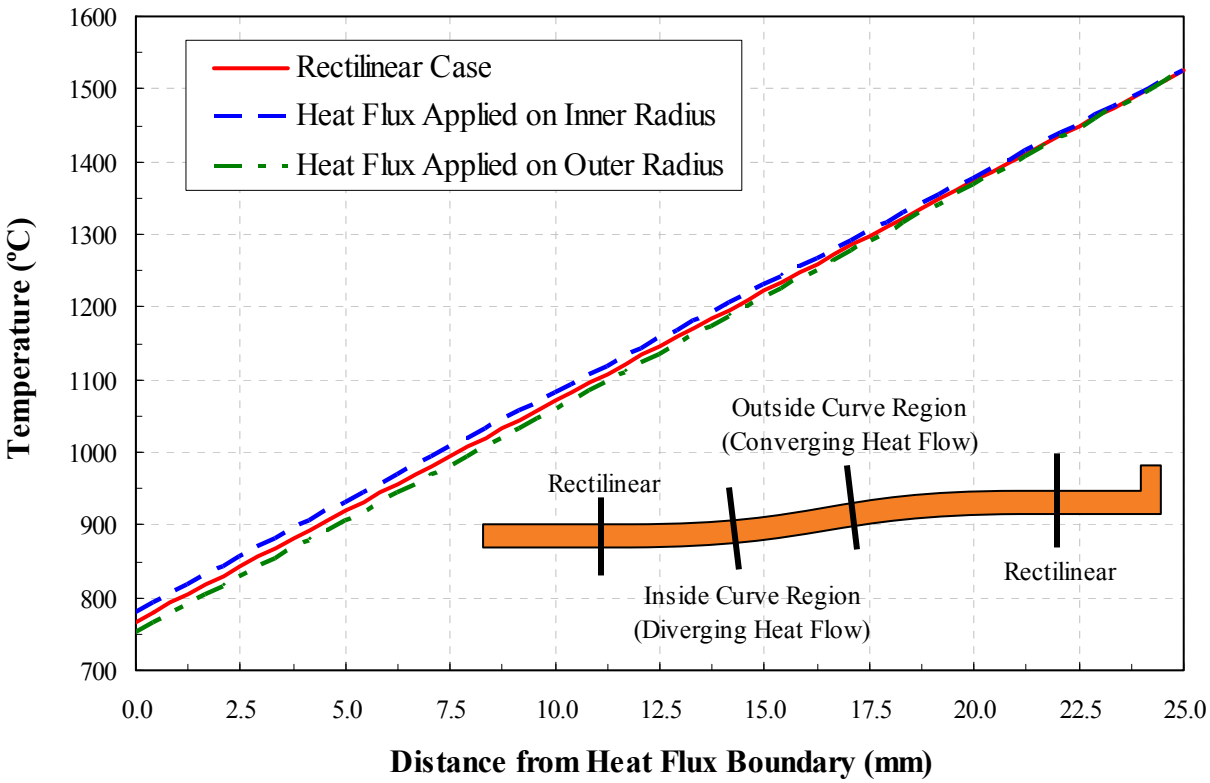

Figure 4.20. Analytical Predictions of Through-Thickness Temperatures for Different Radii

4.7. Conclusions

Mathematical models have been employed to study the effect of funnel geometry on the thermal behavior of the solidifying shell in continuous casting funnel molds. After verifying a two-dimensional finite-element model with an analytical solution of solidification, the model was used to simulate the thermal behavior of the solidifying shell using an interfacial heat flux profile that was calibrated with plant measurements. The funnel geometry is responsible for cooling the inside curve region of the funnel slightly faster than the flat regions, and similarly responsible for cooling the outside curve region slightly slower. These effects have almost no influence on the temperature in the solidifying shell in the funnel transition region. A parametric study of the funnel geometry revealed that this geometric effect is reduced as the funnel gets shallower and wider, and a simple analytical model identified that change in temperature can be

characterized by the horizontal radius of the funnel. The heat transfer model and results presented here are investigated using the thermal-mechanical model in the next chapter.

4.8. References

1. *ABAQUS 6.8-1 User Manuals*. (2008), Dassault Simulia, Inc., 166 Valley Street, Providence, RI, USA 02909-2499.
2. C. Bonacina, G. Comini, A. Fasano, and M. Primicerio, "Numerical Solution of Phase-Change Problems." *International Journal of Heat and Mass Transfer*, **16** (1973), pg. 1825-1832.
3. H. Budhia and F. Kreith, "Heat Transfer with Melting or Freezing in a Wedge." *International Journal of Heat and Mass Transfer*, **16** (1973), pg. 195-211.
4. H.S. Carslaw and J.C. Jaeger, *Conduction of Heat in Solids*, 2e. Oxford University Press, (1959).
5. S.E. Chidiac, J.K. Brimacombe, and I.V. Samarasekera, "A New Transient Method for Analysis of Solidification in the Continuous Casting of Metals." *Applied Scientific Research*, **51** (1993), pg. 573-597.
6. G. Comini, S. del Guidice, R.W. Lewis, and O.C. Zienkiewicz, "Finite Element Solution of Non-Linear Heat Conduction Problem with Special Reference to Phase Change." *International Journal for Numerical Methods in Engineering*, **8** (1974), pg. 613-624.
7. R.D. Cook, D.S. Malkus, M.E. Plesha, and R.J. Witt, *Concepts and Applications of Finite Element Analysis*, 4e. John Wiley and Sons, (2002).
8. S.K. Choudhary, D. Mazumdar, and A. Ghosh, "Mathematical Modelling of Heat Transfer Phenomena in Continuous Casting of Steel." *ISIJ International*, **33**:7 (1993), pg. 764-774.
9. A.B. Crowley, "Numerical Solution of Stefan Problems." *International Journal of Heat and Mass Transfer*, **21** (1978), pg. 215-219.
10. J.A. Dantzig and C.L. Tucker III, *Modeling in Materials Processing*, 1e. Cambridge University Press, (2001).
11. L.E. Goodrich, "Efficient Numerical Technique for One-Dimensional Thermal Problems with Phase Change." *International Journal of Heat and Mass Transfer*, **21** (1978), pg. 615-621.
12. V. Gülkaç, "On the Finite Differences Schemes for the Numerical Solution of Two-Dimensional Moving Boundary Problem." *Applied Mathematics and Computation*, **168** (2005), pg. 549-556.
13. K. Harste, "Untersuchungen zur Schrumpfung und zur Entstehung von Mechanischen Spannungen Während der Erstarrung und Nachfolgender Abkühlung Zylindrischer Blöcke aus Fe-C-Legierungen." Ph.D. Dissertation, Technischen Universität Clausthal, (1989).
14. M.A. Hastaoglu, "A Numerical Solution to Moving Boundary Problems—Application to Melting and Solidification." *International Journal of Heat and Mass Transfer*, **29**:3 (1986), pg. 495-499.

15. X. Huang and B.G. Thomas, "Modeling of Transient Flow Phenomena in Continuous Casting of Steel." *Canadian Metallurgical Quarterly*, **37**:3-4 (1998), pg. 197-212.

16. X. Huang, B.G. Thomas, and F.M. Najjar, "Modeling Superheat Removal During Continuous Casting of Steel Slabs." *Metallurgical and Materials Transactions*, **23B**:3 (1992), pg. 339-356.

17. F.P. Incropera and D.P. DeWitt, *Fundamentals of Heat and Mass Transfer*, 5e. John Wiley and Sons, (2002).

18. L.M. Jiji, K.A. Rathjen, and T. Drzewiecki, "Two-Dimensional Solidification in a Corner." *International Journal of Heat and Mass Transfer*, **13** (1970), pg. 215-218.

19. A. Kagawa and T. Okamoto, "Influence of Alloying Elements on Temperature and Composition for Peritectic Reaction in Plain Carbon Steels." *Materials Science and Technology*, **2**:10 (1986), pg. 997-1008.

20. J.R. King, D.S. Riley, and A.M. Wallman, "Two-Dimensional Solidification in a Corner." *Proceedings of the Royal Society – Mathematical, Physical and Engineering Sciences (Series A)*, **455** (1999), pg. 3449-3470.

21. S. Koric and B.G. Thomas, "Efficient Thermo-Mechanical Model for Soldification Processes." *International Journal for Numerical Methods in Engineering*, **66**:12 (2006), pg. 1955-1989.

22. S. Koric, L.C. Hibbeler, and B.G. Thomas, "Explicit Coupled Thermo-Mechanical Finite Element Model of Steel Solidification." *International Journal for Numerical Methods in Engineering*, **78**:1 (2009), pg. 1-31.

23. E.Y. Kung and J.C. Pollock, "A Mathematical Model of Heat Transfer in Continuous Casting." *Simulation*, **10**:1 (1968), pg. 29-36.

24. J.E. Lait, J.K. Brimacombe, and F. Weinberg, "Mathematical Modeling of Heat Flow in the Continuous Casting of Steel." *Ironmaking and Steelmaking*, **1**:2 (1974), pg. 90-97.

25. G. Lamé and B.P. Clapeyron, "Memoire sur la Solidification par Refroidissement d'un Globe Liquide." *Annales Chimie Physique*, **47** (1831), pg. 250-256.

26. A. Lazaridis, "A Numerical Solution of the Multidimensional Solidification (or Melting) Problem." *International Journal of Heat and Mass Transfer*, **13** (1970), pg. 1459-1477.

27. E.C. Lemmon, "Multidimensional Integral Phase Change Approximations for Finite Element Conduction Codes." In *Numerical Methods in Heat Transfer*, Edited by R. Lewis, K. Morgan, and O.C. Zienkiewicz, John Wiley and Sons, (1981), pg. 201-213.

28. C. Li and B.G. Thomas, "Thermo-Mechanical Finite-Element Model of Shell Behavior in Continuous Casting of Steel." *Metallurgical and Materials Transactions*, **35B**:6 (2004), pg. 1151-1172.

29. E.A. Mizikar, "Mathematical Heat Transfer Model for Solidification of Continuously Cast Steel Slabs." *Transactions of the Metallurgical Society of AIME*, **239**:11 (1967), pg. 1747-1753.

30. H. Nam, H.-S. Park, and J.K. Yoon, "Numerical Analysis of Fluid Flow and Heat Transfer in the Funnel Type Mold of a Thin Slab Caster." *ISIJ International*, **40**:9 (2000), pg. 886-892.

31. H.-S. Park, H. Nam, and J.K. Yoon, "Numerical Analysis of Fluid Flow and Heat Transfer in the Parallel Type Mold of a Thin Slab Caster." *ISIJ International*, **41**:9 (2001), pg. 974-980.

32. J.K. Park, "Thermo-Mechanical Phenomena in High Speed Continuous Casting Processes." Ph.D. Dissertation, The University of British Columbia, (2002).

33. J. Stefan, Über die Theorie der Eisbildung, "Insbesondere über die Eisbildung im Polarmeere." *Akademie der Wißenschaften Wiens*, **98** (1889), pg. 965-983.

34. B.G. Thomas, I.V. Samarasekera, and J.K. Brimacombe, "Comparison of Numerical Modeling Techniques for Complex, Two-Dimensional, Transient Heat Conduction Problems." *Metallurgical and Materials Transactions*, **15B**:2 (1984), pg. 307-318.

35. V. Voller and M. Cross, "Accurate Solutions of Moving Boundary Problems Using the Enthalpy Method." *International Journal of Heat and Mass Transfer*, **24** (1981), pg. 545-556.

36. V. Voller and M. Cross, "An Explicit Numerical Method to Track a Moving Phase Change Front." *International Journal of Heat and Mass Transfer*, **26**:1 (1983), pg. 147-150.

37. V.R. Voller, C.R. Swaminathan, and B.G. Thomas, "Fixed Grid Techniques for Phase Change Problems: A Review." *International Journal for Numerical Methods in Engineering*, **30** (1990), pg. 875-898.

38. Y.-M. Won and B.G. Thomas, "Simple Model of Microsegregation During Solidification of Steels." *Metallurgical and Materials Transactions*, **32A**:7 (2001), pg. 1755-1767.

39. B. Zhao, B.G. Thomas, S.P. Vanka, and R.J. O'Malley, "Transient Fluid Flow and Superheat Transport in Continuous Casting of Steel Slabs." *Metallurgical and Materials Transactions*, **36B**:6 (2005), pg. 801-823.

40. H. Zhu, "Coupled Thermal-Mechanical Finite-Element Model with Application to Initial Solidification." Ph.D. Dissertation, The University of Illinois at Urbana-Champaign, (1993).

41. O.C. Zienkiewicz, R.L. Taylor, and J.Z. Zhu, *The Finite Element Method: Its Basis and Fundamentals*, 6e. Elsevier, (2005).

CHAPTER 5

MECHANICAL BEHAVIOR OF THE SOLIDIFYING SHELL

5.1. Introduction

The mechanical behavior of the solidifying steel shell is mostly driven by the thermal strains that arise during solidification, but is also influenced greatly by the constitutive equation of the material, contact with the mold surface, and ferrostatic pressure. The equations that describe the mechanical behavior of the solidifying steel are discussed below, as well as their representation into a finite-element model. This mathematical description of the shell is then implemented into a computational model and used to investigate the behavior of the solidifying shell in continuous casting funnel molds, to predict longitudinal facial cracks, and to recommend improved funnel designs.

Many numerical models have been used to investigate the thermomechanical behavior of the solidifying shell in continuous casting molds since the pioneering work by Grill, Brimacombe, and Weinberg [7], but the mold geometry has been limited to conventional slabs [29,34,35], billets [24,30,36,38,41], rounds [9,21,32,33], and beam-blanks [4,10,16,22]. The thermomechanical behavior of the shell in funnel molds seems to have first been investigated by Park [31] in two dimensions and by Koric in three dimensions [16], but these studies did not quantitatively investigate the effect of funnel geometry.

5.2. Governing Equations and Their Finite-Element Representation

The description of changes in position, orientation, shape, and size of a solid body is the subject of the field of kinematics, while the description of the forces that cause said changes are studied in the field of dynamics. These areas are connected through the constitutive response of the material, and all of these come together in the field of continuum mechanics [2], which has created the mathematical framework to describe in the general deformation of solid bodies. The equations are solved using the finite-element method with the commercial code ABAQUS augmented with user-defined subroutines. The numerical solution process is briefly summarized, as complete details are given elsewhere [17].

Consider a solid body in an initial / reference configuration at a reference time t_0, and a current/deformed configuration at some later time t. Every material point is described relative

to a global coordinate system with a position vector in the initial configuration and a position vector $\boldsymbol{x}$ in the current configuration, as shown in Figure 5.1. The displacement $\boldsymbol{u}$ of a material point is calculated according to:

$$\boldsymbol{u}\left(\boldsymbol{x}^{\circ},t\right)=\boldsymbol{x}\left(\boldsymbol{x}^{\circ},t\right)-\boldsymbol{x}^{\circ} \tag{5.1}$$

The deformation gradient tensor $\boldsymbol{F}$ maps a material fiber in the reference configuration $d\boldsymbol{x}^{\circ}$ to the current configuration $d\boldsymbol{x}$ according to:

$$d\boldsymbol{x}=\boldsymbol{F}\cdot d\boldsymbol{x}^{\circ} \tag{5.2}$$

The deformation gradient is invertible and is related to the displacement gradient $\nabla\boldsymbol{u}$ (taken with respect to the reference configuration) through the following relation:

$$\boldsymbol{F}=\boldsymbol{I}+\nabla\boldsymbol{u} \tag{5.3}$$

where $\boldsymbol{I}$ is the second-order identity tensor.

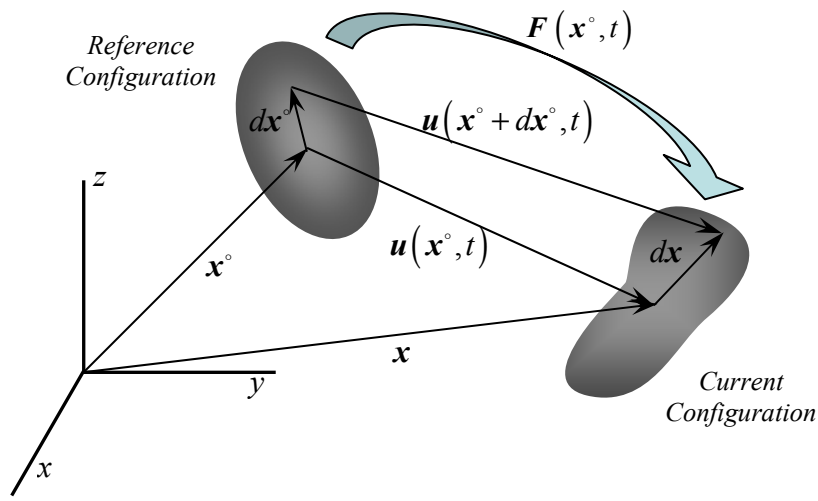

Figure 5.1. General Deformation of a Solid Body

The polar decomposition theorem allows the deformation gradient to be expressed in terms of a stretch and a rotation:

$$\boldsymbol{F}=\boldsymbol{R}\cdot\boldsymbol{U}=\boldsymbol{V}\cdot\boldsymbol{R} \tag{5.4}$$

where $\boldsymbol{R}$ is a proper orthogonal rotation tensor ($\det\left(\boldsymbol{R}\right)=+1$), $\boldsymbol{U}$ is the right stretch tensor, and $\boldsymbol{V}$ is the left stretch tensor. Use of the right stretch tensor indicates that the material is first stretched and then rotated, while the left stretch tensor indicates the reverse. The deformation

gradient is used to define the right Cauchy-Green deformation tensor $\boldsymbol{C}$, which describes the stretch ratios of a material fiber along principal deformation directions:

$$\boldsymbol{C} = \boldsymbol{F}^T \cdot \boldsymbol{F} = \boldsymbol{U}^2 \tag{5.5}$$

The deformation tensors above can be used to define different strain tensors, including the Green-Lagrange strain tensor $\boldsymbol{E}$, which is used in this work:

$$\boldsymbol{E} = \frac{1}{2}\left(\boldsymbol{C} - \boldsymbol{I}\right) \tag{5.6}$$

The Green-Lagrange strain tensor exhibits the desirable property of being identically zero when the deformation consists only of rotation. In terms of the displacement gradient, the Green-Lagrange strain is:

$$\boldsymbol{E} = \frac{1}{2}\left(\nabla\boldsymbol{u} + \left(\nabla\boldsymbol{u}\right)^T + \left(\nabla\boldsymbol{u}\right)^T \cdot \nabla\boldsymbol{u}\right) \tag{5.7}$$

The Cauchy stress tensor $\boldsymbol{\sigma}$ relates the traction vector $\boldsymbol{t}$ and unit outward normal vector $\boldsymbol{n}$ of a surface, all in the current configuration, by:

$$\boldsymbol{t} = \boldsymbol{n} \cdot \boldsymbol{\sigma} \tag{5.8}$$

Considering a body force (*e.g.*, gravity) field $\boldsymbol{b}$, the current mass density ρ, and the local material acceleration vector $\ddot{\boldsymbol{u}}$, conservation of linear momentum implies the local force balance at any material point:

$$\nabla \cdot \boldsymbol{\sigma}\left(\boldsymbol{x}\right) + \boldsymbol{b}\left(\boldsymbol{x}\right) = \rho\ddot{\boldsymbol{u}}\left(\boldsymbol{x}\right) \tag{5.9}$$

Conservation of angular/rotational momentum requires the Cauchy stress tensor to be symmetric, or that $\boldsymbol{\sigma} = \boldsymbol{\sigma}^T$. Similarly, in the reference frame, the first Piola-Kirchhoff stress tensor $\boldsymbol{P}$ relates the traction vector $\boldsymbol{t}^\circ$ and the unit outward normal vector $\boldsymbol{n}^\circ$ through:

$$\boldsymbol{t}^\circ = \boldsymbol{n}^\circ \cdot \boldsymbol{P} \tag{5.10}$$

The local force balance is similarly expressed in the reference configuration for a body force field $\boldsymbol{b}^\circ$, mass density ρ°, and local acceleration $\ddot{\boldsymbol{u}}^\circ$:

$$\nabla \cdot \boldsymbol{P}\left(\boldsymbol{x}^\circ\right) + \boldsymbol{b}^\circ\left(\boldsymbol{x}^\circ\right) = \rho^\circ\ddot{\boldsymbol{u}}^\circ\left(\boldsymbol{x}^\circ\right) \tag{5.11}$$

In general, the first Piola-Kirchhoff stress tensor is not symmetric, though conservation of angular momentum is still satisfied. For the problem at hand, the deformation of the material occurs over "long" periods of time (the deformation rates are many orders of magnitude slower

than the wave speed of the material [18]), so the inertial terms may be neglected in any configuration. The Cauchy and first Piola-Kirchhoff stress tensors are related through:

$$\boldsymbol{P} = \det\left(\boldsymbol{F}\right)\boldsymbol{F}^{-1}\cdot\boldsymbol{\sigma} \tag{5.12}$$

The solidifying steel in the mold can experience crack formation even when subjected to only a few percent of strain [34]. Several previous numerical models of the solidifying shell in conventional slabs and billets have shown that the deformation gradients are small when the steel shell is still in the mold [17,24,40]. This is also the case for the bending of the solidifying shell as it moves through a funnel mold. Although the displacements and rotations are certainly finite in some regions of the shell, the displacement *gradients* are still small enough for the small-strain theory to apply. The analysis performed here thus adopts the conventional small-strain measure and the static force balance in the current configuration:

$$\nabla\cdot\boldsymbol{\sigma} + \boldsymbol{b} = \boldsymbol{0} \tag{5.13}$$

For the "small" displacement gradients of interest in this work, several simplifications of the above development can be made, namely that the reference and current configurations of the body are nearly identical. Thus, the Green-Lagrange strain tensor is approximately equal to the conventional small strain tensor $\boldsymbol{\varepsilon}$, identified below. Mathematically, this gives:

$$d\boldsymbol{x} \approx \boldsymbol{R}\cdot d\boldsymbol{x}^{\circ} \tag{5.14}$$

$$\boldsymbol{F} \approx \boldsymbol{R}\cdot\left(\boldsymbol{I}+\boldsymbol{\varepsilon}\right) \tag{5.15}$$

$$\boldsymbol{E} \approx \boldsymbol{\varepsilon} = \frac{1}{2}\left(\nabla\boldsymbol{u} + \left(\nabla\boldsymbol{u}\right)^{T}\right) \tag{5.16}$$

$$\boldsymbol{P} \approx \boldsymbol{R}^{-1}\cdot\boldsymbol{\sigma} \tag{5.17}$$

If in addition, the rotations were small, then the Cauchy and first Piola-Kirchhoff stress tensors would be approximately equal, and the deformation gradient simply sum of the identity tensor and the small strain tensor. These approximations are reasonable for conventional casting mold geometries and has been used in previous work.

The final governing equation for the solid mechanics problem is the compatibility of the strain field, *i.e.*, the condition that no overlaps or gaps open in the domain. For small strains, this requirement is expressed as:

$$\nabla\times\boldsymbol{\varepsilon}\times\nabla = 0 \tag{5.18}$$

This compatibility condition for the strain field is enforced automatically when using the finite-element method, which calculates strains from the displacements based on Equation. 5.16. An issue that bears the same name arises in the finite element method, where the mesh should be prevented from opening holes. This is not a concern in the formulation of the finite element method used here since the displacement field is continuous by construction.

The continuous casting model developed in this work assumes that heat conduction in the casting direction is negligible, reducing the problem to two dimensions. The corresponding treatment for the mechanical problem is to assume a condition of "generalized plane strain" in the casting direction, where the out-of-plane displacement of the analysis domain is constrained to follow a plane (no warping, no out-of-plane bending). This assumption is valid since the material above and below the analysis plane prevents the shell from bending. Mathematically, this reduces the force balance to just two dimensions and imposes the out-of-plane resultant forces F_x and moments M_x and M_y:

$$F_z = \int_\Omega \sigma_{zz} d\Omega \tag{5.19}$$

$$M_x = \int_\Omega x\sigma_{zz} d\Omega \tag{5.20}$$

$$M_y = \int_\Omega y\sigma_{zz} d\Omega \tag{5.21}$$

The strains also become two-dimensional, with the out-of-plane normal strain specified by:

$$\varepsilon_{zz} = c_0 + c_x x + c_y y \tag{5.22}$$

where c_0, c_x, and c_y are constants determined as a part of the solution, and the out-of-plane shearing strains ε_{xz} and ε_{yz} are equal to zero. One plane of symmetry in the analysis domain forces one of the generalized plane strain constants to zero since one of the out-of-plane resultant moments vanishes. Two or more planes of symmetry forces c_x and c_y both to be zero in accordance with no out-of-plane bending, $M_x = M_y = 0$, which is the case in the present work.

Well-posed mechanics boundary-value problems also require boundary conditions for each degree of freedom on every portion of the domain. A solid body can be described by its interior Ω, where the force balance equation must hold, and its surface Γ, where boundary conditions must be specified. Valid boundary conditions include either specified displacements $\boldsymbol{u} = \boldsymbol{u}_{sp}$ on part of the boundary Γ_u, specified surface tractions $\boldsymbol{t} = \boldsymbol{t}_{sp}$ on part of the boundary

Γ_t, or a combination of the two. The force balance is specified by Equation (5.13) with generalized plane strain condition Equation (5.22) to reduce the dimensionality to two, and the strain-displacement relationship is specified by Equation (5.16). The final relationship necessary to solve this mechanics problem relating forces and displacements is a constitutive law to relate stress and strain, and is discussed later.

The above governing partial differential equations are solved by employing the Bubnov-Galerkin finite element method [5,42] to cast the equations in weak form and force the residual error to zero in an average sense. The residual $\{R\}$ of the static force balance is:

$$\{R\} = \int_{\Omega} [B]^T \{\sigma\} d\Omega - \int_{\Omega} [N]^T \{b\} d\Omega - \int_{\Gamma_t} [N]^T \{t\} d\Gamma \tag{5.23}$$

where $[N]$ and $[B]$ are the matrix of element basis functions and their spatial derivatives, $\{\sigma\}$ is the Voigt vector of the Cauchy stress tensor, $\{b\}$ is the body force vector and $\{t\}$ is the surface traction vector. An incremental approach is used to integrate the governing equation through time, where the solution variables at the end of an increment are updated from their values at the beginning of the step. The displacement field is updated with incremental displacements $\{\Delta u\}$ according to:

$$\{u^{t+\Delta t}\} = \{u^t\} + \{\Delta u\} \tag{5.24}$$

The total strain field is updated with incremental strains $\{\Delta\varepsilon\}$ by:

$$\{\varepsilon^{t+\Delta t}\} = \{\varepsilon^t\} + \{\Delta\varepsilon\} \tag{5.25}$$

The incremental strains are calculated from the incremental displacements according to the strain-displacement relation Equation (5.16) at the midpoint of an increment:

$$\{\Delta\varepsilon\} = \frac{1}{2}\left(\frac{\partial \Delta u}{\partial\left(u^t + \frac{1}{2}\Delta u\right)} + \left(\frac{\partial \Delta u}{\partial\left(u^t + \frac{1}{2}\Delta u\right)} \right)^T \right) \tag{5.26}$$

The generalized plain strain condition is also enforced incrementally. The stress field, body force field, and surface tractions are updated according to:

$$\{\sigma^{t+\Delta t}\} = \{\sigma^t\} + \{\Delta\sigma\} \tag{5.27}$$

$$\{b^{t+\Delta t}\} = \{b^t\} + \{\Delta b\} \tag{5.28}$$

$$\left\{t^{t+\Delta t}\right\} = \left\{t^{t}\right\} + \left\{\Delta t\right\} \tag{5.29}$$

The single-step, fully-implicit "Backward Euler" method is employed to march the system through time, and so the residual is evaluated at the new time level and the above definitions of stress, body forces, and surface tractions are substituted into the equation:

$$\begin{aligned}\left\{R^{t+\Delta t}\right\} = &\int_{\Omega}\left[B\right]^{T}\left(\left\{\sigma^{t}\right\}+\left\{\Delta\sigma\right\}\right)d\Omega \\ &-\int_{\Omega}\left[N\right]^{T}\left(\left\{b^{t}\right\}+\left\{\Delta b\right\}\right)d\Omega+\int_{\Gamma}\left[N\right]^{T}\left(\left\{t^{t}\right\}+\left\{\Delta t\right\}\right)d\Gamma\end{aligned} \tag{5.30}$$

Owing to the linearity of the integration operator, the above may be re-cast as:

$$\begin{aligned}\left\{R^{t+\Delta t}\right\} = &\int_{\Omega}\left[B\right]^{T}\left\{\sigma^{t}\right\}d\Omega-\int_{\Omega}\left[N\right]^{T}\left\{b^{t}\right\}d\Omega+\int_{\Gamma}\left[N\right]^{T}\left\{t^{t}\right\}d\Gamma \\ &+\int_{\Omega}\left[B\right]^{T}\left\{\Delta\sigma\right\}d\Omega-\int_{\Omega}\left[N\right]^{T}\left\{\Delta b\right\}d\Omega+\int_{\Gamma}\left[N\right]^{T}\left\{\Delta t\right\}d\Gamma\end{aligned} \tag{5.31}$$

The first line of the above equation is clearly the residual at the start of an increment, which is taken as zero by virtue of the finite-element method. The residual at the end of an increment is then expressed as simply:

$$\left\{R^{t+\Delta t}\right\} = \int_{\Omega}\left[B\right]^{T}\left\{\Delta\sigma\right\}d\Omega-\int_{\Omega}\left[N\right]^{T}\left\{\Delta b\right\}d\Omega+\int_{\Gamma}\left[N\right]^{T}\left\{\Delta t\right\}d\Gamma \tag{5.32}$$

Forcing this residual to zero in order to achieve static equilibrium is a nonlinear problem requiring iteration, and in this work the Newton-Raphson (NR) method is employed, owing to its strong convergence rates. The NR method uses a Taylor series expansion of the residual at the next iteration $i+1$ about the solution variable, which in this case is the incremental displacement vector $\left\{\Delta u_i\right\}$ at iteration i:

$$\left\{R_{i+1}^{t+\Delta t}\right\} = \left\{R_{i}^{t+\Delta t}\right\} + \left.\frac{\partial\left\{R^{t+\Delta t}\right\}}{\partial\left\{\Delta u\right\}}\right|_{\left\{\Delta u\right\}=\left\{\Delta u_i\right\}}\left\{\delta\Delta u\right\} + O\left(\left\|\delta\Delta u\right\|^{2}\right) \tag{5.33}$$

The goal is to force $\left\{R_{i+1}^{t+\Delta t}\right\}$ to zero, and the correction to the incremental displacement vector $\left\{\delta\Delta u\right\}$ can then be found by solving the following matrix equation:

$$\left.\frac{\partial\left\{R^{t+\Delta t}\right\}}{\partial\left\{\Delta u\right\}}\right|_{\left\{\Delta u\right\}=\left\{\Delta u_i\right\}}\left\{\delta\Delta u\right\} = \left[T\right]\left\{\delta\Delta u\right\} = -\left\{R_{i}^{t+\Delta t}\right\} \tag{5.34}$$

where $\left[T\right]$ is the tangent operator, calculated by differentiating the residual in Equation (5.32):

$$[T]=\frac{\partial\{R^{t+\Delta t}\}}{\partial\{\Delta u\}}=\int_{\Omega}[B]^{T}\frac{\partial\{\Delta\sigma\}}{\partial\{\Delta u\}}d\Omega-\int_{\Omega}[N]^{T}\frac{\partial\{\Delta b\}}{\partial\{\Delta u\}}d\Omega+\int_{\Gamma}[N]^{T}\frac{\partial\{\Delta t\}}{\partial\{\Delta u\}}d\Gamma \tag{5.35}$$

The body forces are generally not functions of displacement, so the second term on the right-hand side is dropped. Applying the chain rule inside the first term gives:

$$[T]=\int_{\Omega}[B]^{T}\frac{\partial\{\Delta\sigma\}}{\partial\{\Delta\varepsilon\}}\frac{\partial\{\Delta\varepsilon\}}{\partial\{\Delta u\}}d\Omega+\int_{\Gamma}[N]^{T}\frac{\partial\{\Delta t\}}{\partial\{\Delta u\}}d\Gamma \tag{5.36}$$

This form of the tangent operator identifies the "material Jacobian" $[J]=\partial\{\Delta\sigma\}/\partial\{\Delta\varepsilon\}$, which depends on the constitution of the material, discussed shortly. The derivative of the total strain with respect to the displacement field is the matrix of spatial derivatives of the element basis functions, $[B]$, which gives:

$$[T]=\int_{\Omega}[B]^{T}[J][B]d\Omega+\int_{\Gamma}[N]^{T}\frac{\partial\{\Delta t\}}{\partial\{\Delta u\}}d\Gamma \tag{5.37}$$

The residual, calculated from Equation (5.32), and the tangent operator, calculated from Equation (5.37), are used in Equation (5.34) to solve for the correction to the incremental displacements. The improved guess of the incremental displacements are then calculated with:

$$\{\Delta u_{i+1}\}=\{\Delta u_{i}\}+\{\delta\Delta u\} \tag{5.38}$$

This NR procedure is carried out until the infinity norm (maximum absolute value of any element) of both the residual $\{R^{t+\Delta t}\}$ and the displacement correction $\{\delta\Delta u\}$ vectors are sufficiently small. Convergence is assumed to be achieved here when the norm of the residual at the end of a step is less than 1% of the norm of the time-averaged force in the domain, and when the norm of the incremental displacement correction is less than 2% of the norm of the displacement increment.

The commercial finite element code ABAQUS [1] is used in this work to solve the global force balance as defined above, owing to its robust contact algorithms. The calculation of the material Jacobian, stress increment, and decomposition of the total strain into its various parts all depend on the constitutive behavior of the material, as discussed next, and are implemented into ABAQUS through the user subroutine UMAT.

At high temperatures, the mechanical response of solid steel is sensitive to the rate at which the material is loaded, commonly described as elastic-viscoplastic behavior. The

mechanical effects can be decomposed into recoverable elastic behavior (associated with chemical bond stretching) and irrecoverable inelastic behavior. The inelastic effects include both rate-insensitive plasticity as well as rate-sensitive creep, although at high temperatures they are difficult to distinguish [24]. Following the (Kröner-) Lee multiplicative decomposition of the deformation gradient [15,20], the deformation of the solidifying shell, at a higher level of abstraction, is composed of mechanical deformation gradients $\boldsymbol{F}^{mech}$ and also thermal deformation gradients $\boldsymbol{F}^{th}$:

$$\boldsymbol{F} = \boldsymbol{F}^{th} \cdot \boldsymbol{F}^{mech} \tag{5.39}$$

The development here is based on this general equation, but it is worth noting that with both small strains and small rotations, the above would simplify to:

$$\boldsymbol{\varepsilon} = \boldsymbol{\varepsilon}^{th} + \boldsymbol{\varepsilon}^{mech} \tag{5.40}$$

where $\boldsymbol{\varepsilon}^{th}$ is the thermal strain tensor and $\boldsymbol{\varepsilon}^{mech}$ is the mechanical strain tensor.

All materials exhibit an effect known as thermal expansion, which corresponds to the fact that at different temperatures the constituent molecules vibrate and move by different amounts, and thus have different average spacing at equilibrium with no load. This effect results in temperature-dependent mass density $\rho(T)$. Most materials, including steel, contract in size with decreasing temperature, which generates compressive (negative) thermal strain. Another effect that behaves like thermal strain is the change in molecular lattice spacing with changes in crystal structure, such as the solid-state phase change from ferrite (alpha or delta) to austenite. The coefficient of thermal expansion α_E can be calculated from the mass density to include both of these effects according to:

$$\alpha_E(T) = \frac{1}{T_{ref} - T}\left(1 - \sqrt[3]{\frac{\rho(T_{ref})}{\rho(T)}}\right) \tag{5.41}$$

where T_{ref} is a reference temperature, chosen in this work to be the solidus temperature of the steel. The coefficient of thermal expansion is used to calculate the *isotropic* thermal deformation gradient according to:

$$\boldsymbol{F}^{th} = \boldsymbol{R}^{th}\left(\boldsymbol{I} + \boldsymbol{\varepsilon}^{th}\right) = \boldsymbol{R}^{th}\left(\boldsymbol{I} + \boldsymbol{I}\int_{T_0}^{T} \alpha_E(T)\,dT\right) \tag{5.42}$$

where T_0 and T are the initial and current temperatures of a material point, and $\boldsymbol{R}^{th}$ is a rotation that accompanies the thermal deformation. However, since the thermal expansion is assumed to be isotropic, this thermal rotation has no effect on the deformation gradient to within the order of the small-strain approximation, so:

$$\boldsymbol{F}^{th} = \boldsymbol{I}\left(1+\int_{T_0}^{T} \alpha_E\left(T\right)dT\right) \tag{5.43}$$

The thermal deformation is treated incrementally, so:

$$\Delta\boldsymbol{F}^{th} = \boldsymbol{I} + \Delta\boldsymbol{\varepsilon}^{th} \tag{5.44}$$

where the incremental thermal strain $\Delta\boldsymbol{\varepsilon}^{th}$ is calculated by [1]:

$$\Delta\boldsymbol{\varepsilon}^{th} = \left(\alpha_E\left(T^{t+\Delta t}\right)\left(T^{t+\Delta t}-T_{ref}\right)-\alpha_E\left(T^{t}\right)\left(T^{t}-T_{ref}\right)\right)\boldsymbol{I} \tag{5.45}$$

Note that this definition ensures that no thermal strain will be generated at initial temperatures different from the chosen reference temperature. The incremental thermal strain is subtracted from the total strain so that the UMAT subroutine is only responsible for dividing the remaining mechanical strain into its elastic and inelastic parts.

The velocity gradient tensor at a material point is defined as:

$$\boldsymbol{L} = \nabla\dot{\boldsymbol{u}} = \nabla\boldsymbol{v} = \dot{\boldsymbol{F}}\cdot\boldsymbol{F}^{-1} \tag{5.46}$$

The thermal and mechanical deformation gradients define their respective velocity gradients:

$$\boldsymbol{L}^{th} = \dot{\boldsymbol{F}}^{th}\cdot\left(\boldsymbol{F}^{th}\right)^{-1} \tag{5.47}$$

$$\boldsymbol{L}^{mech} = \dot{\boldsymbol{F}}^{mech}\cdot\left(\boldsymbol{F}^{mech}\right)^{-1} \tag{5.48}$$

though in general they do not add directly to form the total velocity gradient. In fact,

$$\boldsymbol{L} = \dot{\boldsymbol{F}}^{th}\left(\boldsymbol{F}^{th}\right)^{-1} + \boldsymbol{F}^{th}\left(\dot{\boldsymbol{F}}^{mech}\cdot\left(\boldsymbol{F}^{mech}\right)^{-1}\right)\left(\boldsymbol{F}^{th}\right)^{-1} = \boldsymbol{L}^{th} + \boldsymbol{F}^{th}\boldsymbol{L}^{mech}\left(\boldsymbol{F}^{th}\right)^{-1} \tag{5.49}$$

However, since the thermal deformation gradient is isotropic, the above reduces to just:

$$\boldsymbol{L} = \boldsymbol{L}^{th} + \boldsymbol{L}^{mech} \tag{5.50}$$

The velocity gradient tensor can be decomposed into its symmetric part $\boldsymbol{D}$, called the rate-of-deformation tensor, and its skew-symmetric part $\boldsymbol{W}$, called the spin tensor:

$$\boldsymbol{L} = \boldsymbol{D} + \boldsymbol{W} \tag{5.51}$$

$$\boldsymbol{D} = \frac{1}{2}\left(\boldsymbol{L}+\boldsymbol{L}^{T}\right) \tag{5.52}$$

$$\boldsymbol{W} = \frac{1}{2}\left(\boldsymbol{L} - \boldsymbol{L}^T\right) \tag{5.53}$$

With the simplified total velocity gradient, the decomposition into thermal and mechanical components is simply:

$$\boldsymbol{D} = \boldsymbol{D}^{th} + \boldsymbol{D}^{mech} \tag{5.54}$$

$$\boldsymbol{W} = \boldsymbol{W}^{th} + \boldsymbol{W}^{mech} \tag{5.55}$$

with isotropic thermal behavior, the thermal spin tensor is zero, giving:

$$\boldsymbol{W} = \boldsymbol{W}^{mech} \tag{5.56}$$

Along similar arguments as above, the mechanical deformation gradient can be decomposed into its elastic $\boldsymbol{F}^{el}$ and inelastic $\boldsymbol{F}^{ie}$ parts:

$$\boldsymbol{F}^{mech} = \boldsymbol{F}^{el} \cdot \boldsymbol{F}^{ie} \tag{5.57}$$

Again, this development is based on this general equation, but it is worth noting that for small strains and small rotations, the above would simplify to:

$$\boldsymbol{\varepsilon}^{mech} = \boldsymbol{\varepsilon}^{el} + \boldsymbol{\varepsilon}^{ie} \tag{5.58}$$

where $\boldsymbol{\varepsilon}^{el}$ is the elastic strain tensor and $\boldsymbol{\varepsilon}^{ie}$ is the inelastic strain tensor. The elastic deformation gradient is calculated from:

$$\boldsymbol{F}^{el} = \boldsymbol{R}^{el}\left(\boldsymbol{I} + \boldsymbol{\varepsilon}^{el}\right) \tag{5.59}$$

where $\boldsymbol{R}^{el}$ is a rotation accompanying the elastic deformation. The elastic behavior of the material is assumed to be isotropic in this work, so this rotation has no effect on the elastic deformation gradient to within the order of the small-strain approximation, leaving just:

$$\boldsymbol{F}^{el} = \boldsymbol{I} + \boldsymbol{\varepsilon}^{el} \tag{5.60}$$

The assumption of isotropic elasticity allows the velocity gradient decomposition into the rate-of-deformation and spin as follows:

$$\boldsymbol{D} = \boldsymbol{D}^{th} + \boldsymbol{D}^{el} + \boldsymbol{D}^{ie} \tag{5.61}$$

$$\boldsymbol{W} = \boldsymbol{W}^{el} + \boldsymbol{W}^{ie} \tag{5.62}$$

Isotropic small-strain elasticity has a zero spin tensor, so the total continuum spin has a contribution only from the inelastic effects:

$$\boldsymbol{W} = \boldsymbol{W}^{ie} \tag{5.63}$$

With small strains, spatial derivatives are approximately equal in the initial and current configurations, and the rate-of-deformation is identified as the strain rate, which can be calculated with simple time derivatives of the small strain tensor:

$$\dot{\boldsymbol{\varepsilon}} = \dot{\boldsymbol{\varepsilon}}^{th} + \dot{\boldsymbol{\varepsilon}}^{el} + \dot{\boldsymbol{\varepsilon}}^{ie} \tag{5.64}$$

where $\dot{\boldsymbol{\varepsilon}}$, $\dot{\boldsymbol{\varepsilon}}^{th}$, $\dot{\boldsymbol{\varepsilon}}^{el}$, and $\dot{\boldsymbol{\varepsilon}}^{ie}$ are the total, thermal, elastic, and inelastic strain rate tensors, respectively. According to Hooke's Law, the stress is proportional to the elastic strain via the fourth-order stiffness tensor $\mathbf{D}$:

$$\boldsymbol{\sigma} = \mathbf{D} : \boldsymbol{\varepsilon}^{el} \tag{5.65}$$

For isotropic linear-elastic materials, a suitable model for most metals under small strains, the stiffness tensor is calculated by:

$$\mathbf{D} = 2\mu\mathbf{I} + \left(K - \frac{2}{3}\mu \right) \boldsymbol{I} \otimes \boldsymbol{I} \tag{5.66}$$

where μ is Lamé's second constant, also known as the shear modulus, K is the bulk modulus, and $\mathbf{I}$ is the fourth-order identity tensor. The shear and bulk moduli are in general functions of temperature, so the time derivative of the Cauchy stress tensor is:

$$\dot{\boldsymbol{\sigma}} = \mathbf{D} : \dot{\boldsymbol{\varepsilon}}^{el} + \dot{\mathbf{D}} : \boldsymbol{\varepsilon}^{el} = \mathbf{D} : \dot{\boldsymbol{\varepsilon}}^{el} + \frac{\partial T}{\partial t} \left(\frac{\partial \mathbf{D}}{\partial T} : \boldsymbol{\varepsilon}^{el} \right) \tag{5.67}$$

In this work, the effect of the temperature dependence of the stiffness tensor is neglected for the sake of simplicity, and improving this simplification is left for future work. Solving Equation (5.64) for the elastic strain rate then gives:

$$\dot{\boldsymbol{\sigma}} = \mathbf{D} : \left(\dot{\boldsymbol{\varepsilon}} - \dot{\boldsymbol{\varepsilon}}^{th} - \dot{\boldsymbol{\varepsilon}}^{ie} \right) \tag{5.68}$$

The equivalent inelastic strain rate $\dot{\bar{\varepsilon}}^{ie}$ for the steel grades considered here is assumed to be a function of temperature T, equivalent inelastic strain $\bar{\varepsilon}^{ie}$, equivalent stress $\bar{\sigma}$, and carbon composition C, as discussed later. The equivalent strain and stress are calculated according to:

$$\bar{\varepsilon}^{ie} = \sqrt{\frac{2}{3} \boldsymbol{\varepsilon}^{ie} : \boldsymbol{\varepsilon}^{ie}} \tag{5.69}$$

$$\bar{\sigma} = \sqrt{\frac{3}{2} \boldsymbol{\sigma} : \boldsymbol{\sigma}} \tag{5.70}$$

The solidifying steel is assumed to harden isotropically, and is treated with standard *J2*-plasticity theory (defined by the von Mises yield surface and normality hypothesis with the Prandtl-Reuss

flow rule) [25]. The inelastic strain rate tensor is thus recovered from the equivalent inelastic strain rate by:

$$\dot{\boldsymbol{\varepsilon}}^{ie} = \frac{3}{2}\frac{\dot{\bar{\varepsilon}}^{ie}}{\bar{\sigma}}\boldsymbol{\sigma}' \tag{5.71}$$

where $\boldsymbol{\sigma}'$ is the deviatoric Cauchy stress tensor, calculated by:

$$\boldsymbol{\sigma}' = \boldsymbol{\sigma} - \frac{1}{3}\mathrm{tr}(\boldsymbol{\sigma})\boldsymbol{I} \tag{5.72}$$

and $\mathrm{tr}(\boldsymbol{\sigma})$ is the trace of the Cauchy stress tensor. In this work, the stress and strain increments are obtained by solving a pair of coupled ordinary differential equations (valid for isotropically hardening materials) in terms of the equivalent stress and strains [26]:

$$\bar{\sigma}^{t+\Delta t} = \left(\bar{\sigma}^{*}\right)^{t+\Delta t} - 3\mu^{t+\Delta t}\dot{\bar{\varepsilon}}^{ie}\left(T^{t+\Delta t}, \bar{\sigma}^{t+\Delta t}, \left(\bar{\varepsilon}^{ie}\right)^{t+\Delta t}, C\right)\Delta t \tag{5.73}$$

$$\left(\bar{\varepsilon}^{ie}\right)^{t+\Delta t} = \left(\bar{\varepsilon}^{ie}\right)^{t} + \dot{\bar{\varepsilon}}^{ie}\left(T^{t+\Delta t}, \bar{\sigma}^{t+\Delta t}, \left(\bar{\varepsilon}^{ie}\right)^{t+\Delta t}, C\right)\Delta t \tag{5.74}$$

where $\left(\bar{\sigma}^{*}\right)^{t+\Delta t}$ is the effective elastic predictor stress that is calculated assuming that the entire strain increment was elastic. The solution of this pair of equations uses the methodology outlined in the work of Koric and Thomas [17]. This approach helps the iterative solution process make better guesses for the solution with larger time steps. This gives better overall computational efficiency than alterative approaches, including the built-in method in ABAQUS, which take more time steps of smaller size. The inelastic strain increment is calculated by:

$$\Delta\bar{\varepsilon}^{ie} = \dot{\bar{\varepsilon}}^{ie}\Delta t \tag{5.75}$$

The elastic strain increment is calculated by subtracting the inelastic strain increment from the total strain increment, which completes the definition of the material response to loading.

5.3. Mechanical Material Properties

The mechanical governing equations (continuum or finite-element) require the specification of thermophysical properties, including the coefficient of thermal expansion and elastic modulus, and the specification of a constitutive relationship between inelastic strain rate and stress. These properties in real materials exhibit a dependence upon temperature, which must be known accurately for realistic simulations. The phase fractions are calculated as described in Section 4.3.1 for the grade described in Table 4.1.

5.3.1. Coefficient of Thermal Expansion

The coefficient of thermal expansion is calculated from the temperature-dependent density with Equation (5.41), so it follows that a model of the density is necessary. Harste [8] fit equations to several measurements of density across a wide range of temperatures:

$$\rho_\ell = 7965.98 - 0.618T \tag{5.76}$$

$$\rho_\delta = 8010.71 - 0.4724T \tag{5.77}$$

$$\rho_\gamma = 8105.91 - 0.5091T \tag{5.78}$$

$$\rho_\alpha = 7880.76 - 0.3244T - 27.461 \cdot 10^{-6} T^2 \tag{5.79}$$

Instead of the Harste model for the liquid steel, in this work the empirical model of Jimbo and Cramb [12] is used, which is dependent upon both temperature and composition:

$$\rho_\ell = (7100 - 73.2C) - (0.828 - 0.0874C)(T - 1550) \tag{5.80}$$

Note that here densities are given in kg/m³, temperatures are given in ºC, and carbon composition is given in % wt. C. In accordance with the isotropic thermal expansion that has been assumed for this work, the density mixture model assumes that the mass of a control volume is the sum of the mass of its constituents:

$$\rho_{mix} = g_\ell \rho_\ell + g_\delta \rho_\delta + g_\gamma \rho_\gamma + g_\alpha \rho_\alpha \tag{5.81}$$

for volume fractions g_i. However, it is more convenient to use, at the cost of only a small error, to use the mass fractions f_i of each phase in the mixture rule for mass density:

$$\rho_{mix} = f_\ell \rho_\ell + f_\delta \rho_\delta + f_\gamma \rho_\gamma + f_\alpha \rho_\alpha \tag{5.82}$$

Figure 5.2 shows the temperature-dependent density, and the corresponding thermal expansion coefficient is given in Figure 5.3. The reference temperature is taken as the solidus temperature.

5.3.2. Elastic Constants

Many researchers have measured the elastic modulus of high-temperature steels, but the model adopted here is based on the tensile test measurements of Mizukami *et al*. [28], and Poisson's ratio is taken as a constant ν = 0.3. At elevated temperatures, the usual method of determining the elastic constants by dividing stress by the strain in a tensile tests will underpredict the values of the elastic constants because of increased creep in the tensile

specimen. Ultrasonic methods have been developed to calculate the elastic constants by measuring vibration frequencies of the specimen at high temperatures, and then calculating the elastic constants based on the wave speed of the solid material. The ultrasonic methods are more accurate at high temperatures, but since the creation of the constitutive models used in this work [19,40] also used the Mizukami model, so also must the finite element models used here to recreate the intended behavior of the constitutive models. The data of Mizukami *et al.* is plotted in Figure 5.4, with the data points inset in the graph. The value of the elastic modulus is assumed to fall to 14 GPa at the solidus temperature and then fall again to 10 GPa at and above the liquidus temperature [17,24], and for temperatures between the solidus temperature and the highest data point of Mizukami *et al.*, the elastic modulus is linearly interpolated.

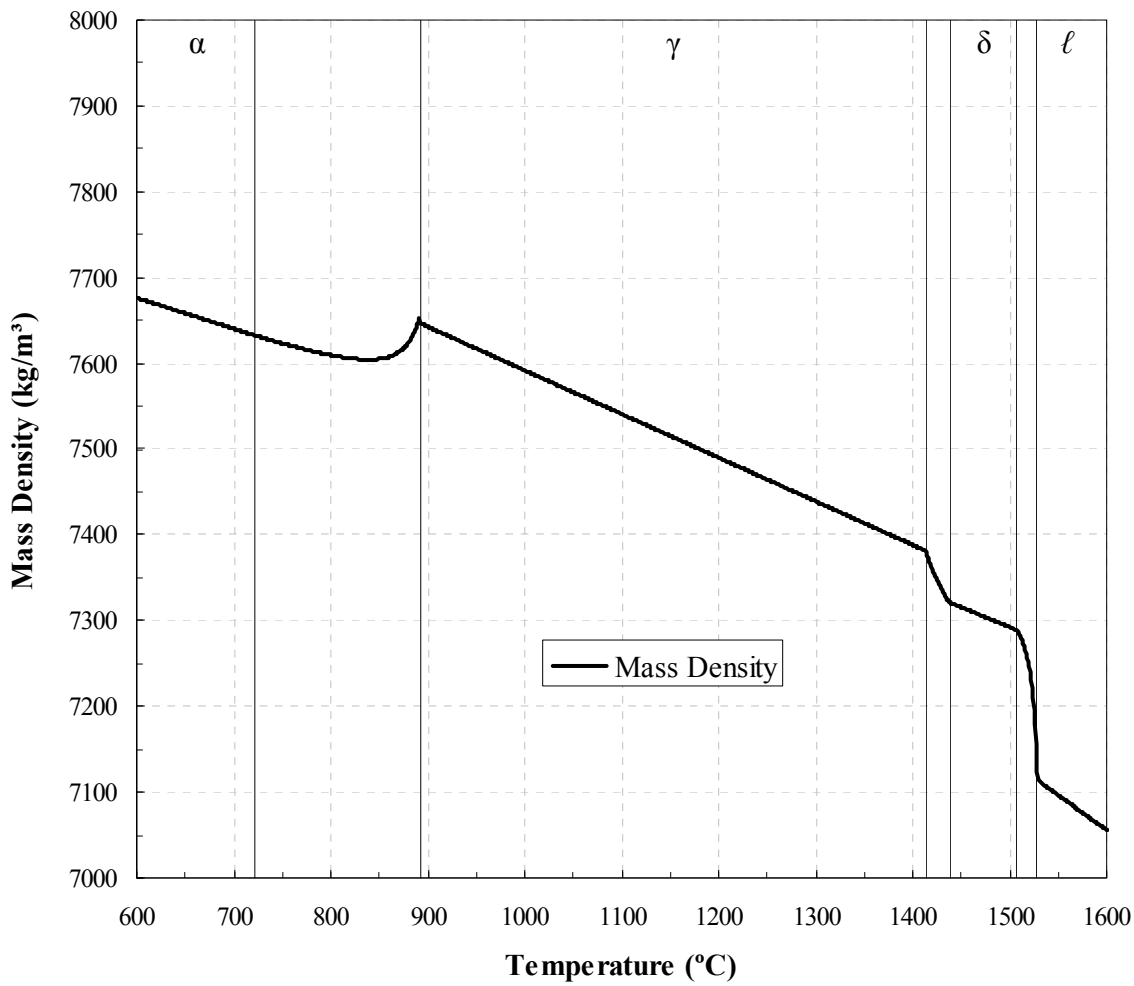

Figure 5.2. Density of 0.045 % wt. C Steel

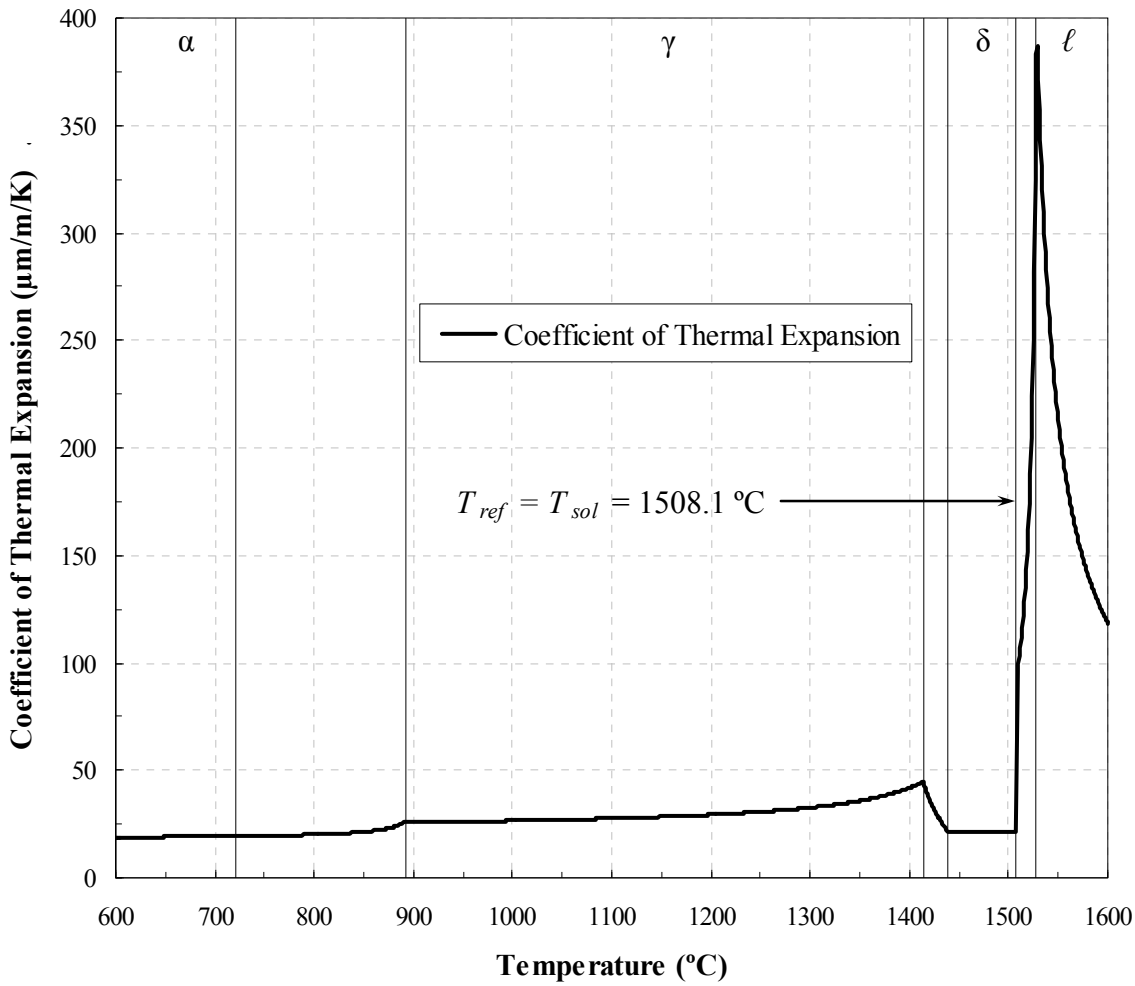

Figure 5.3. Coefficient of Thermal Expansion of 0.045 % wt. C Steel

5.3.3. Constitutive Behavior

The constitutive model that describes the relationship between stress and strain is likely the most important aspect of modeling the high-temperature behavior of solidifying steel. At elevated temperatures, the phenomenon known as creep dominates the mechanical response of most metals. A creep test is performed by measuring the increasing deformation of the solid over time while under a constant load, and several types and mechanisms of creep have been observed. The strength of delta ferrite is nearly a full order of magnitude less than austenite, so it is necessary to include separate models for each phase to correctly model the material behavior. For the current work, the constitutive models adopted include that of Zhu [40] for delta ferrite and that of Kozlowski (model III) [19] for austenite. The Kozlowski model III is given as:

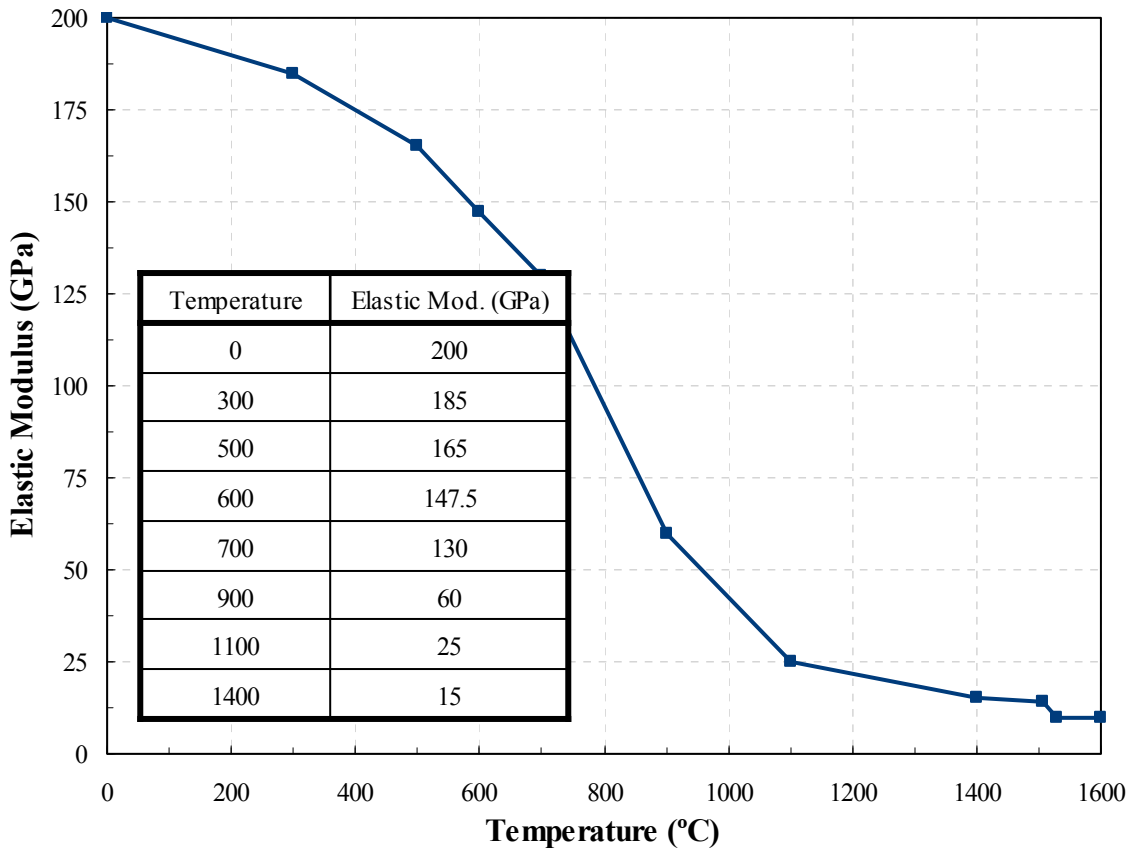

Temperature	Elastic Mod. (GPa)
0	200
300	185
500	165
600	147.5
700	130
900	60
1100	25
1400	15

Figure 5.4. Elastic Modulus of Steel

$$\dot{\bar{\varepsilon}}^{ie} = f_{\gamma C}\left[\bar{\sigma} - f_1\bar{\varepsilon}^{ie}\left|\bar{\varepsilon}^{ie}\right|^{f_2-1}\right]^{f_3}\exp\left(-\frac{Q}{\bar{R}T}\right) \tag{5.83}$$

$$f_1 = 130.5 - 5.128\cdot 10^{-3}T \tag{5.84}$$

$$f_2 = -0.6289 + 1.114\cdot 10^{-3}T \tag{5.85}$$

$$f_3 = 8.132 - 1.54\cdot 10^{-3}T \tag{5.86}$$

$$f_{\gamma C} = 10^3\cdot\left(46.55 + 71.4\cdot C + 120.0\cdot C^2\right) \tag{5.87}$$

where f_1, f_2, f_3 are temperature-dependent parameters, $f_{\gamma C}$ is a composition-dependent parameter, Q = 371.24 J/mol is the molar Zener-Hollomon parameter activation energy, and $\bar{R}$ = 8.314 J/(mol·K) is the gas constant. The Zhu model is given as:

$$\dot{\bar{\varepsilon}}^{ie} = 0.1\left|\frac{\bar{\sigma}}{(T/300)^{-5.52}\left(1+1000\bar{\varepsilon}^{ie}\right)^m f_{\delta C}}\right|^{(1/n)} \tag{5.88}$$

$$m = 0.3495 - 94.156 \cdot 10^{-6} T \tag{5.89}$$

$$n = -0.06166 + 0.1617 \cdot 10^{-3} T \tag{5.90}$$

$$f_{\delta C} = 13.678 \cdot 10^{3} C^{-0.0556} \tag{5.91}$$

where m and n are temperature-dependent parameters and $f_{\delta C}$ is a composition-dependent parameter. Both models give strain rates in s^{-1} for temperatures in K, stress in MPa, carbon composition in % wt. C, and strains in raw values (not percent). Figure 5.5 shows the response of the steel used in this work in a simple tension test with $\dot{\varepsilon} = 10^{-4}\ s^{-1}$ at $T = 1400\ ^{\circ}C$, a temperature at which both delta ferrite and austenite are present.

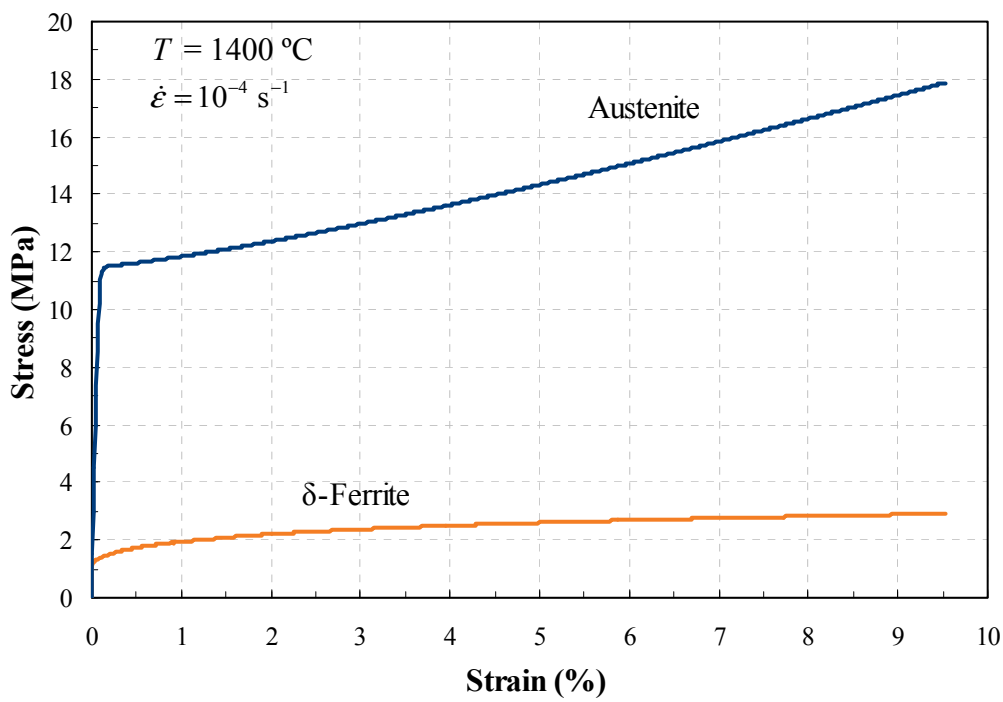

Figure 5.5. Constitutive Response of 0.045 % wt. C Steel

Over the applicable temperature ranges, the austenite strain rate increases roughly in proportion with σ^6 and ε^4 while the delta ferrite strain rate increases with σ^5 and ε^1, so the phases are both extremely sensitive to stress. However, the austenite is much more sensitive to the current inelastic strain than the delta ferrite. Both models are clearly very nonlinear and require either very small time step sizes or intelligent guessing during the iterative solution procedure, where the latter is adopted in this work after Koric and Thomas [17]. During the delta-ferrite-to-austenite phase change, the delta-ferrite model is used if the mass fraction of delta

ferrite is over 10%, where the assumption is that the softer material dominates the net mechanical behavior. Improving upon this mixture law is left for future work.

A liquid is material that deforms continuously under an applied shear loading. However, in the context of a solid mechanics numerical method this will tend to cause problems with the solution process, and an artificial shear stiffness is given to the liquid material to avoid numerical instability. The "liquid" is thus modeled with a small elastic modulus and small yield stress. Previous researchers have modeled the inelastic behavior as a solid with extremely high creep-rate [24] or as a perfectly-plastic solid [17]. The latter approach is adopted here, with a yield stress of 10 kPa, to avoid convergence problems within ABAQUS, and this "liquid" behavior is applied any time the mass fraction of the liquid in a control volume is greater than zero.

5.4. Model Verification with Analytical Solution

Verification of the finite-element thermal-mechanical model formulation is performed by comparing with the analytical solution of Weiner and Boley [37], which considers a solidifying semi-infinite plate constrained against bending with temperatures in the solid material described by Equation (4.65). The material is assumed to exhibit elastic-perfectly-plastic behavior, with a constant elastic modulus and a yield stress that decreases with temperature to zero in the liquid:

$$\sigma_Y\left(T\right)=\sigma_{Y,wall}-\left(\frac{T-T_{wall}}{T_m-T_{wall}}\right)\sigma_{Y,wall} \tag{5.92}$$

where $\sigma_{Y,wall}$ is the yield stress at the wall temperature and $\sigma_Y\left(T\right)$ is the yield stress at temperature T. Without derivation, the solution to the stress problem is given below. The material shifts from a plastic region on the surface, to an elastic region in the center of the solidified material, to a plastic region just below the solidification front. The calculation of the distance of these two transition points from the surface require the solution of a pair of nonlinear equations for the variables ζ_1 and ζ_2:

$$\begin{aligned}&2\left(1-\psi\right)\zeta_1\exp\left(-\zeta_1^2\right)\left(\zeta_1-\zeta_2\right)=\\&\quad\left(1+\psi\right)\exp\left(-\zeta_2^2\right)-\left(1-\psi\right)\exp\left(-\zeta_1^2\right)-\psi\left(\exp\left(-\phi^2\right)+1\right)\end{aligned} \tag{5.93}$$

$$\begin{aligned}&2\left(1-\psi\right)\zeta_1\exp\left(-\zeta_1^2\right)\ln\left(\zeta_1/\zeta_2\right)\Big/\sqrt{\pi}=\\&\quad\left(1-\psi\right)\mathrm{erf}\left(\zeta_1\right)-\left(1+\psi\right)\mathrm{erf}\left(\zeta_2\right)+2\psi\,\mathrm{erf}\left(\phi\right)\end{aligned} \tag{5.94}$$

where ϕ is the length-time proportionality constant from the thermal problem calculated from Equation (4.73), and ψ is a scaling constant calculated from:

$$\psi = \frac{(1-\nu)\sigma_{Y,wall}}{\alpha_E E_{sol}(T_m - T_w)} \tag{5.95}$$

The depth below the surface of the plastic-elastic transition ξ_1 is:

$$\xi_1 = \min(\zeta_1, \zeta_2)\delta(t) \tag{5.96}$$

where $\delta(t)$ is the shell thickness as a function of time, calculated from Equation (4.63).

Similarly, the depth below the surface of the elastic-plastic transition ξ_2 is:

$$\xi_2 = \max(\zeta_1, \zeta_2)\delta(t) \tag{5.97}$$

The stress in the surface plastic region is then:

$$\sigma = \sigma_{Y,wall}\left(\frac{\operatorname{erf}\left(x/\sqrt{4\alpha_T t}\right)}{\operatorname{erf}(\phi)} - 1\right) \qquad \text{for } 0 \le x \le \xi_1 \tag{5.98}$$

The stress in the middle elastic region is:

$$\sigma = \frac{\sigma_{Y,wall}}{\psi}\left(\begin{array}{c}(1-\psi)\left(\operatorname{erf}(\zeta_1) - \frac{2\zeta_1}{\sqrt{\pi}}\exp\left(-\zeta_1^2\right)\ln\left(\frac{\zeta_1\sqrt{4\alpha_T t}}{x}\right)\right) + \\ \psi\operatorname{erf}(\phi) - \operatorname{erf}\left(x/\sqrt{4\alpha_T t}\right)\end{array}\right) \qquad \text{for } \xi_1 \le x \le \xi_2 \tag{5.99}$$

The stress in the subsurface plastic region, closest to the solidification front, is given by:

$$\sigma = \sigma_{Y,wall}\left(1 - \frac{\operatorname{erf}\left(x/\sqrt{4\alpha_T t}\right)}{\operatorname{erf}(\phi)}\right) \qquad \text{for } \xi_2 \le x \le \delta(t) \tag{5.100}$$

Finally, the stress in the liquid is zero:

$$\sigma = 0 \qquad \text{for } \delta(t) \le x < \infty \tag{5.101}$$

This completes the definition of the elastic-perfectly-plastic stress solution for the solidification of an infinite plate.

The surface of the shell quenches immediately the thermal contraction tends to cause the body to shrink locally. The surface shrinks stress-free in the first few moments of solidification owing to the lack of constraint imposed by the neighboring liquid material. The material closer to the solidification front, then solidifies and tends to shrink. As time progresses, these internal

points point will cool more and thus will shrink more, relative to the surface region which will stay relatively constant. This tends to generate compression at the surface. The constraint against bending requires that the net out-of-plane normal stresses are zero, which results in subsurface tension to balance the surface compression, giving the characteristic curves shown below.

In addition to the properties and parameters provided in Table 4.2 for the thermal stress problem, the required parameters for the stress solution are summarized in Table 5.1. The numerical solution is accommodated by decreasing the yield stress to a small value rather than zero. The domain and boundary conditions are illustrated in Figure 5.6. The domain and mesh used is identical to the 300-element, 602-node mesh used for the heat transfer verification, except using the standard CPEG4 generalized plane strain elements (with no extra features) in ABAQUS [1]. The constraint against bending in the out-of-plane directions is treated by defining a reference node with constrained rotational degrees of freedom, forcing c_x and c_y in Equation (5.22) to zero. The constraint against bending in analysis plane is treated by fixing the perpendicular displacements of the top edge, and constraining the perpendicular displacement of the bottom edge to be identical, thus enforcing a second generalized plane-strain condition.

Table 5.1. Properties Used in Solidification Stress Test Problem

Property	Symbol	Value	Units
Coefficient of Thermal Expansion	α_T	$20 \cdot 10^{-6}$	(m/m)/K
Poisson's Ratio	ν	0.3	--
Elastic Modulus in Solid	E_{sol}	40.0	GPa
Elastic Modulus in Liquid	E_{liq}	14.0	GPa
Yield Stress at Wall Temperature	$\sigma_{Y,wall}$	20.0	MPa
Yield Stress at Solidus Temperature	$\sigma_{Y,sol}$	35.0	kPa

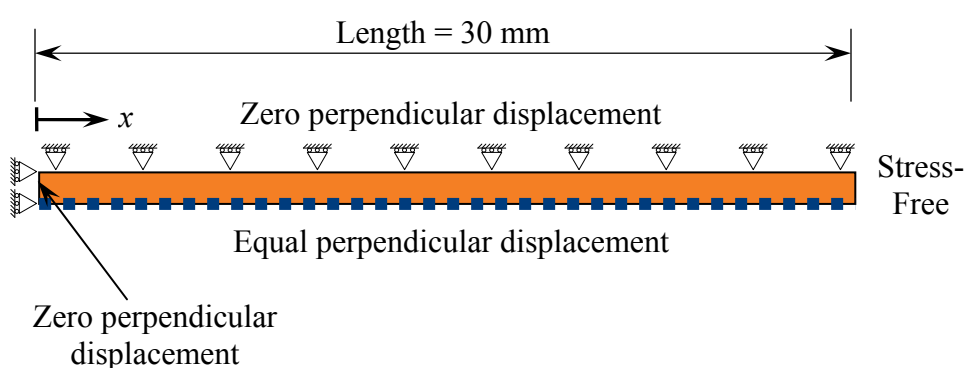

Figure 5.6. Thermal-Stress Test Problem Domain and Boundary Conditions

Figures 5.7 and 5.8 show a comparison of the analytical and numerical solutions of the test problem for several times and several points in space, respectively. The stress components plotted are in the analysis plane, perpendicular to the longer sides of the domain. The numerical solution matches the analytical solution for the most part, with the exceptions being around the solidification front and in regions of high spatial gradient of stress. The time history plots illustrate this better with the transition from elasticity to plasticity. A convergence study of this test problem has been performed elsewhere [24,40]. This study showed that a mesh like the one in this study with 0.1-mm elements using a time step of 0.01 seconds lowers the maximum errors to about 1% or less.

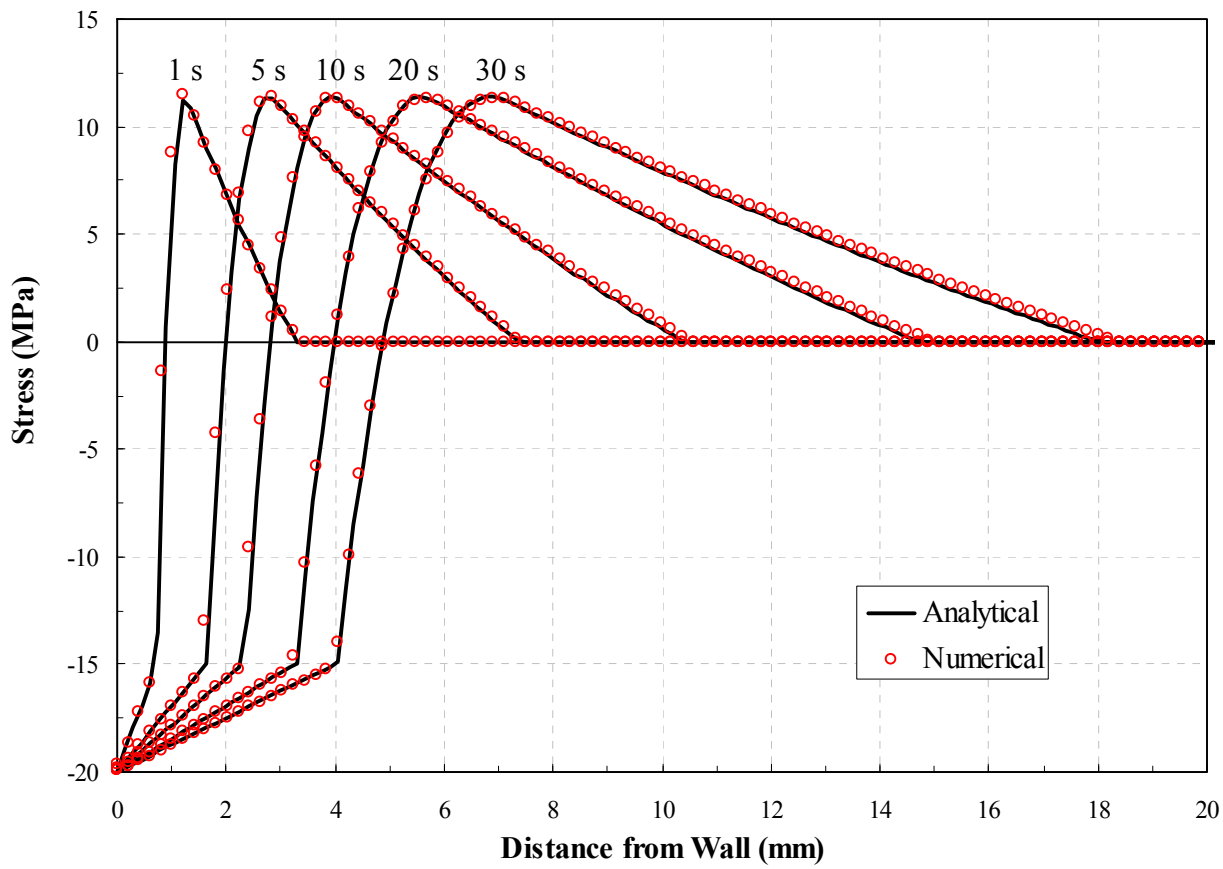

Figure 5.7. Solidification Test Problem Stress Verification in Space

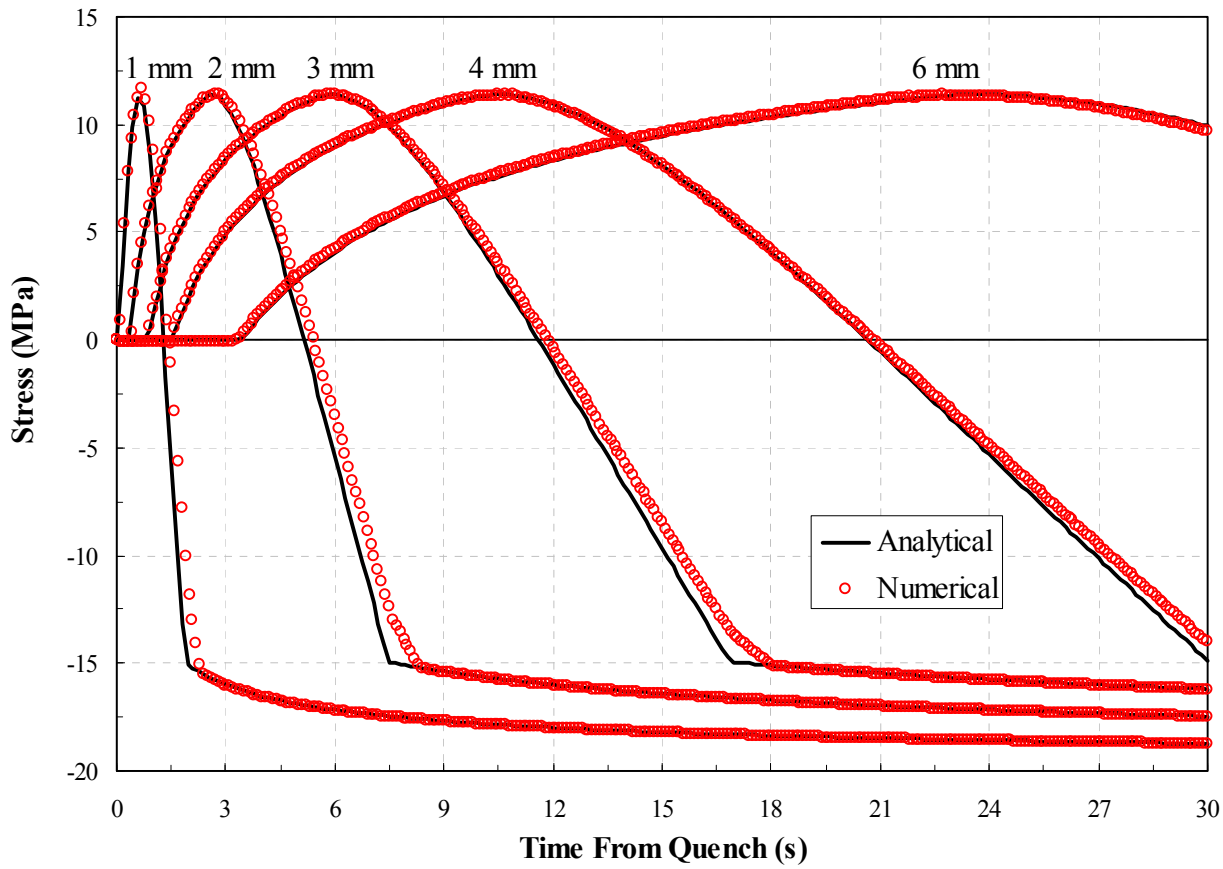

Figure 5.8. Solidification Test Problem Stress Verification in Time

5.5. Shell Model Setup

A finite element model of the solidifying shell was constructed to investigate the effect of the funnel mold geometry on the mechanical behavior of the shell. The shell domain is identical to that of the thermal problem described in Chapter 4, including the shape and size, two-fold symmetry, and the assumption of a two-dimensional slice that moves at the casting speed down the mold, as discussed in Sections 4.2. and 5.2. The material properties are defined as discussed above for a 0.045 %wt. C steel. The temperature field at any point in time is recovered from the results of the thermal analysis.

The analysis domain and boundary conditions are shown schematically in Figure 5.9. The contacting surfaces between the shell and the mold are treated with a "softened" exponential pressure-penetration algorithm within ABAQUS [1], and the coefficient of friction is taken as $\mu_f = 0.11$ after measurements of mold slag on copper [27]. The first 5 mm of the mold is modeled so that contact surfaces may be defined to enforce the changing funnel shape with

distance down the mold. The mold is the stiffer material, so it is defined as the master contacting surface in ABAQUS. All nodes on the mold are given a displacement boundary condition (except for the appropriate symmetry planes) that reproduce the shape of the funnel as seen by the traveling analysis plane. The depth of the analysis plane below the top of the mold z is calculated from the time using Equation (4.16), and then the applied displacement is calculated from the appropriate function s in Chapter 2 that describes the hot face of the mold:

$$u_y = s(x,z) - s(x,z_m) \tag{5.102}$$

This displacement function for Mold A (*cf.* Chapter 2) is plotted in Figure 5.10.

The symmetry planes have the appropriate zero normal displacement boundary condition. The analysis domain does not include the entire quadrant of the two-dimensional slice plane; the region closest to the center of the plane will always be in the liquid state while the analysis plane is in the mold, so inclusion in this analysis is not necessary and would only serve to increase the computational cost and cause numerical problems. The always-liquid inner surface is modeled as stress-free in this work, which allows this region to shrink as it would naturally. The ferrostatic pressure is applied as a uniformly-distributed load on the shell-mold interface, pulling the stiff solid shell outward, rather than pushing on the soft solidification front, which is almost equivalent, but much less stable. The magnitude of the ferrostatic pressure p is calculated according to:

$$p = \rho_{liq} g z \tag{5.103}$$

where g is the acceleration due to gravity and ρ_{liq} is the density of the liquid steel at the liquidus temperature. Furthermore, as illustrated in Figure 5.11, the application of the load is delayed by about one second in order to allow the outermost row of elements to solidify to improve convergence at early times.

The mesh used in the mechanical analysis is identical to that used for the appropriate thermal analysis for a given funnel geometry, except that the element type are all generalized plane strain, four-node, "fully integrated" (2×2 Gaussian quadrature) bilinear quadrilateral finite elements like those used for the stress validation problem. Node and element counts are given in the discussion of results.

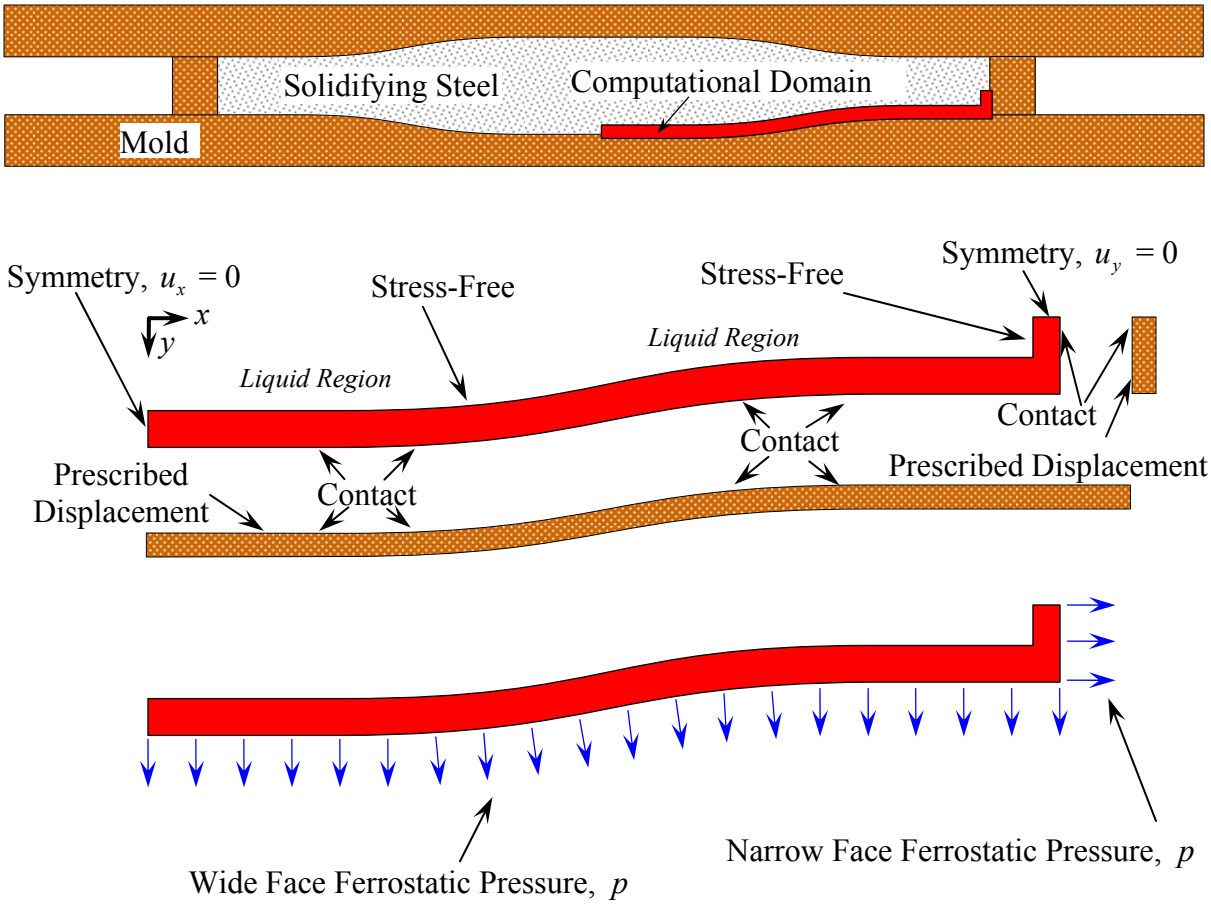

Figure 5.9. Schematic of Computational Domain and Boundary Conditions

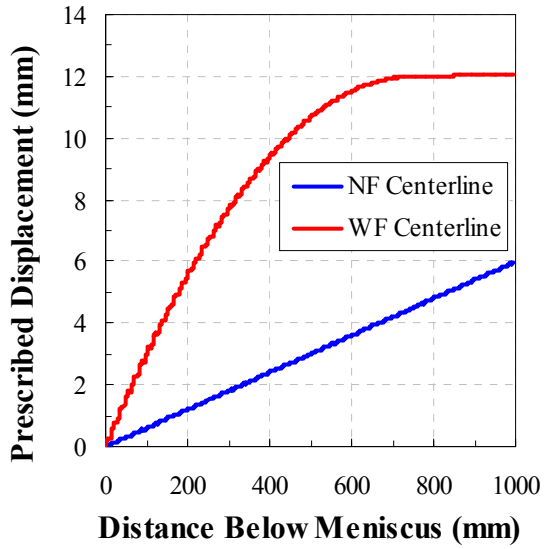

Figure 5.10. Mold Displacement Functions

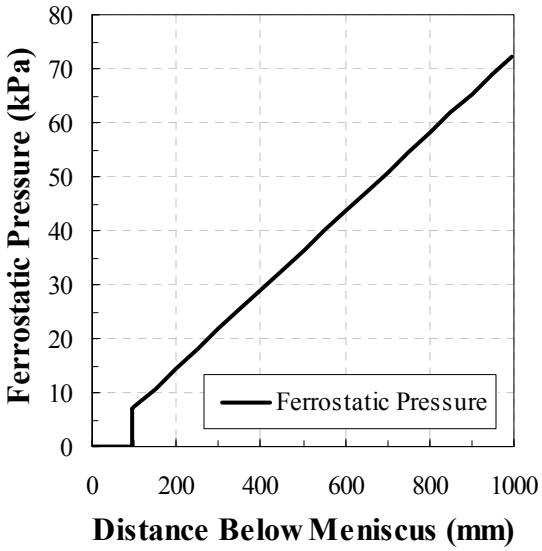

Figure 5.11. Ferrostatic Pressure Function

5.6. Shell Model Results

The results of the mechanical model investigation of the solidifying shell are presented below, with consideration according to the through-thickness and circumferential directions. Stress and strain components reported are always in the direction parallel to the surface of the mold, *i.e.*, perpendicular to the heat flow direction.

5.6.1. Through-Thickness Direction

The stress profiles through the thickness of the shell at increasing times are shown in Figure 5.12. The stress profile at mold exit with the different phase regions labeled are given in Figure 5.13. The stress histories at a few points beneath the surface are shown in Figure 5.14. Except for the first 0.5 seconds, the surface is always in compression, and the subsurface regions are always in tension, resulting in zero net stress through the thickness of the shell. The liquid region always has almost zero stress (equal to the small yield stress defined in the liquid region), and the delta ferrite region unable to sustain much stress. A considerable load is developed in the steel once the austenite phase is formed at 10 % mass fraction delta remaining. The circumferential stress field contours in the casting direction have been reconstructed in Figure 5.15. This figure shows clearly that the compressive region at the surface grows to only about 2 mm thick within the mold. Internal cracks are most likely in weak inter-dendritic regions found outside of this region.

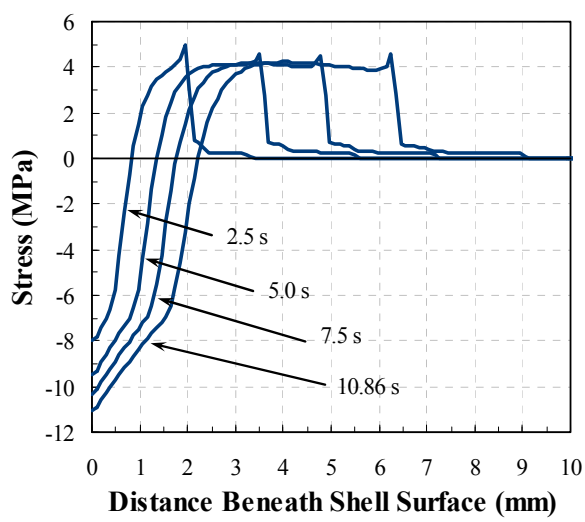

Figure 5.12. Through-Thickness Shell Stresses

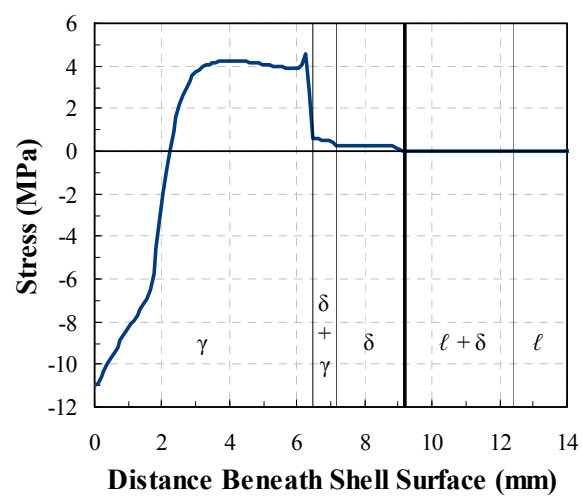

Figure 5.13. Shell Stresses with Phases Delineated

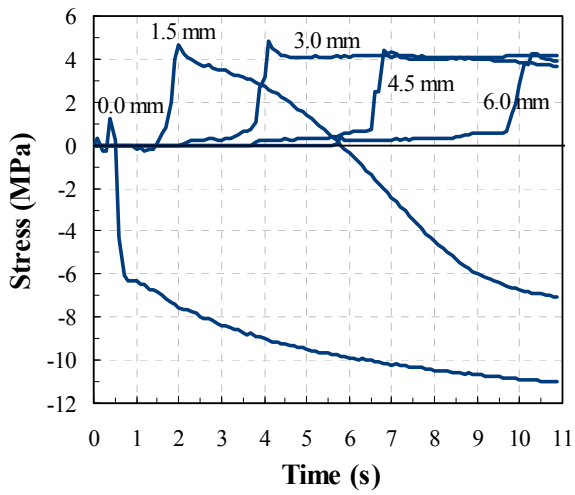

Figure 5.14. Shell Stress Histories

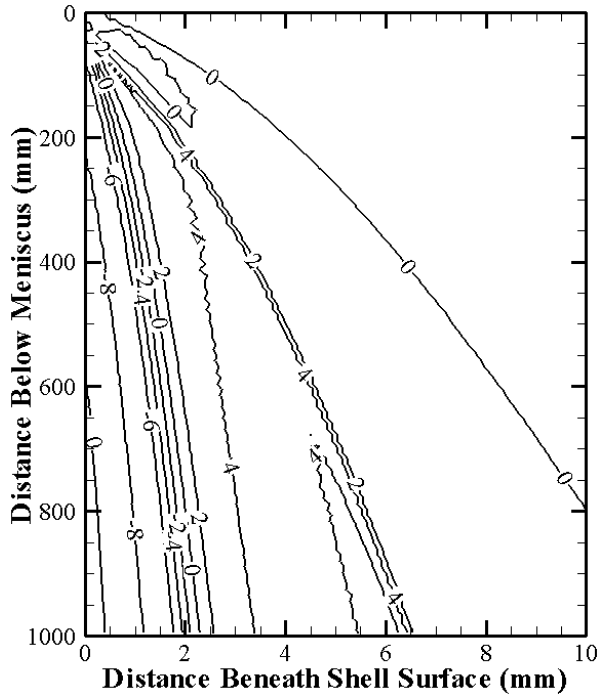

Figure 5.15. Stress Field in Casting Direction

5.6.2. Circumferential Direction

More important information for this project on funnel design can be gained by examining the variation in stress and strain around the mold perimeter. Figure 5.16 shows the stress on the surface as a function of distance from the centerline at several times for Mold A. The surface stress becomes slightly more compressive as the distance from the center increases, which is likely related to frictional effects reducing the compression imparted to the shell from excessive narrow face taper. The more striking feature is the increase in compressive stress in the "inside curve" region and the corresponding decrease in compressive stress in the "outside curve" region.

Recalling the surface temperatures in Figure 4.18, the localized increase and decrease in stress follow the respective increase and decrease in temperature. Examining the computed heat flux on the surface in the curved regions, the inside curve region of Mold A sees a 0.5 % increase in heat flux and the outside curve region sees as 0.5 % decrease in heat flux. A series of one-dimensional thermal-stress simulations (similar to the validation problems, but with the realistic properties and boundary conditions) were performed with the applied heat flux increased and decreased to determine if the change in temperature alone causes the resulting change in stress. The resulting stress in the inside curve region was 0.15 MPa more compressive than with the

nominal conditions for the duration of the simulation. Similarly, the stress in the outside curve region was 0.15 MPa less compressive than the nominal conditions. These were observed to decrease with decreasing variation of heat flux, *i.e.*, with increasing horizontal funnel radius. These deviations in stress are much smaller than the approximately 2 MPa variations observed in Figure 5.16, indicating that another effect is responsible for the observed stress profiles.

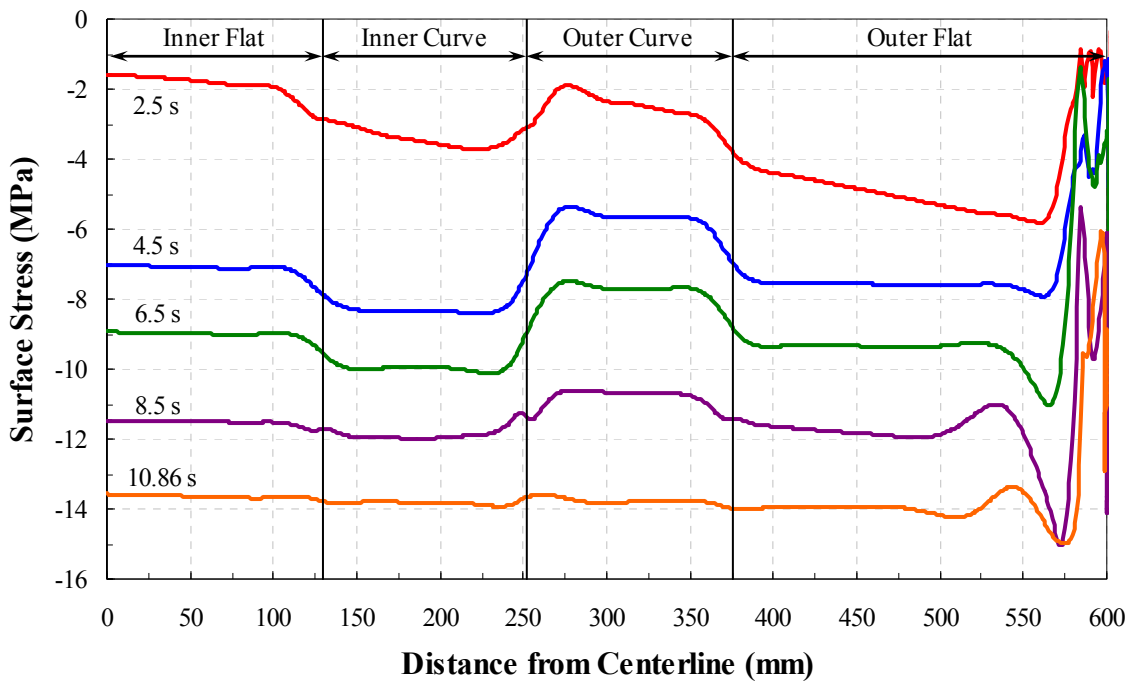

Figure 5.16. Shell Surface Circumferential Stresses at Different Times

Examining the stress on the solidification front, found by taking the maximum through-thickness stress at several points along the perimeter, reveals similar trends but occurring in the opposite direction, as shown in Figure 5.17. The combination of Figures 5.16 and Figure 5.17 indicates that the mechanical effect of the funnel mold on the solidifying shell is to induce bending behavior in the transition region. The difference between the bending effect experienced by the shell in the inside curve and outside curve regions is the "sign" of the bending effect; the magnitude of the strain is equal, though the shell surface on the inside curve is subject to compression and the shell surface in the outside curve is subject to tension. The magnitude of the internal stresses is naturally smaller, owing to the lower strength of the hotter steel there, relative to the colder and stronger surface.

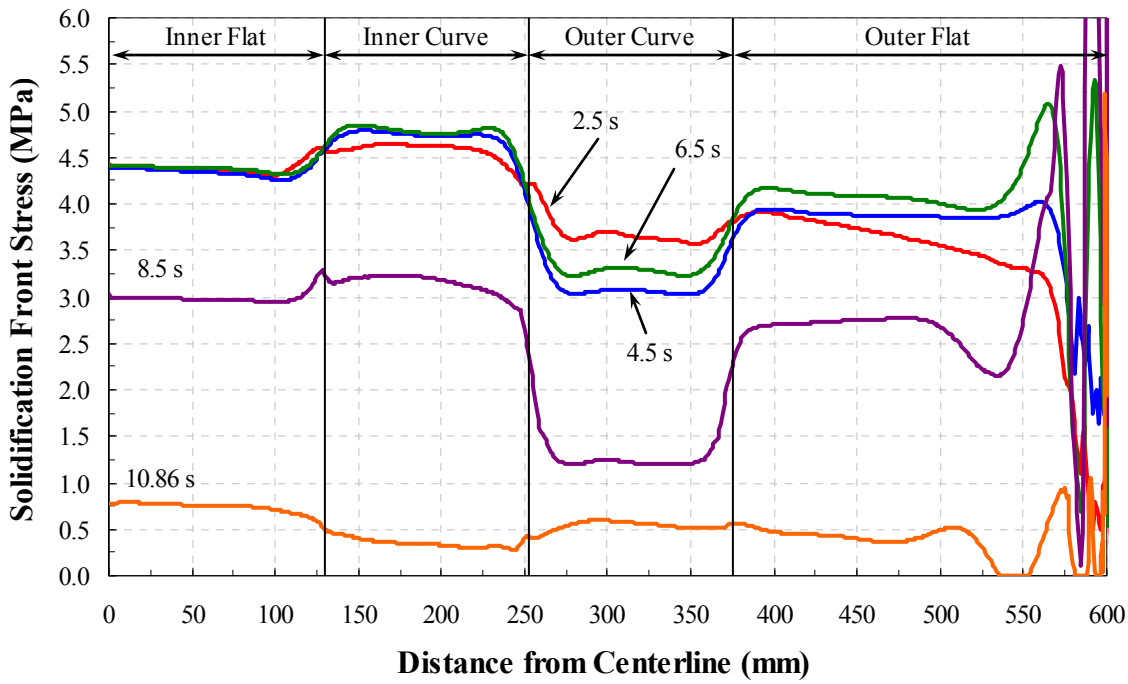

Figure 5.17. Shell Solidification Front Circumferential Stresses at Different Times

To investigate the effect of funnel geometry on these variations in the circumferential stress, a parametric study was performed with several hypothetical geometries based on the A-type design presented in Chapter 2. All cases use a mold length of 1100 mm, a funnel length of 850 mm, and a casting speed of 5.5 m/min. The geometry, model sizes, and run times, using 2 CPUs on a Dell PowerEdge 1750 Linux Cluster with Intel Xeon 3.2 GHz processors, are summarized in Table 5.2. Figures 5.18 and 5.19 show the circumferential stress profiles on the surface and solidification front for the different cases. These results are all extracted from the simulations at 500 mm below the meniscus, or halfway down the length of the mold. For the most part, the difference in stress between the flat regions and the transition regions decreases with increasing funnel width and decreasing crown, *i.e.*, the effect of the funnel geometry on the mechanical response of the shell reduces as the funnel approaches a parallel mold, similar to the effect of the geometry on the thermal behavior of the shell. The same trends are observed in the study of B-type molds. The exception to the trend is with the case with the deep crown, in which the effective taper of the funnel is so large that the narrow face causes more net compressive behavior in the shell, as discussed next. Similar to the thermal response, the trends indicate that the variation in stress is proportional to the horizontal radius, which will be discussed the next section.

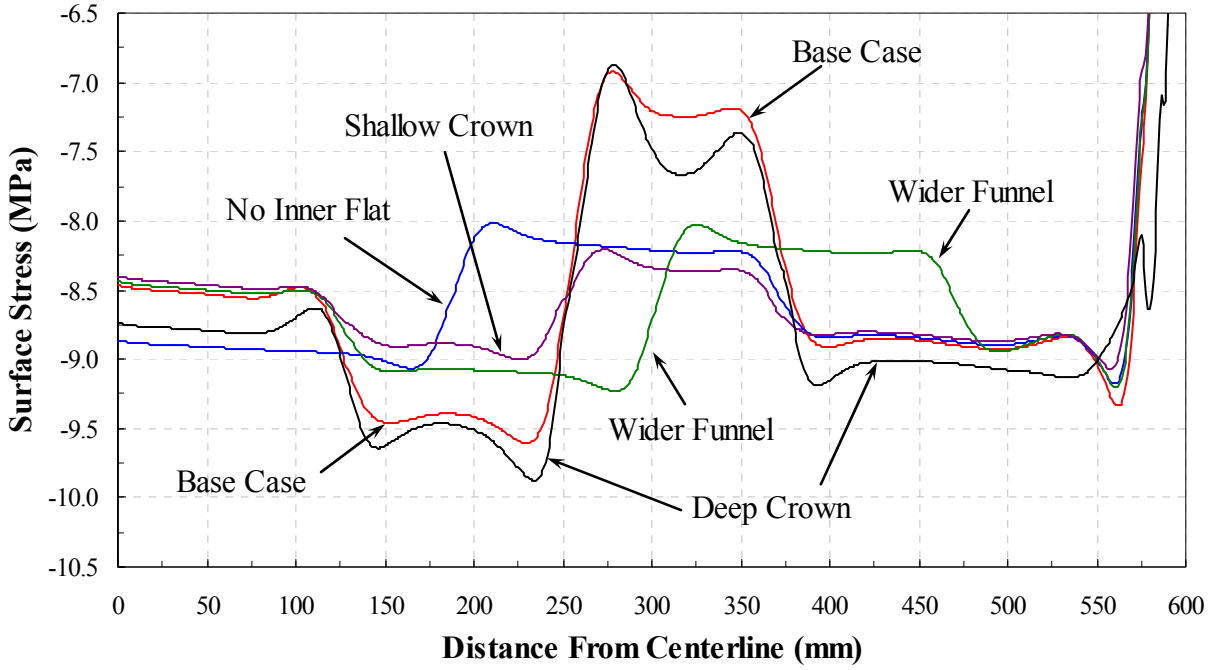

Figure 5.18. Effect of Funnel Geometry on Surface Circumferential Stress

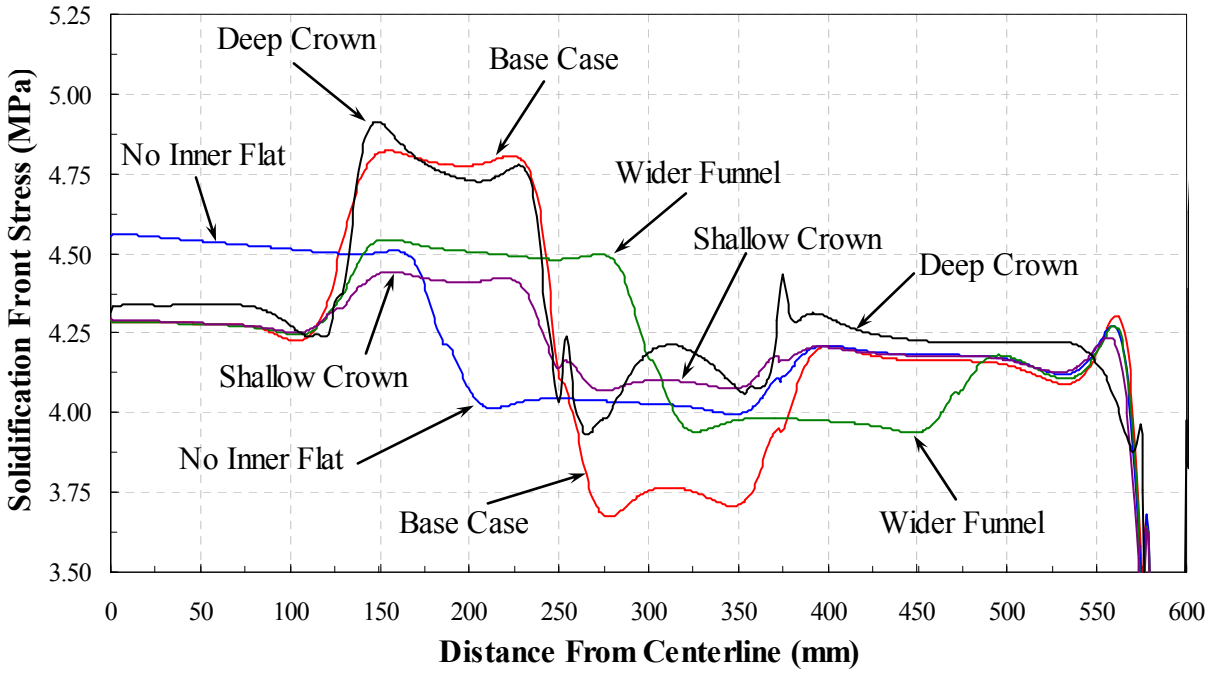

Figure 5.19. Effect of Funnel Geometry on Solidification Front Circumferential Stress

Table 5.2. Summary of Funnel Geometries Simulated for Mechanical Behavior Study

Case	Description	Funnel Geometry (mm)				Simulation Data		
		w_i	w_0	c_T	c_B	Nodes	Elements	Runtime (hr)
1	Base Case	130	375	23.4	8	34664	17258	21.0
2	No Inner Flat	0	375	23.4	8	34667	17260	22.8
3	Wider Funnel	130	475	23.4	8	34719	17286	19.8
4	Shallow Crown	130	375	13	8	34664	17258	20.3
5	Deep Crown	130	375	48	8	34664	17258	19.5

All of the above simulations were performed with the same strand width of 1200 mm, and the applied 1.0 %/m (percent per meter of perimeter per meter of effective mold length, taken as 1000 mm) linear narrow face taper based on that width is then 6 mm per side. The geometry of the funnel actually increases the total perimeter length of the slab, so changing the sizes of the funnel geometric features effectively changes the taper. This needs to be accounted for when designing taper practices to avoid the issues that arise with excessive narrow face taper, namely, squeezing the shell. For example, considering funnel geometries based on the B-type design presented in Chapter 2, crowns of 20, 30, and 40 mm account for 1.30, 3.23, and 5.92 mm of perimeter length per wide face that must be considered in the taper calculations. Including the applied 6 mm of taper from the narrow face, these molds have effective tapers of 1.1, 1.3, and 1.5 %/m, which can induce a considerable amount of compressive behavior on the solidifying shell, and thus increasing the risk for shell buckling producing longitudinal depressions, cracks, and breakouts. The extra compression is somewhat evident in the stress profiles in Figures 5.18 and 5.19, but is more clear in examining the average circumferential stress through the thickness of the shell as a function of distance from the center of the wide face, plotted in Figure 5.20 for the B-type mold with the three crown sizes mentioned above at 500 mm below the meniscus. At this particular location, the narrow face is just starting to make good contact with the shell for the 20- and 30-mm crowns, and the average stress anywhere in the shell is slightly tensile as a result of the ferrostatic pressure pulling the shell towards the narrow faces when a substantial gap is open between the shell and mold due to insufficient narrow face taper. Owing to the increased perimeter length change with the deeper crown, the shell in the 40-mm crown case is entirely under net compression, increasing the risk for buckling-related failure mechanisms, discussed later. The tendency of the average stress to become more compressive with increasing distance away from the center of the wide face is likely related to the difference in accumulated frictional

effects at different points around the perimeter of the shell, but deserves further study before any solid claims can be made.

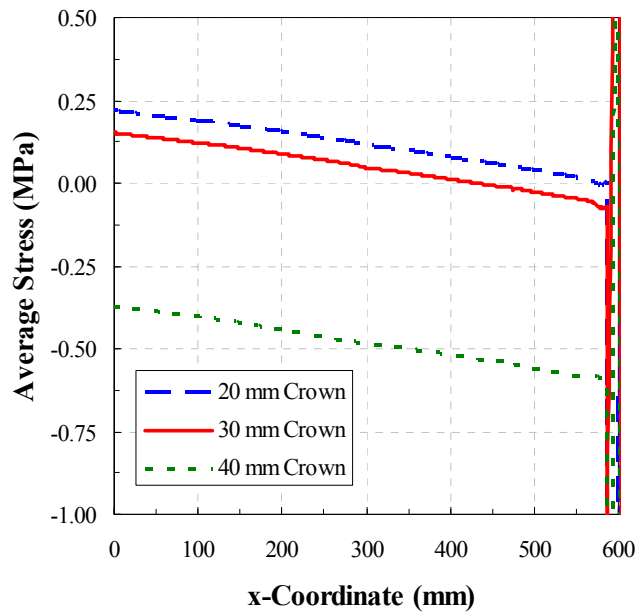

Figure 5.20. Average Circumferential Stress at 500 mm Below Meniscus

The average circumferential stress becomes more compressive with increasing distance below the meniscus, as shown in Figure 5.21, which plots the average stress at the outer curve-outer flat transition point at 475 mm away from the centerline. These plots are typical of the average stress at any point around the perimeter of the wide face (except the corners), owing to the fact that the bending mechanism has no effect on the average stress. The average stress is negligible higher in the mold with the small applied taper and high creep rates in the shell. As the narrow face squeezes the shell more with increasing distance down the mold, the average stress becomes more compressive. The wiggles in the figure are associated with the jumps in hot face position as seen by the slice domain moving through the oscillating mold. Although all three cases do end at the same average stress (because all geometries are identically flat at mold exit), it is important to note that the deeper crowns become more compressive higher in the mold when the shell is thinner and can withstand less of a buckling load. This suggests that deeper crowns might be more prone to cracks and other problems associated with longitudinal depressions.

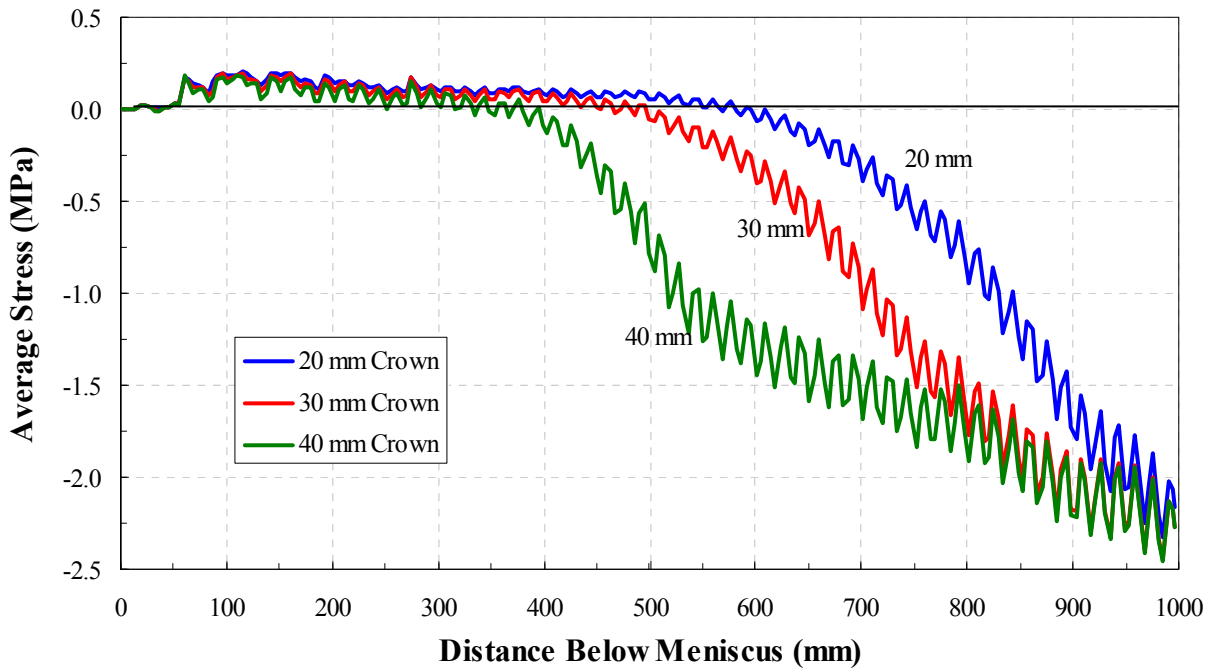

Figure 5.21. Average Circumferential Stress at 475 mm from Wide Face Centerline

5.7. Analytical Bending Model

As mentioned above, the main effect of the funnel geometry on the solidifying shell is to induce a bending mechanical response in the funnel transition region. This effect is unique to funnel molds, since although other shapes may have changing hot face profiles from taper or a casting radius, they do not change position by several centimeters as is common in funnel molds. This section will not only explain the bending mechanism in terms of elementary solid mechanics [11], but will derive a simple analytical model that can predict the strain results of the two-dimensional elastic-viscoplastic finite element models with surprising accuracy.

Consider an initially straight beam of length w_s and thickness δ in the coordinate system defined in Figure 5.22. The elementary beam theory employed here considers only one component of stress, σ_{xx}, with all others set to be zero. This beam is representative of the shell in contact with the wide face of the mold and in this case σ_{xx} is the circumferential stress in the shell, which is most important to longitudinal crack formation, discussed in the next section. The "neutral axis" of the beam must be determined as a part of this analysis, and is defined as the region of the cross section where σ_{xx} = 0, as sketched in Figure 5.23. The neutral axis experiences no change in length during bending of the beam, and is located by integrating the

stress distribution above and below the neutral axis and determining the constants to cause the resultant forces to balance:

$$\int_{A_{lower}} \sigma_{xx} dA = \int_{A_{upper}} \sigma_{xx} dA \tag{5.104}$$

For a linear-elastic material with constant elastic modulus, the typical approach is to assume that the axial stress varies linearly with the y-coordinate by some constant c_0:

$$\sigma_{xx} = c_0 y \tag{5.105}$$

This assumption results in the neutral axis and centroidal axis falling coincident upon each other. However, considering the beam as a model of the solidifying shell, the assumption of constant elastic modulus is unreasonable. As observed in Figure 4.13, the temperature through the thickness of the shell is not constant, and Figure 5.4 illustrates that the elastic modulus of the solidifying steel decreases with increasing temperature. Since the material closer to the surface is much stronger and stiffer than the material closer to the solidification front, the neutral axis will fall just a few millimeters beneath the surface, even when the shell is over a centimeter in thickness, as illustrated in Figure 5.12 for the case without bending. Thus, to simplify the analysis at hand, the neutral axis will be assumed to always lie on the surface of the solidifying shell, but the analysis will nevertheless proceed as in the general case.

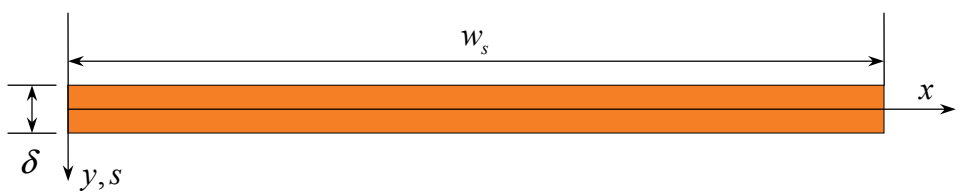

Figure 5.22. Beam Schematic and Coordinate System

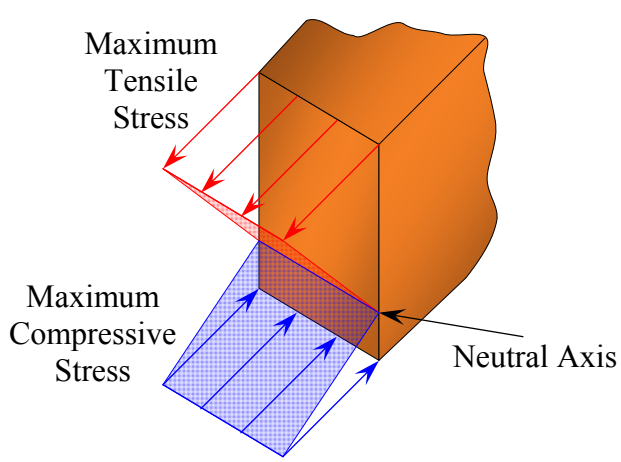

Figure 5.23. Bending Stress Profile Across Beam Section

The axial strain profile through a cross-section is determined by the local radius of curvature about which the beam is bent. Consider a beam segment of undeformed thickness Δx anywhere along the beam axis, as shown in Figure 5.24. A line segment on the neutral axis of the beam will have length Δx both before and after deformation, while a line segment at some elevation y from the neutral axis has original length Δs and deformed length $\Delta s'$ upon bending, as shown in Figure 5.25. The axial strain at the elevation y is then:

$$\varepsilon_{xx} = \lim_{\Delta x \to 0} \frac{\Delta s' - \Delta s}{\Delta s} \tag{5.106}$$

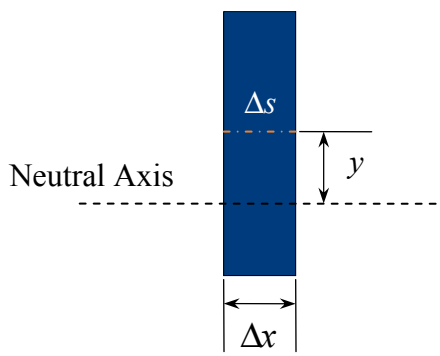

Figure 5.24. Undeformed Beam Element

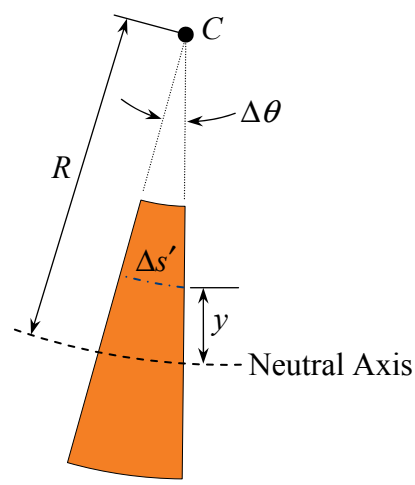

Figure 5.25. Deformed Beam Element

The elementary beam theory requires that planar cross-sections remain planar after deformation, or that no warping occurs. The beam segment considered above will then deform so that it sides rotate to form a well-defined radius of curvature R, center point C, and subtended angle $\Delta\theta$, as shown in Figure 5.25. Simple geometry gives that the original length of the line segment of interest, which is initially equal to the beam segment width Δx, is $\Delta s = R\Delta\theta$, and the deformed length is $\Delta s' = (R - y)\Delta\theta$. Substituting these lengths into the above definition of axial strain gives:

$$\varepsilon_{xx} = \lim_{\Delta\theta \to 0} \frac{(R - y)\Delta\theta - R\Delta\theta}{R\Delta\theta} \tag{5.107}$$

which simplifies, even without taking the limit, to just:

$$\varepsilon_{xx} = -\frac{y}{R} = -y\kappa \tag{5.108}$$

where here y is the distance from the neutral axis, R is the local radius of curvature, and $\kappa = 1/R$ is the curvature. This axial strain is defined only in terms of the geometry, and so can only be described as applied mechanical strain, neither elastic or inelastic. In general, the curvature of a line $s(x)$ can be calculated from:

$$\kappa = \frac{\frac{d^2 s}{dx^2}}{\left(1 + \left(\frac{ds}{dx}\right)^2\right)^{\frac{3}{2}}} \tag{5.109}$$

For the analysis at hand, the line $s(x)$ is the shape of the funnel mold hot face, but it can also be the deformed shape of the beam, which is usually recovered by assuming that the slope of the line is small, giving $\kappa = d^2 s / dx^2$, and integrating. In the case of the "tangent circles" funnel design of Chapter 2, this assumption is not necessary since the curvature is just the inverse of the horizontal funnel radius. The circumferential strain due to bending in the tangent circles design is then simply:

$$\varepsilon_{xx} = -y \begin{cases} 0 & 0 \le x \le w_i \\ -1/r_h & w_i \le x \le w_m \\ 1/r_h & w_m \le x \le w_o \\ 0 & w_o \le x \le w_s \end{cases} \tag{5.110}$$

One qualification that must be noted at this point is that the strain predicted with this equation is the strain that is developed from bending an initially straight beam into whatever configuration has the value r_h. This qualification can be overcome by calculating the strain developed in bending a straight beam of some thickness into the mold profile at the meniscus, calculating the strain developed in bending another straight beam of the same thickness into the mold profile at some position below the meniscus, and then subtracting the two values.

$$\varepsilon_{xx}(z) = \frac{y}{r_h(z_m)} - \frac{y}{r_h(z)} = y\frac{r_h(z) - r_h(z_m)}{r_h(z) r_h(z_m)} \tag{5.111}$$

Here, y is the distance from the surface of the shell, applying the result of the earlier development that the neutral axis lies on the shell surface. If anywhere the mold profile becomes

perfectly flat, *i.e.*, a parallel mold, then the infinite radius removes the second term from the subtraction. The result of this subtraction is the more important quantity when considering the behavior of the solidifying shell in a funnel mold, and is the strain developed in bending a beam originally in the shape of the mold at the meniscus into the shape of the mold at some position lower in the mold, as illustrated in Figure 5.26.

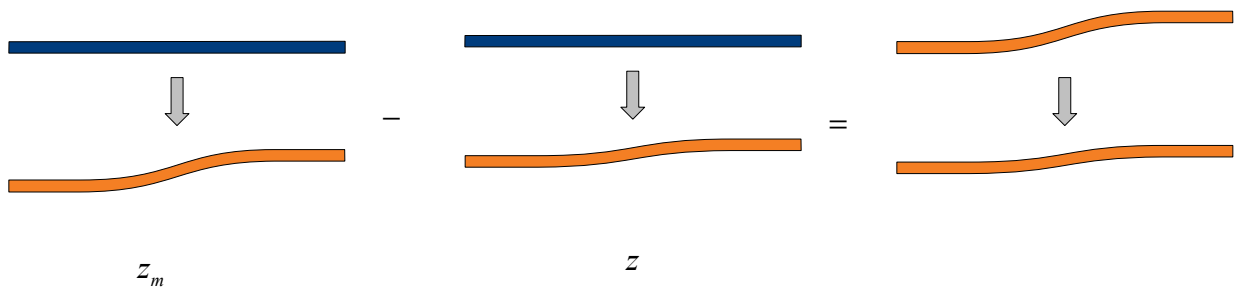

Figure 5.26. Logic of "Developing" Bending Strain Model

To evaluate the accuracy of the bending model, including the assumption of the neutral bending axis lying on the surface of the shell, the predictions of Equation (5.110) are compared with the results of the realistic, elastic-viscoplastic two-dimensional finite element models discussed earlier. Figures 5.27 and 5.28 show the strain decomposition of the simulation results of the Mold A geometry presented in Chapter 2, through the thickness at different points along the wide face centerline and in the center of the inner curve region. The total strain from the inner flat region is subtracted from the total strain in the inner curve region to isolate the "bending strain." Figure 5.28 clearly shows that this bending strain increases linearly with distance below the shell surface. This bending strain at the surface is slightly compressive, but close to the value of zero that corresponds to the neutral bending axis lying on the surface as assumed in the analytical model above. Figure 5.29 shows that the analytical model matches the bending strains on the solidification front, defined as 75% solid, in the inside curve region for the A-type mold with two different funnel widths. The fact that the ferrostatic pressure keeps the shell in relatively good contact with the mold is one reason that the simple analytical model matches so well with the numerical predictions. The mold forces the inelastic strain to develop in the shell to cause the total strain predicted by the bending model. This model clearly is a powerful tool for characterizing the bending imparted in the shell by different funnel geometries.

It is particularly useful because hot tear cracks depend more on strain than on stress, and is discussed in more detail in the next section.

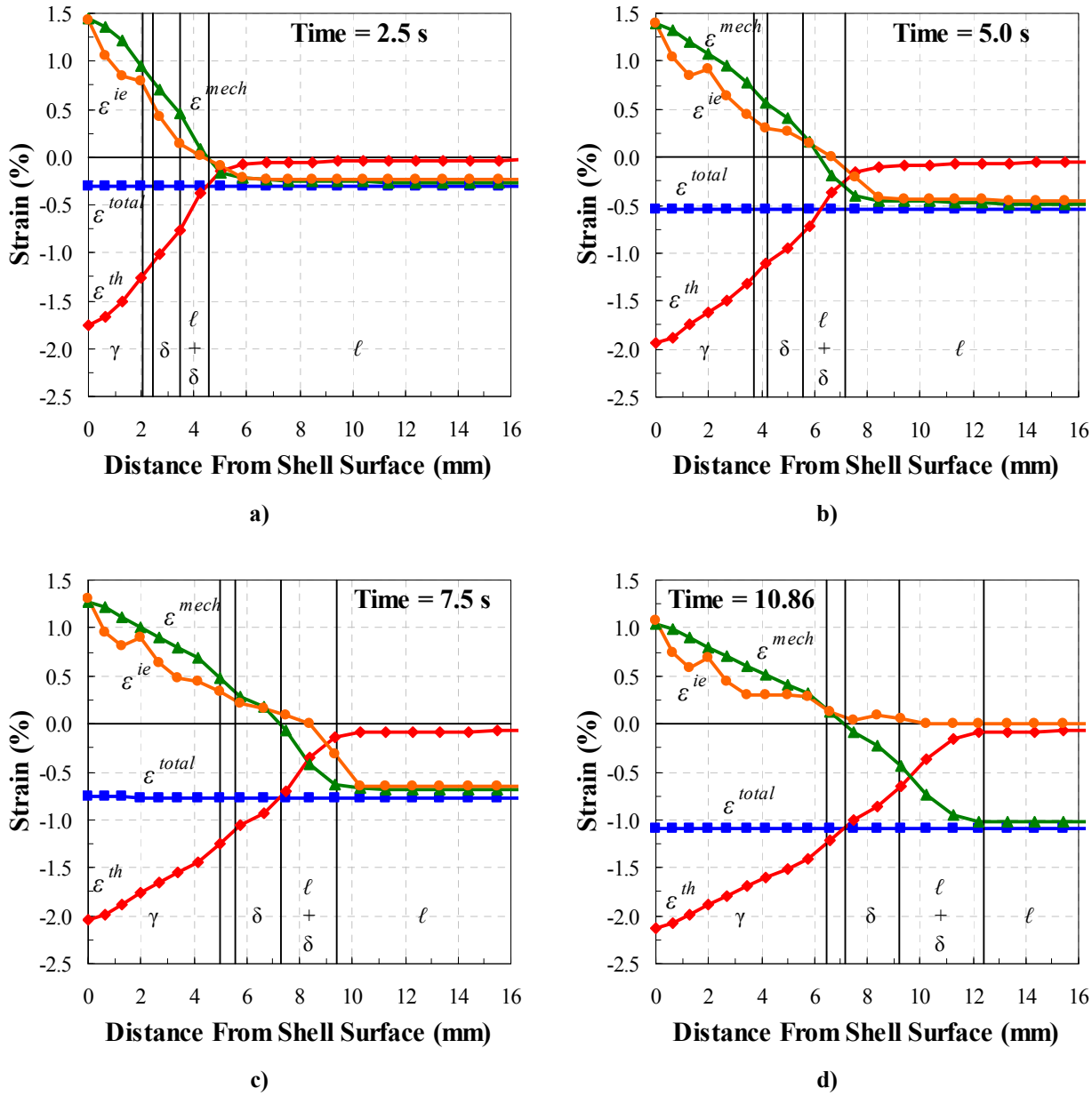

Figure 5.27. Strain Decomposition in Center of Inner Flat Region

5.8. Longitudinal Facial Cracking Potential

Longitudinal facial cracking (LFC) is an important consideration in designing the shape of funnel molds for continuous casting thin slabs. The solidifying steel is well-known to have very low ductility, and so is subject to hot-tear crack formation when subjected to small strains.

Navigating through a funnel mold naturally subjects the shell to transverse tensile strains, causing LFCs if they are too high. Longitudinal cracks have been observed to form at various locations around the perimeter of the shell in both conventional and funnel continuous casting molds, as summarized in Figure 5.30.

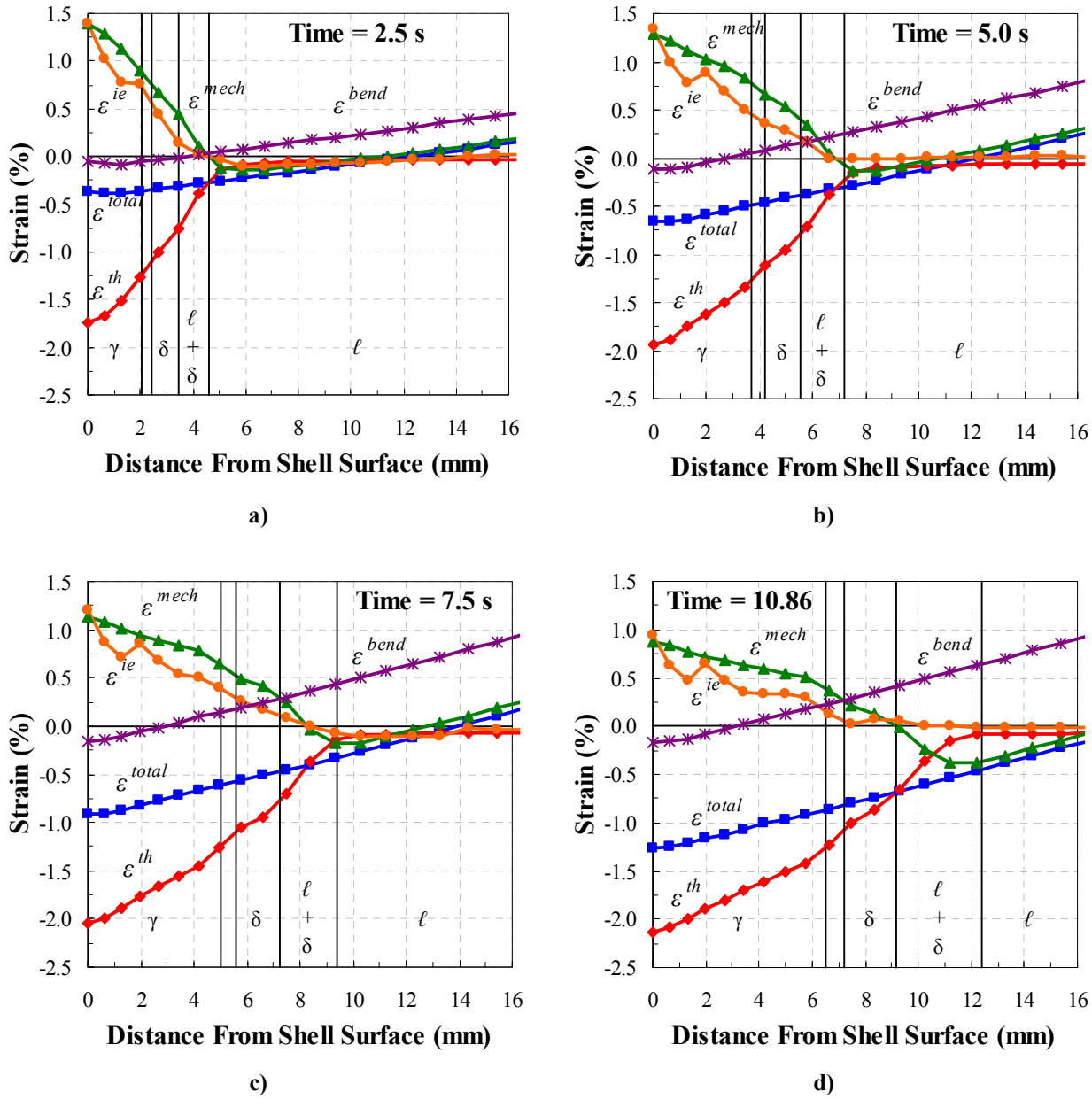

Figure 5.28. Strain Decomposition in Center of Inner Curve Region

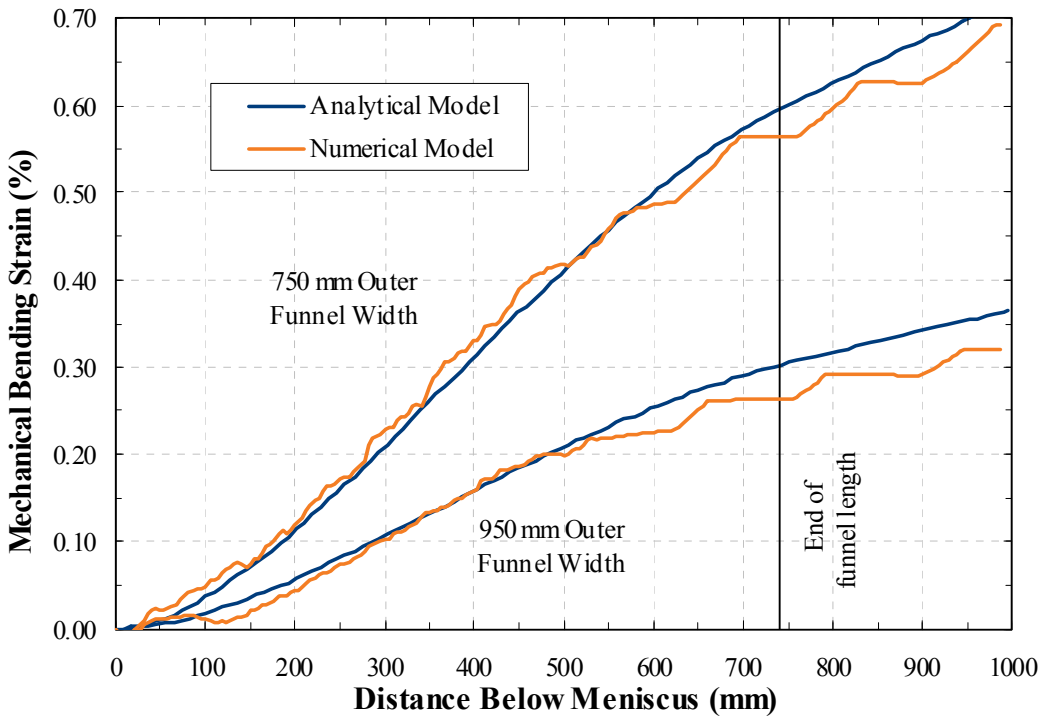

Figure 5.29. Comparison of Bending Strains on the Solidification Front

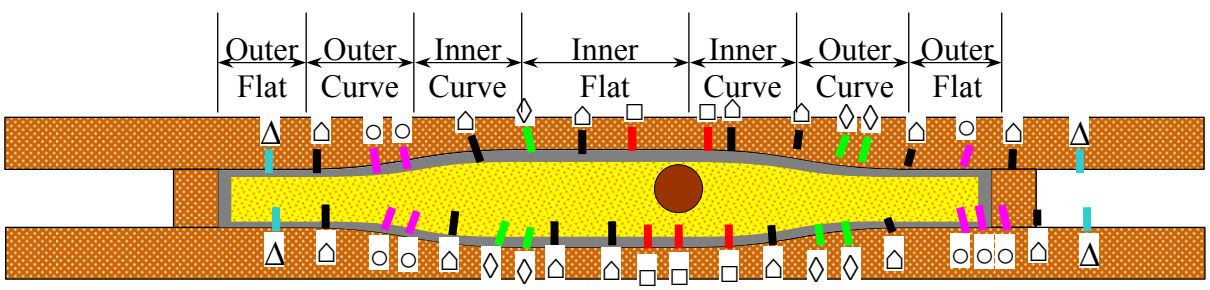

Mode	Symbol	Location	Notes
I	◊	Inside Curve	Funnel only; depression-type; excessive bending
II	○	Outside Curve	Funnel only; depression-type; excessive NF taper
III	⌂	No Preference	Jagged, short cracks; heat transfer related
IV	□	Near SEN	Fluid-flow related
V	Δ	Off-Corner WF	Inadequate NF taper

Figure 5.30. Longitudinal Facial Crack Locations and Mechanisms

Apart from the pioneering work by Brimacombe and colleagues [3,14], little work has been done to investigate longitudinal facial cracks. Cracks form from a combination of tensile strain and loss of metallurgical ductility. Tensile strains may arise from mechanical effects (such as bending and bulging, which are the main cause of transverse cracks), or from combined

thermo-mechanical effects (which are the main cause of longitudinal cracks, such as hot tears). Hot tears occur from excessive tensile strain across the roots of the dendrites at the solidification front; microsegregation effects depress the local solidus temperature, resulting in thin liquid films between dendrites that act as strain concentrators. Hot tear cracks can propagate through the shell immediately, or remain a subsurface crack that grows with the solidification front and reduces the load-carrying capability of the shell until rupture. The weakened shell may rupture at or below mold exit due to overload from the ferrostatic pressure. The effective shell thickness is measured from the strand surface to the root of the crack, and previous calculations [23] have shown that the critical shell thickness at mold exit is just 3 mm. Breakouts occur where cracks penetrate through to the surface because the local shell thickness falls below this limit. Local shell thickness can be reduced from gap formation, either by mechanical forces lifting the shell from the mold surface or from fluid-flow related effects such as variations in slag layer thickness (either too thick or too thin).

The different types of longitudinal cracking in the mold observed in plants share some common causes, but also exhibit unique mechanisms, which depend on where the cracks occur

I. In the inner-curve region, the funnel mold imparts a mechanical bending effect in the solidifying shell, which causes extra tensile strains on the solidification front and extra compressive strains on the shell surface. The extra strain on the solidification front makes subsurface hot tears more likely to form in this region. These cracks are often found in the root of a depression, such as shown in Figure 5.31, which suggests a contribution from another mechanism as well, such as buckling or necking of the shell. These cracks are initiated by problems at the meniscus. Funnel design impacts this mechanism because the additional mechanical bending strains in the shell depend on the funnel shape.
II. In the outer-curve region, the bending effect of the funnel has the reverse effect, reducing the natural tensile strains on the solidification front. However, longitudinal cracks both with and without depressions have been frequently observed in this region. Excessive narrow face taper, combined with frictional effects in the inside flat and inside curve regions, may push on the shell, causing it to lift off of the mold face, leading to a gap, as well as buckling. Funnel design impacts this mechanism because the changing shape of the funnel with distance down the mold may push the shell outward, causing a detrimental gap

to form, if the funnel perimeter decreases faster than shell shrinkage from cooling, inelastic strain, and narrow-face taper can accommodate.

III. Non-uniform heat transfer around the strand perimeter can lead to cracks along grain boundaries as a result of locally reduced heat transfer causing larger, more brittle grains. All continuous casting mold shapes are subject to this type of cracking, which can be initiated by mold level fluctuations, variations in slag rim thickness, fingers of mold flux caught in the shell-mold gap, and other problems at the meniscus which produce local nonuniformities that enhance local strain concentration. Funnel design impacts this mechanism through its important effect on the flow pattern in the mold, especially in the funnel transition region (curved regions), which is susceptible to the largest level fluctuations.

IV. Fluid flow around the SEN is particularly important in funnel molds because of the relatively short distances between the nozzle and mold surface. Flow patterns in the mold can disrupt the infiltration of liquid flux feeding at the meniscus, cause shell thickness variations, excessive slag layer solidification, local increase of inclusions, and mold level fluctuations, especially near the SEN. Each of these can cause LFCs similar to Types I and III. Funnel design impacts this mechanism by affecting the space between the SEN and the mold.

V. Longitudinal cracks can form on the wide face of the shell, just off of the corner with the narrow face. These cracks are caused by two-dimensional effects, related to narrowface taper and mechanical shearing. With insufficient NF taper, ferrostatic pressure maintains shell contact with the central narrow face, causing the shell to rotate around the rigid corner, creating off-corner gaps, and related heat transfer drop and longitudinal depressions and cracks. With excessive NF taper, the shell can buckle near the corner. In addition, the accompanying excessive-cooling of the corner together with later reheating and subsurface cooling and shrinkage can lead to subsurface tensile strain and internal hot tears near the corner. All of these effects lead to off-corner longitudinal cracks. Funnel design impacts this mechanism in the same way as Type II cracks.

The cracking issues faced by a particular funnel design may be one or more of the above list, so funnel design and operation must simultaneously account for all of the mechanisms. Indeed, the

plant experience at Corus IJmuiden in Figure 5.32 suggests that all five types of longitudinal crack are likely present with A-type funnel design, though Type I clearly dominates the problem.

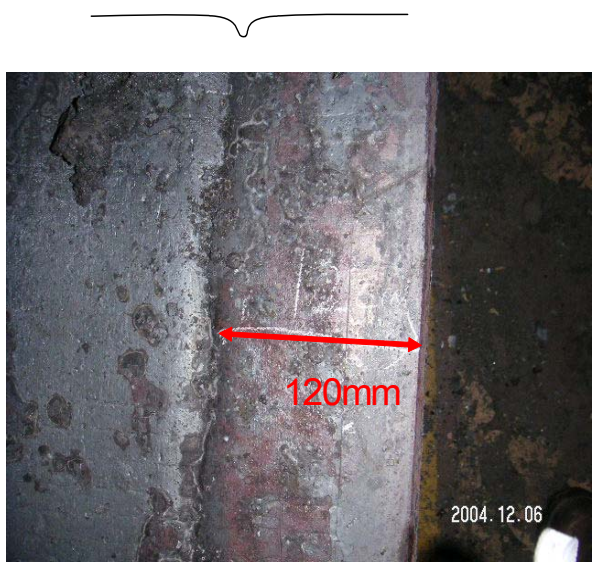

Figure 5.31. Depression-Type LFC [13]

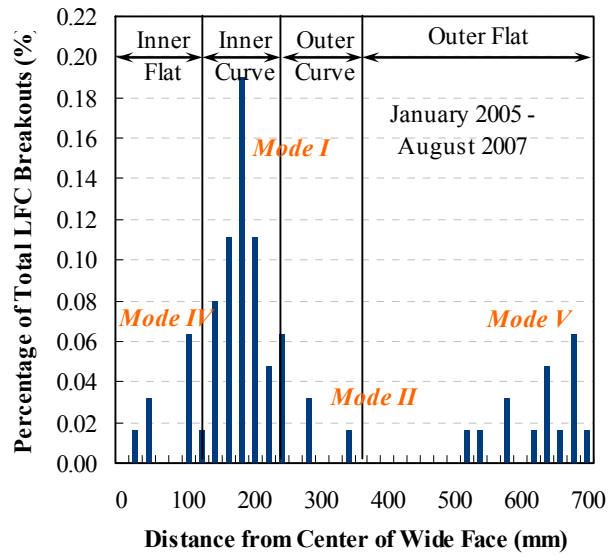

Figure 5.32. LFCs Occurring at Corus Ijmuiden [13]

Design of the funnel shape to avoid longitudinal cracking requires careful optimization to avoid both excessive bending effects and problems with fluid flow, so SEN design provides many parameters to adjust in the design process. Other design variables, including narrow face taper, flow-pattern control (nozzle shape, etc), and sub-mold support (e.g. foot roll alignment) are all equally or more important than funnel design in controlling longitudinal cracks. Funnel designs should be evaluated together with all variables which define the entire mold system, according to what produces the lowest cracking tendency in the solidifying steel and the highest product quality. Thus, the best funnel design depends on the dominant crack mechanism and can vary between different casting operations.

Hot tears are casting defects that occur when the liquid is unable to flow into the roots of the dendrites while the mushy zone is under tension, as shown in Figure 5.33, and are typically found at grain boundaries [6]. Won *et al.* [39] proposed the following empirical criterion to predict the onset of hot tearing:

$$\varepsilon_{crit} = \frac{0.02821}{\dot{\varepsilon}^{0.3131} \cdot \Delta T_B^{0.8638}} \tag{5.112}$$

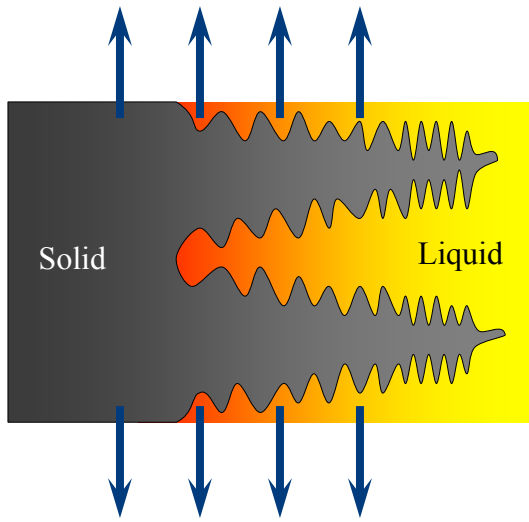

Figure 5.33. Hot Tearing is Caused by Tensile Stress on the Mushy Zone

where ε_{crit} is the critical strain (here in m/m, not percent), $\dot{\varepsilon}$ is the average inelastic strain rate over the brittle temperature zone (here in m/m/s), and ΔT_B is the width of the brittle temperature zone (here in ºC). The brittle temperature zone is defined in [39] as the range of the mushy zone between 90% and 99% solid:

$$\Delta T_B = T\left(f_s = 0.99\right) - T\left(f_s = 0.90\right) \tag{5.113}$$

The average inelastic strain rate was calculated in this work using a simple finite difference approximation:

$$\dot{\varepsilon}_{ij} = \frac{\varepsilon_{ij}^{ie}\left(f_s = 0.99\right) - \varepsilon_{ij}^{ie}\left(f_s = 0.99\right)}{t\left(f_s = 0.99\right) - t\left(f_s = 0.99\right)} \tag{5.114}$$

where the involved inelastic strains and times are found by interpolating through the results first for temperatures at the respective fraction solids, which are then used to interpolate for the other data. Furthermore, the maximum principal component of the inelastic strain rate is used in the critical strain calculation; this was always the circumferential component in the two-dimensional simulations.

To actually evaluate the potential for hot tearing, the critical strain is compared against the "damage strain," which is the inelastic strain accumulated over the brittle temperature zone. For monotonic thermal histories, the damage strain is simply:

$$\varepsilon_{dmg} = \varepsilon^{ie}\left(f_s = 0.99\right) - \varepsilon^{ie}\left(f_s = 0.90\right) \tag{5.115}$$

In the case of more complicated thermal histories, this needs to be generalized to include every pass in and out of the brittle temperature zone, which did not occur in the funnel simulations, but has been observed in other thermomechanical models of the solidifying shell [10]. The comparison of the damage strain to the critical strain is facilitated with the definition of a "damage index." The damage index D is a simple ratio which expresses the relative danger of crack formation:

$$D = \frac{\varepsilon_{dmg}}{\varepsilon_{crit}} \tag{5.116}$$

Crack formation is imminent when the damage index exceeds unity. This single value simplifies comparing different funnel geometries for their tendency to induce cracking, as discussed next.

Initial post-processing of the thermomechanical simulations discussed above for hot-tearing potential showed that the calculation is extremely sensitive to mesh spacing and time step size. Instead of trying to perform this calculation in two dimensions, a one-dimensional simulation was performed with boundary conditions specified according to the analytical bending model to include the bending effect. With mesh sizes as small as 0.03 mm, the predictions of the average strain rate were still extraordinarily noisy, and so the carbon content was increased to 1% wt. C, with all other alloying components identical to the other cases. This significantly reduced the noise in the damage calculation, but the high-carbon steel is much more crack sensitive than the grade initially considered. Thus, the estimates given below should predict more cracks than observed, but nevertheless the effect of geometry can still be investigated effectively.

The geometries considered for this small study include a parallel mold, (also representing regions away from funnels and corners); the nominal A-type mold presented in Chapter 2; the A-type mold with a 200 mm wider outer funnel width, and the A-type mold with a 100 mm longer funnel. Figure 5.34 shows that the damage strain in the inside curve region is decreased by using a wider funnel, or in particular, a larger horizontal funnel radius. Increasing the funnel length increases the damage strain deeper in the shell. Similar results are observed in the average inelastic strain rate over the brittle temperature zone, as shown in Figure 5.35. Evaluation of the Won critical strain rate with these values shows in Figure 5.36 that the funnel decreases the critical strain in the subsurface regions, and the same trends as above are observed. The critical strain is decreased by a lesser amount with the wider funnel (larger horizontal radius), and the

longer funnel results in lower critical strain deeper in the shell. Combining these results together via the damage index, Figure 5.37 shows that although the damage index is always far below the "danger zone" of unity, the effect of the funnel geometry is to make hot tearing much more likely in the inner curve region. If some additional detrimental effect, such as a level fluctuation, superimposed additional strains that would tend to cause crack formation, then the results here suggest that funnel molds increase the likelihood of the crack actually opening and a breakout forming. This can be mitigated by using funnels with larger horizontal radii and shorter funnel lengths.

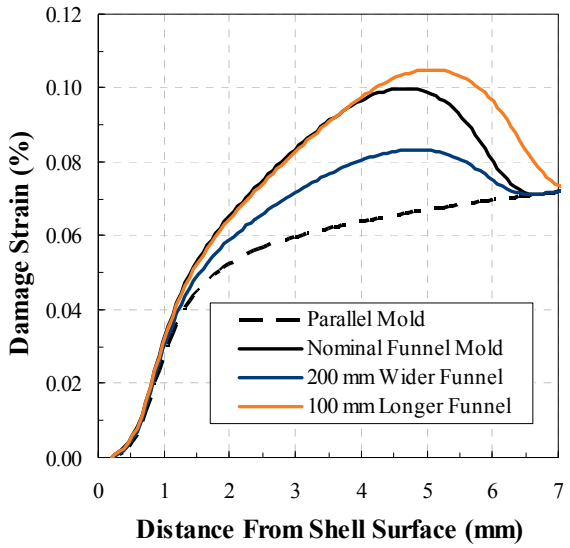

Figure 5.34. Accumulated Damage Strain

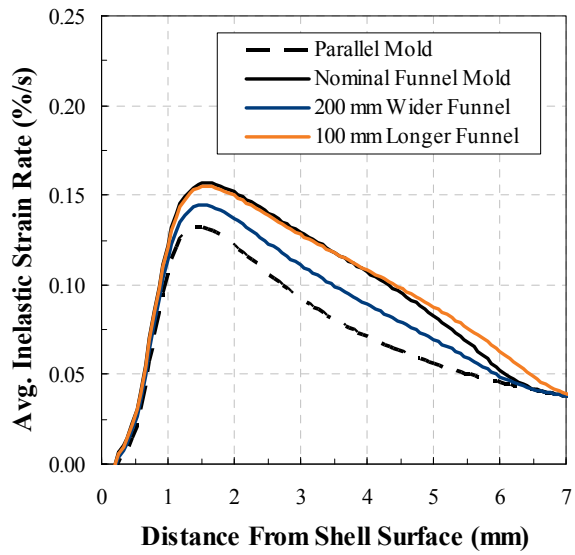

Figure 5.35. Average Inelastic Strain Rate in BTZ

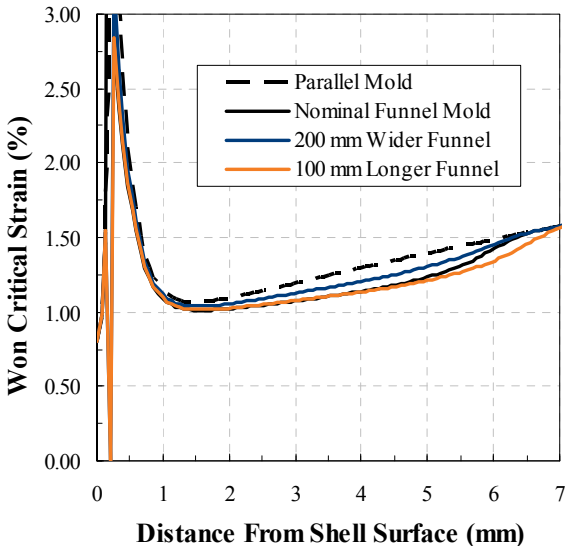

Figure 5.36. Won Critical Strain

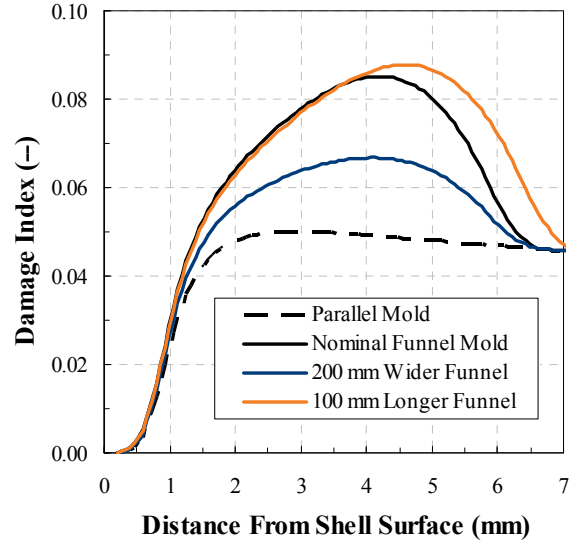

Figure 5.37. Damage Index

5.9. Conclusions

Mathematical models have been employed to study the effect of funnel geometry on the mechanical behavior of the solidifying shell in continuous casting funnel molds. After verifying a two-dimensional finite-element model with an analytical solution of solidification stresses, the model was used to simulate the mechanical behavior of the solidifying shell using the temperature fields calculated in Chapter 4. The funnel geometry is responsible for inducing bending behavior in the funnel transition region, which, when combined with the normal solidification behavior, tends to cause hot tearing in the inside curve region. A parametric study of the funnel geometry revealed that this bending effect is reduced as the funnel gets shallower and wider, and a simple analytical model identified that the severity of the bending can be accurately characterized by the horizontal radius of the funnel. During normal operation, the funnel will not cause hot tear cracks to form, but as a result of the bending effect, the funnel is less likely to survive an event that would cause the hot tear to open.

5.10. References

1. *ABAQUS 6.8-1 User Manuals*. (2008), Dassault Simulia, Inc., 166 Valley Street, Providence, RI, USA 02909-2499.
2. R.J. Asaro and V.A. Lubarda, *Mechanics of Solids and Materials*, 1e. Cambridge University Press, (2006).
3. J.K. Brimacombe, F. Weinberg, and E.B. Hawbolt, "Formation of Longitudinal, Midface Cracks in Continuously-Cast Slabs." *Metallurgical and Materials Transactions*, **10B**:2 (1979), pg. 279-292.
4. W. Chen, Y.Z. Zhang, C.J. Zhang, L.G. Zhu, B.X. Wang, W.G. Lu, and J.H. Ma, "Numerical Simulation of the Thermo-Mechanical Process for Beam Blank Continuous Casting." *Acta Metallurgica Sinica (English Letters)*, **20**:4 (2007), pg. 241-250.
5. R.D. Cook, D.S. Malkus, M.E. Plesha, and R.J. Witt, *Concepts and Applications of Finite Element Analysis*, 4e. John Wiley and Sons, (2002).
6. J.A. Dantzig and M. Rappaz, *Solidification*. EPFL Press, (2009).
7. A. Grill, J.K. Brimbacombe, and F. Weinberg, "Mathematical Analysis of Stresses in Continuous Casting of Steel." *Ironmaking and Steelmaking*, **3**:1 (1976), pg. 38-47.
8. K. Harste, "Untersuchungen zur Schrumpfung und zur Entstehung von Mechanischen Spannungen Während der Erstarrung und Nachfolgender Abkühlung Zylindrischer Blöcke aus Fe-C-Legierungen." Ph.D. Dissertation, Technischen Universität Clausthal, (1989).

9. Y. Hebi, Y. Man, Z. Huiying, and F. Dacheng, "3D Stress Model with Friction in and of Mould for Round Billet Continuous Casting." *ISIJ International*, **46**:4 (2006), pg. 546-552.

10. L.C. Hibbeler, K. Xu, B.G. Thomas, S. Koric, and C. Spangler, "Thermomechanical Modeling of Beam Blank Casting." *Iron and Steel Technology*, **6**:7 (2009), pg. 60-73.

11. R.C. Hibbeler, *Mechanics of Materials*, 5e. Prentice Hall, (2003).

12. I. Jimbo and A.W. Cramb, "The Density of Liquid Iron-Carbon Alloys." *Metallurgical and Materials Transactions*, **24B**:1 (1993), pg. 5-10.

13. A.A. Kamperman, Private Communications, 2007.

14. J. Konishi, M. Militzer, J.K. Brimacombe, and I.V. Samarasekera, "Modeling the Formation of Longitudinal Facial Cracks During Continuous Casting of Hypoperitectic Steel." *Metallurgical and Materials Transactions*, **33B**:3 (2002), pg. 413-423.

15. E. Kröner, "Allgemeine Kontinuumstheorie der Versetzungen und Eigenspannungen." *Archive for Rational Mechanics and Analysis*, **4**:1 (1959), pg. 273-334.

16. S. Koric, "Efficient Thermo-Mechanical Model for Solidification Processes and its Applications in Steel Continuous Casting." Ph.D. Dissertation, The University of Illinois at Urbana-Champaign, (2006).

17. S. Koric and B.G. Thomas, "Efficient Thermo-Mechanical Model for Soldification Processes." *International Journal for Numerical Methods in Engineering*, **66**:12 (2006), pg. 1955-1989.

18. S. Koric, L.C. Hibbeler, and B.G. Thomas, "Explicit Coupled Thermo-Mechanical Finite Element Model of Steel Solidification." *International Journal for Numerical Methods in Engineering*, **78**:1 (2009), pg. 1-31.

19. P.F. Kozlowski, B.G. Thomas, J. Azzi, and H. Wang, "Simple Constitutive Equations for Steel at High Temperature." *Metallurgical and Materials Transactions*, **23A**:3 (1992), pg. 903-918.

20. E.H. Lee, "Elastic-Plastic Deformation at Finite Strain." *Journal of Applied Mechanics*, **36**:1 (1969), pg. 1-6.

21. J.-E. Lee, H.N. Han, K.H. Oh, and J.-K. Yoon, "A Fully Coupled Analysis of Fluid Flow, Heat Transfer, and Stress in Continuous Round Billet Casting." *ISIJ International*, **39**:5 (1999), pg. 435-444.

22. J.-E. Lee, T.-J. Yeo, K.H. Oh, J.-K. Yoon, and U.-S. Yoon, "Prediction of Cracks in Continuously Cast Steel Beam Blank through Fully Coupled Analysis of Fluid Flow, Heat Transfer, and Deformation Behavior of a Solidifying Shell." *Metallurgical and Materials Transactions*, **31A**:1 (2000), pg. 225-237.

23. C. Li and B.G. Thomas, "Maximum Casting Speed for Continuous Cast Steel Billets Based on Sub-Mold Bulging Computation." *ISS Steelmaking Conference Proceedings*, The Iron and Steel Society, **85** (2002), pg. 109-130.

24. C. Li and B.G. Thomas, "Thermo-Mechanical Finite-Element Model of Shell Behavior in Continuous Casting of Steel." *Metallurgical and Materials Transactions*, **35B**:6 (2004), pg. 1151-1172.

25. J. Lubliner, *Plasticity Theory*, 1e. Dover, (2008).

26. A.M. Lush, G. Weber, and L. Anand, "An implicit time-integration prodecure for a set of internal variable constitutive equations for isotropic elasto-viscoplasticity." *International Journal of Plasticity*, **5**:5 (1989), pg. 521-549.

27. Y. Meng, B.G. Thomas, A.A. Polycarpou, A. Prasad, and H. Henein, "Mold Slag Property Measurements to Characterize Continuous-Casting Mold—Shell Gap Phenomena." *Canadian Metallurgical Quarterly*, **45**:1 (2006), pg. 79-94.

28. H. Mizukami, K. Murakami, and Y. Miyashita, "Elastic Modulus of Steels at High Temperature." *Tetsu-to-Hagane*, **63** (1977), pg. S652.

29. A. Moitra, B.G. Thomas, and W. Storkman, "Thermo-Mechanical Model of Steel Shell Behavior in the Continuous Casting Mold." In *Proceedings of the 1992 TMS Annual Meeting*, EPD Congress, pg. 547-557.

30. J.K. Park, B.G. Thomas, and I.V. Samarasekera, "Analysis of Thermomechanical Behaviour in Billet Casting with Different Mould Corner Radii." *Ironmaking and Steelmaking*, **29**:5 (2002), pg. 1-17.

31. J.K. Park, "Thermo-Mechanical Phenomena in High Speed Continuous Casting Processes." Ph.D. Dissertation, The University of British Columbia, (2002).

32. J.M. Risso, A.E. Huespe, and A. Cardona, "Thermal Stress Evaluation in the Steel Continuous Casting Process." *International Journal for Numerical Methods in Engineering*, **65** (2006), pg. 1355-1377.

33. K. Schwerdtfeger, M. Sato, and K.-H. Tacke, "Stress Formation in Solidifying Bodies: Solidification in a Round Continuous Casting Mold." *Metallurgical and Materials Transactions*, **29B**:5 (1998), pg. 1057-1068.

34. B.G. Thomas, J.K. Brimacombe, and I.V. Samarasekera, "The Formation of Panel Cracks in Steel Ingots, A State of the Art Review, Part I: Hot Ductility of Steel." *Transactions of the Iron and Steel Society*, **7** (1986), pg. 7-20.

35. B.G. Thomas, A. Moitra, and R. McDavid, "Simulation of Longitudinal Off-Corner Depressions in Continuously Cast Steel Slabs." *Iron and Steelmaker*, **23**:4 (1996), pg. 57-70.

36. E.-G. Wang, J.-C. He, "Finite Element Numerical Simulation on Thermo-Mechanical Behavior of Steel Billet in Continuous Casting Mold." *Science and Technology of Advanced Materials*, **2** (2001), pg. 257-263.

37. J.H. Weiner and B.A. Boley, "Elasto-Plastic Thermal Stresses in a Solidifying Body." *Journal of the Mechanics and Physics of Solids*, **11**:3 (1963), pg. 145-154.

38. J.R. Williams, R.W. Lewis, and K. Morgan, "An Elasto-Viscoplastic Thermal Stress Model with Applications to the Continuous Casting of Metals." *International Journal for Numerical Methods in Engineering*, **14** (1979), pg. 1-9.

39. Y.-M. Won, T.-J. Yeo, D. J. Seol, and K. H. Oh, "A New Criterion for Internal Crack Formation in Continuously Cast Steels." *Metallurgical and Materials Transactions*, **31B**:4 (2000), pg. 779-794.

40. H. Zhu, “Coupled Thermal-Mechanical Finite-Element Model with Application to Initial Solidification.” Ph.D. Thesis, The University of Illinois at Urbana-Champaign, (1993).

41. L.-G. Zhu and R.V. Kumar, “Modelling of Steel Shrinkage and Optimisation of Mould Taper for High Speed Continuous Casting.” *Ironmaking and Steelmaking*, **34**:1 (2007), pg. 76-82.

42. O.C. Zienkiewicz, R.L. Taylor, and J.Z. Zhu, *The Finite Element Method: Its Basis and Fundamentals*, 6e. Elsevier, (2005).

CHAPTER 6

CONCLUSIONS AND FUTURE WORK

6.1. Conclusions

A two-dimensional thermomechanical numerical model of the solidifying shell and a three-dimensional model of the mold in continuous casting of steel in funnel molds has been developed to study the effect of funnel geometry on the behavior of the shell. Specific conclusions arising from the mold thermal model, shell solidification heat transfer model, and shell mechanical model are given in the Conclusions to Chapters 3,4, and 5 respectively.

The thermal aspects of the model were calibrated with a large database of plant measurements from the Corus Direct Sheet Plant in IJmuiden, The Netherlands, most importantly resulting in an interfacial heat flux profile between the mold and shell. The calibration exercise also showed the variation of mold and shell thermal behavior with decreasing mold thickness, *i.e.*, mold wear. The geometric effect of the funnel on the thermal behavior of the mold was found to be very small, and increases with decreasing horizontal funnel radius. Variations in mold surface temperature caused by geometric features such as water slot spacing around bolts and gap conduction variations are likely to be more important for detrimental shell behavior, *i.e.*, cracks, than the geometric effect of the funnel itself.

Although the constitutive response of the solidifying steel is dependent upon temperature, the previously-mentioned thermal effect is indeed small on the resulting mechanical response of the shell. The major effect of the funnel geometry on the mechanical response of the shell is to induce bending, *i.e.*, tension on the surface and compression on the solidification front or vice-versa, which is proportional to the horizontal funnel radius. In fact, the bending strain can be accurately quantified using a simple relationship derived using elementary solid mechanics. This bending effect was found to make hot-tear cracks that originate beneath the surface more likely in the “inside curve” region of the funnel, and less likely in the “outside curve” region of the funnel. This finding corresponds well with one family of longitudinal face cracks that have been observed in practice. The parametric studies performed in this work have also identified that the change in shell perimeter length due to the funnel must be accounted for when designing narrow face taper practices.

Several findings in this work indicate that the optimum funnel shape is to maximize the funnel radius of curvature, which means at best using a parallel-walled mold with no funnel at all. Barring this, the optimum funnel shape has no "inner flat" region, an outer funnel width as wide as possible, and a crown as shallow as possible, as shown in Figure 6.1. The outer funnel width is specified by consumer demand for minimum product width, while the crown size must be balanced with the SEN size to avoid fluid-flow related defects. This opens a new field of research in the design of funnel molds and SENs.

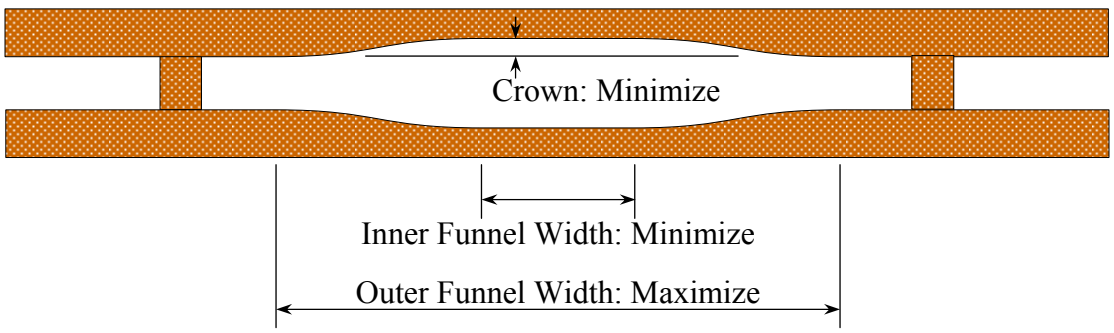

Figure 6.1. Recommended Funnel Geometry

6.2. Future Work

Several points of future work have been indicated throughout this work. The model developed here, as it stands, is already a very useful prediction tool, and should be used to investigate the behavior of the solidifying shell at various casting speeds, steel grades, funnel shapes, mold tapers, and other casting parameters such as interfacial friction coefficient and heat flux profile. One ultimate and practical goal is to recommend safe operating practices for higher casting speeds.

The numerical model developed here could be improved in several ways. One issue of cracking that is unique to funnel molds is the "bend" in the funnel at the end of the funnel length; this can induce transverse cracking and requires three-dimensional models to study properly. Other important multi-physics effects include the coupled effects of fluid flow in the liquid pool, and the thermal distortion of the mold on the shell heat transfer and deformation. Other future improvements include developing a cooling-rate-dependent phase fraction model, anisotropic material behavior, finite deformation, and better cracking criteria.